Politecnico di Torino

Corso di Laurea Magistrale in Ingegneria Meccanica

Tesi di Laurea

Real time active thermography for defect detection on arc welding: numerical and experimental analysis for model validation

Relatori:

Prof.ssa Raffaella Sesana

Ing. Luca Santoro

Ing. Rosario Molica Nardo

Ing. Dario Rini

Candidato:

Claudio Amodeo

Dipartimento di Ingegneria Meccanica e Aerospaziale

DIMEAS

Anno accademico 2021/2022

ABSTRACT

This work aims to investigate the use of active thermography on welded joints, a non-destructive method which is required if verifications are carried out on working components. Unlike the traditional method, where the workpiece is thermally stimulated by a laser beam at the end of the process, the method here adopted is based on real-time control of welding. By means of a thermal imaging camera, in fact, data collection takes place simultaneously with the welding itself, leading to a considerable reduction in time and consequently in costs. Thanks to Ades Group, at their site in Rovato (BS), four welding tests, monitored by an infrared camera, were carried out to analyze the different behavior of S275JR steel depending on welding method (SMAW and GMAW), material thickness (3mm and 5mm) and type of joint (butt joint and tee joint). All data were analyzed on the ResearchIR software, which enabled us to detect the presence of programmed defects from anomalies in temperature distribution along profiles or weld bead sections. Subsequently, metallographic examinations and hardness tests were carried out to characterize the microstructures and to distinguish the weld bead area, the heat affected zone (HAZ) and the base material. The various data obtained were used on MSC Marc Mentat to create a simulation of the welding process; as an output we can observe thermo-structural characteristics, the evolution of microstructures and deformations. Finally the simulation results will be compared with the experimental ones to verify the accuracy of the model.

SUMMARY

1 INTRODUCTION

This chapter will introduce the main technology on which this experimental thesis is based on: infrared thermography. We will discuss its evolution over time with a brief reference to the physical laws that describe this phenomenon.

The various methods of thermography most commonly used in industry will then be defined and some application examples will be mentioned. In addition, welding processes will be briefly discussed, with particular emphasis on SMAW and GMAW methods, and examples of infrared thermography as a non-destructive testing method for welding will be shown.

1.1 History of thermography

The discovery of thermography was made between 1770 and 1800 by the Italian researcher Marsilio Landriani. After some experiments with a glass prism through which the sun's rays split the light into colors, he discovered that beyond the 'red zone' there was an area outside the colors of the prism where a further increase in temperature was detected.

Figure 1.1 : Marsilio Landriani and Sir Frederik William Herschel

Later, Sir Frederik William Herschel, a German astronomer, had the same intuition while searching for an optical filter to reduce the brightness of the sun during telescope observations.

He was accidentally struck by the fact that some of the colored glass filters showed different amounts of heat from the sun, and some in particular risked injuring his eyes after only a few moments of observation.

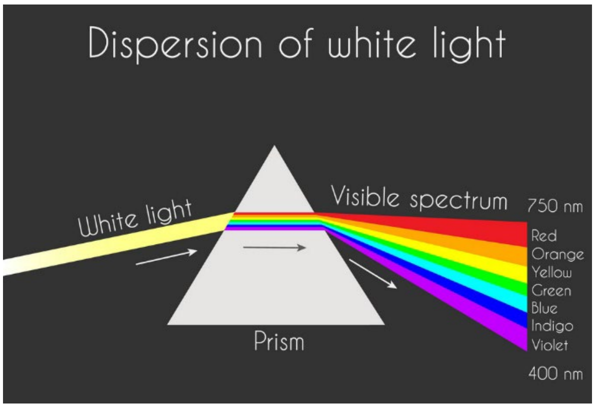

Figure 1.2 : Dispersion of white light through a prism

He wanted to investigate further and after several experiments, using a glass prism through which sunlight passed and some thermometers as detectors, he was the first to ascertain the existence of points outside the visible spectrum where heat radiation reached higher values.

He realized that measurements within the visible spectrum could not achieve these results. Therefore, he placed a mercury-sensitive thermometer from one color to another in the prism spectrum and measured the temperatures.

He noticed that these increased as the thermometer moved beyond the red light. He called this zone 'dark heat' and today this zone is associated with the 'infrared wavelength' [23].

Between 1900 and 1920, the production of the first radiometric devices starts. They were able to detect living beings, ships, aircraft and even icebergs. During the First World War, infrared technology was used to detect the enemy and guide missiles.

Today, as technology evolves, there are devices capable of detecting temperatures down to one hundredth of a degree. Working at different wavelengths, they can even detect harmful gases.

Nowadays these devices are widely used in civil and military applications, for security, research, medicine and science.

It was only in the 1960s that the first thermal imaging cameras for industrial use were created.

The first commercially available thermal imaging camera was manufactured by AGA, a Swedish company, with the Model 650, that was used as a measurement tool for predictive maintenance, but also to monitor the thermal insulation of homes.

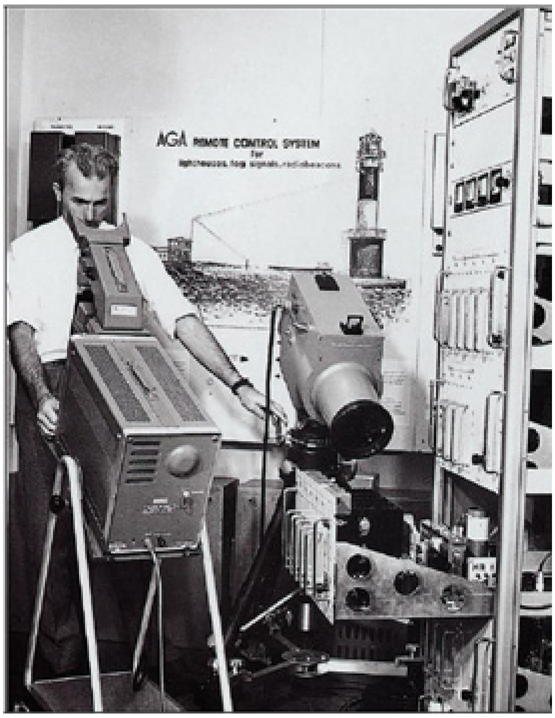

Figure 1.3 : AGA Model 650 thermal imaging camera

The instrumentation took up a lot of space compared to the latest thermal cameras and it allowed the acquisition of images in greyscale only.

It was only in 1966 that the possibility of acquiring colored images was introduced. The procedure, however, was very laborious and the resulting images had a bad resolution compared to greyscale images. This was only improved in the 1990s thanks to the better sensitivity of thermal imaging cameras. Since the 1970s, there has been also an improvement in the size of the entire measuring system, which, until then, had been a constraint on the handling of the system and its possible applications. In 1973, the first battery system was realized, which will however represent a restriction in terms of camera lifetime, a problematic aspect up until the late 2000's [24].

1.2 Physical laws

Infrared thermography uses the ability of a body to emit radiation in the infrared range when it is at a temperature above 0 K. It is necessary to start with the study of thermal waves in order to understand the basis of its operation. In particular they operate in the range between 0.75 - 1000 µm outside the visible spectrum. The highest temperatures are reached in this band [1].

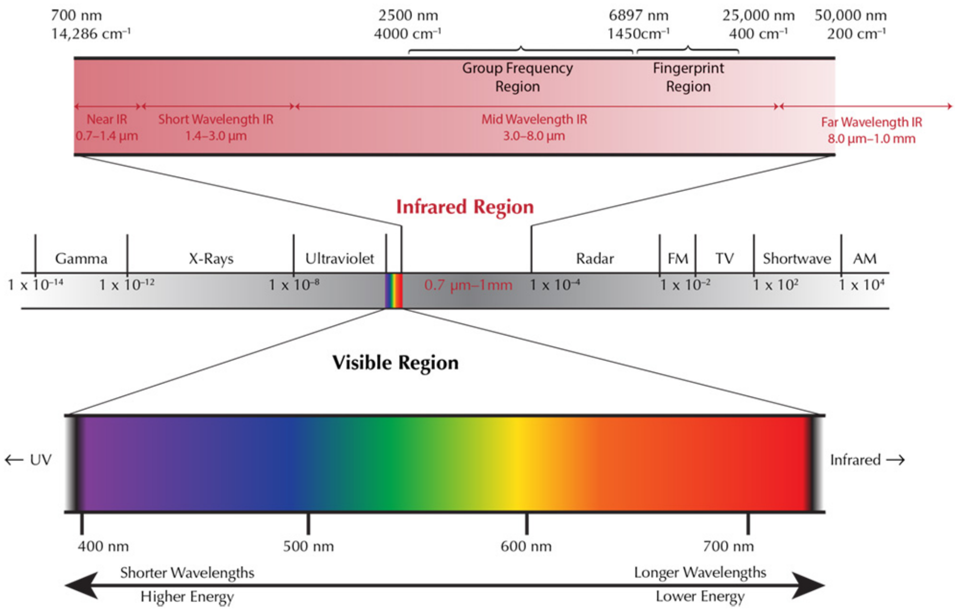

Figure 1.4 : Visible and Infrared Region Wavelengths

The ability of a body to emit radiation is called emissivity and it is measured by a thermal imaging camera. The focus of the problem is calculating the temperature from the measurement of emissivity.

The approach used to start defining the phenomenon is based on Kirchhoff's studies. To simplify the problem, he included in his analysis the concept of an ideal body, called the black body, which is not able to reflect or transmit but to absorb incident radiation. A peculiar characteristic of our interest is represented by the fact that the black body is a perfect emitter, it only emits the radiation it can absorb. The physical law at the basis of this phenomenon is Plank's Law, which describes the spectral distribution of the emitted radiation emitted by a black body.

$$B_\nu(T) = \frac{2\nu^2}{c^2} \frac{h\nu}{e^{h\nu/kT} - 1} \qquad (1)$$

Where:

- $B_\nu(T)$ is the spectral radiance (the power per unit solid angle and per unit of area normal to the propagation) density of frequency v radiation per unit frequency at thermal equilibrium at temperature T.
- h is the Planck constant
- c is the speed of light in a vacuum
- k is the Boltzmann constant
- v is the frequency of the electromagnetic radiation
- T is the absolute temperature of the body.

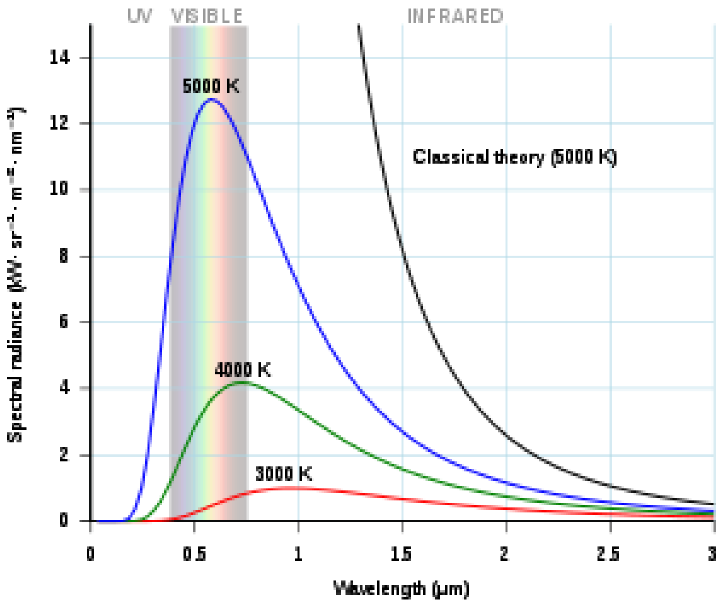

Figure 1.5 : Spectral radiance depending on temperature and wavelength

As it is possible to notice from the figure 1.5, the spectral emittance of a black body is zero for $\lambda = 0$ and for very high values of λ; it reaches its maximum in correspondence of a wavelength equal to λ_{max} whose value is inversely proportional to the value of the temperature. By derivation of Planck's law, with respect to λ, Wien identified a simple formula for the calculation of this wavelength expressed in μm.

$$\lambda = 2898/\mathrm{T} \qquad (2)$$

By integrating B_ν(T) over the frequency, the radiance L is:

$$L = \frac{2\pi^5}{15}\frac{k^4 T^4}{c^2 h^3}\frac{1}{\pi} = \sigma T^4 \frac{\cos(\theta)}{\pi} \qquad (3)$$

Where:

$$\sigma \equiv \frac{2\pi^5}{15}\frac{k^4}{c^2 h^3} = 5.670373 \times 10^{-8}\frac{W}{m^2 K^4} \qquad (4)$$

By subsequently integrating L over the solid angle Ω for all azimuthal angle (0 to 2π) and polar angle θ (0 to π/2), we arrive at the Stefan-Boltzmann law: the power j emitted per unit area of the surface of a black body is directly proportional to the fourth power of its absolute temperature:

$$j = \sigma T^4 \qquad (5)$$

A real body, however, is not treated as a black body but as a grey body. The difference lies in the non-frequency dependence and the no longer unitary emissivity, $\varepsilon < 1$. Some real cases may approach the special case of a blackbody in the case, for example, of surface coatings.

A real body, as mentioned above, is not able to absorb all the radiation incident on it because a fraction of it is reflected by its surface and a further fraction is transmitted through the body itself. The parameters representing the absorbed, reflected and transmitted fractions of the real body are dependent on the wavelength of the incident radiation.

This leads to the following equation:

$$\rho + \alpha + \tau = 1 \qquad (6)$$

Where:

- ρ is the reflectance
- α is the absorbance
- τ is the transmittance

The ability of a real body to emit absorbed electromagnetic radiation is limited by a fourth element, mentioned earlier, which is emissivity. For this reason we introduce the new parameter ε. It is defined as the ratio between the spectral power emitted by the real body and the spectral power emitted by a black body at the same temperature and wavelength. In the case of a black body, the spectral emissivity has a value equal to $\varepsilon = 1$; in the case of a grey body, its value is independent of the wavelength and $\varepsilon < 1$; finally, considering a highly polished material, $\varepsilon \cong 0$.

The introduction of parameter ε has made it possible to correct the physical laws on which the theory of thermography is based on and to adapt them to real bodies. The total power emitted by a grey body, for example, can be expressed using the modified Stefan-Boltzmann law as follows:

$$j = \varepsilon \, \sigma T^4 \qquad (7)$$

The main governing equation of the physics of the problem is the Fourier equation:

$$\frac{\delta T}{\delta t} = \alpha \frac{\delta^2 T}{\delta z^2} \qquad (8)$$

Where:

- T is the temperature in [K]
- α is the thermal diffusivity [m^2 /s] defined as:

$$\alpha = \frac{k}{\rho c} \qquad (9)$$

Where k is the thermal conductivity [W/(mK)], ρ the density [Kg/m^3] and c the specific heat [J/(KgK)].

Once the temperature distribution is known, the conduction heat flux at any point in the material or on its surface may be computed from Fourier's law.
The heat equation is derived from Fourier's law and conservation of energy. Fourier's law states that the time rate of heat transfer through a material is proportional to the negative gradient in the temperature and the area at right angles to that gradient, through which the heat flows.

$$q = -k \nabla T \qquad (10)$$

Where:
- q is the vector of local heat flux density [W/m^2]
- k is the thermal conductivity [W/(mK)]
- ∇T is the temperature gradient.

A change in internal energy per unit volume in the material, ΔQ, is proportional to the change in temperature, ΔT. That is:

$$\mathbf{\Delta Q = \rho . c_p . \Delta T} \qquad (11)$$

Using these two equations (10-11), we can derive the general heat conduction equation:

$$\frac{\partial}{\partial x}\left(k\frac{\partial T}{\partial x}\right)+\frac{\partial}{\partial y}\left(k\frac{\partial T}{\partial y}\right)+\frac{\partial}{\partial z}\left(k\frac{\partial T}{\partial z}\right)+q_V=\rho c_p\frac{\partial T}{\partial t} \qquad (12)$$

Where q_v is the rate at which energy is generated per unit volume of the medium [W/m^3].

This equation is also known as the Fourier-Biot equation and provides the basic tool for heat conduction analysis. From its solution, we can obtain the temperature field as a function of time.

2 STATE OF THE ART

This bibliographic research is based on two main topics: arc welding and active thermography. We will start researching a model capable of accurately simulating an arc welding process, after which it will be possible to carry out several tests on the weld bead using a thermal imaging camera.

2.1 Arc welding simulation

2.1.1 Heat transfer

To accurately describe the whole process in each aspect, the thermal analysis needs to involve the phase change phenomenon, including melting and solidification [2]. For this reason enthalpy methods are used, which are based on the heat conduction equations as following:

$$\frac{\partial}{\partial x}(k\frac{\partial T}{\partial x}) + \frac{\partial}{\partial y}(k\frac{\partial T}{\partial y}) + \frac{\partial}{\partial z}(k\frac{\partial T}{\partial z}) = \frac{\partial H}{\partial t} \qquad (13)$$

Where:

- T is the temperature
- k is the thermal conductivity
- H is the enthalpy

$$H = \int \rho C_p(T)dT \qquad (14)$$

Where ρ is the density of the material and $C_p(T)$ is the specific heat.

Convection and radiation heat transfer equations are used for boundary conditions on external surfaces.

Convective heat flux

$$q_c = h_c(T - T_0) \qquad (15)$$

Where h_c is the coefficient of convective heat transfer (usually from 5 to 20 W/m^2K)

Radiation flux

$$q_r = \varepsilon_r \sigma_r (T^4 - T_0^4) \qquad (16)$$

Where ε_r is the emissivity of the material surface and σ_r is the Stefan-Boltzmann constant. It is evident that the radiation flux component plays an important role especially in the proximity of the fused zone, due to the fourth degree power elevation.

2.1.2 Modeling

Once the parts to be welded have been chosen, the first step is to find a model characterizing the heat source. As shown in the work [3] the most appropriate model for this type of simulation is the "double ellipsoidal heat source model", also known as "Goldak model". Thanks to his mathematical formulation, based on the gaussian distribution of power density, it allows to effectively analyze the thermal distribution both along the arc motion and below the weld pool surface (deep penetration).

The equations that describe the power density distribution in a Cartesian coordinate system for the front quadrant is:

$$q_f(x,y,z,t) = \frac{6\sqrt{3}f_f Q}{abc_f\pi\sqrt{\pi}} exp\left\{-3\left(\frac{x^2}{a^2}+\frac{y^2}{b^2}+\frac{(z+vt)^2}{c_f^2}\right)\right\}$$

Similarly, for the rear quadrant:

$$q_r(x,y,z,t) = \frac{6\sqrt{3}f_r Q}{abc_r\pi\sqrt{\pi}} exp\left\{-3\left(\frac{x^2}{a^2}+\frac{y^2}{b^2}+\frac{(z+vt)^2}{c_r^2}\right)\right\} \qquad (17)$$

Where:

- η is the process performance (value from ISO standards, depends on the welding method)
- $Q = \eta VI$ is the welding heat source's input power
- v is the welding speed
- t is the current time
- f_r and f_f are constants that influence the intensity of the energy flow to the material ($f_r + f_f = 2$ and usually $f_f = 0.6$ $f_r = 1.4$)

As we can observe from the figure, the shape is made up of two ellipsoids placed in two perpendicular planes, where a, b, c_f and c_r are the characteristic dimensions.

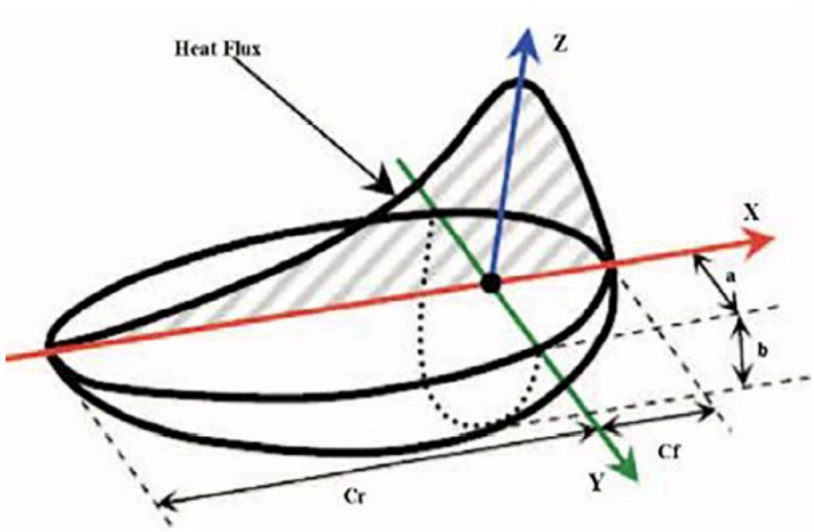

Figure 2.1 : Goldak model

This kind of solution is particularly suitable for simulated welding with coated electrodes [4]. In case of simulation of different processes such as GMAW, the method must be modified to obtain the correct shape of the weld pool. Therefore, instead of applying the fixed value of three, we need to separate the coefficient for each coordinate of the equation.

For the front part of the heat source model, the Equation is:

$$Q_f(x,y,z) = \frac{6\sqrt{3} f_f Q}{abC_f \pi \sqrt{\pi}} exp\left(\frac{-kx^2}{a^2}\right) exp\left(\frac{-ly^2}{b^2}\right) exp\left(\frac{-mz^2}{c^2}\right)$$

and for the rear part of the heat source model, the Equation is:

$$Q_r(x,y,z) = \frac{6\sqrt{3} f_r Q}{abC_r \pi \sqrt{\pi}} exp\left(\frac{-kx^2}{a^2}\right) exp\left(\frac{-ly^2}{b^2}\right) exp\left(\frac{-mz^2}{c^2}\right) \quad (18)$$

Where k, l, m are coefficients enabling modification of the liquid metal pool shape. In any case, for a proper calibration, it is necessary to compare the results with experimentally measured values.

Another possible solution, which is more suitable for laser welding or electron-beam welding is the Conical Model.

The three-dimensional Conical heat source distributes the heat flux in the volume sketched in the next figure. The diameter that defines the region in which the power density is distributed varies linearly along the thickness, with the maximum value at the top surface of the heat source and minimum at the bottom one. At any plane perpendicular to z-axis, the heat intensity is distributed in a Gaussian shape.

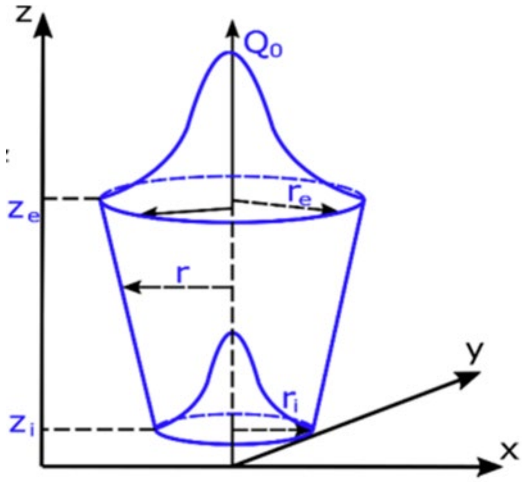

Figure 2.2 : Conical model

This model is governed by the following equation:

$$Q(x,y,z) = Q_0 exp\left(-\frac{x^2+y^2}{r_0^2(z)}\right)$$

$$r_0(z) = r_e + \frac{r_i - r_e}{z_i - z_e}(z - z_e) \qquad (19)$$

Where Q_0 is the maximum value of the heat flow volume density.

Usually, as a first evaluation to verify the accuracy of the model, a comparison between the calculated size of the molten zone and a real macrograph of the weld bead is made.

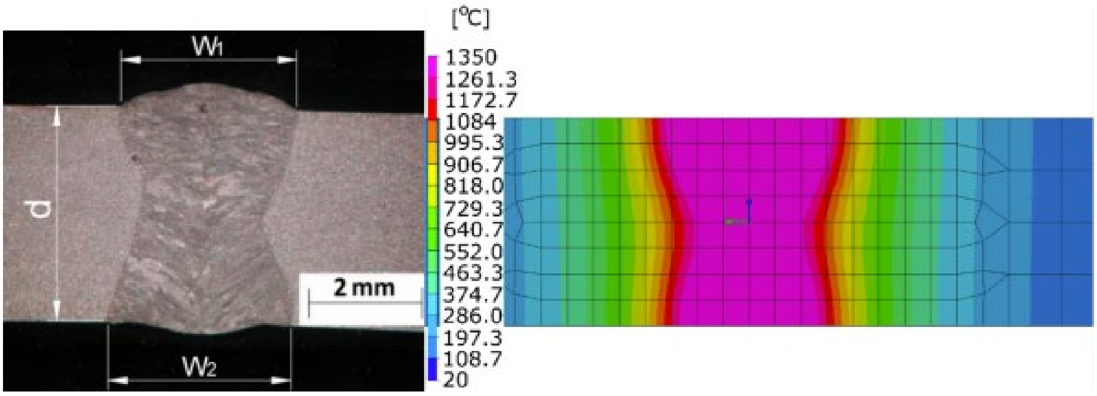

Figure 2.3 : Comparison between real macrograph and numerical simulation of the weld bead

2.1.3 Calculation techniques

This kind of analysis called "Transient Technique", requires a large amount of data, due to the calculations that are made for each subsequent time step, eventually adjusted depending on the mesh density and adaptivity. On the other hand, this method gives us a large amount of information including temperature fields, hardness, metallurgical phases, stresses and deformations. Therefore, according to our needs, we have to find a compromise between calculation time and amount of information.

The calculation of large structures with many welds, for example, are usually made using alternative techniques such as the "Macro-Bead" (MBD) , which is a sort of extension of the transient techniques that uses a prepared thermal cycle on one specific area of the model. The mesh, in this case, is only refined at the edges of the section of elements on which the thermal cycle is applied, making calculation faster. An alternative and even faster method is the "Shrinkage Technique", based on the distortion, where only the mechanical phenomena occurring during the process are used.

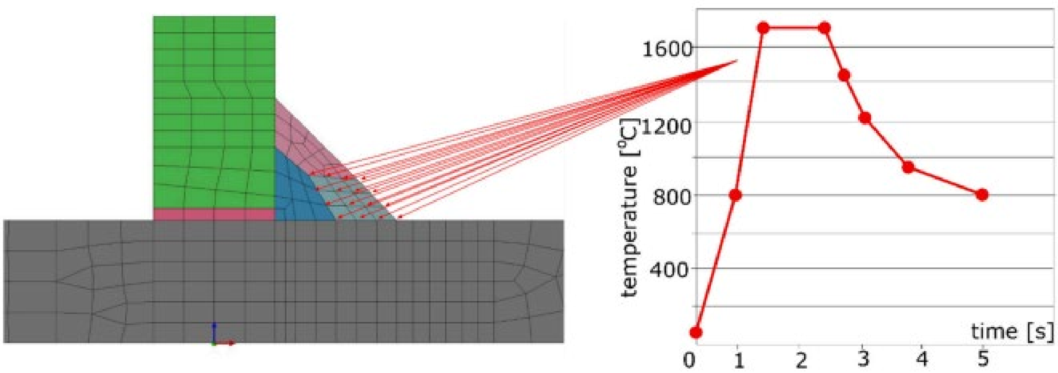

Figure 2.4 : MBD technique with its related thermal cycle

Comparing the same process results with different techniques [4] it is demonstrated that even if the distortion distribution slightly differed in the shapes, the peak values were similar.

As we said before, the results obtained with the transient technique are the most accurate and they can be taken as a reference for the other techniques. Two of the most important values distribution (normal displacement and equivalent Von Mises stresses) of the welding process are shown with their respective calculation times:

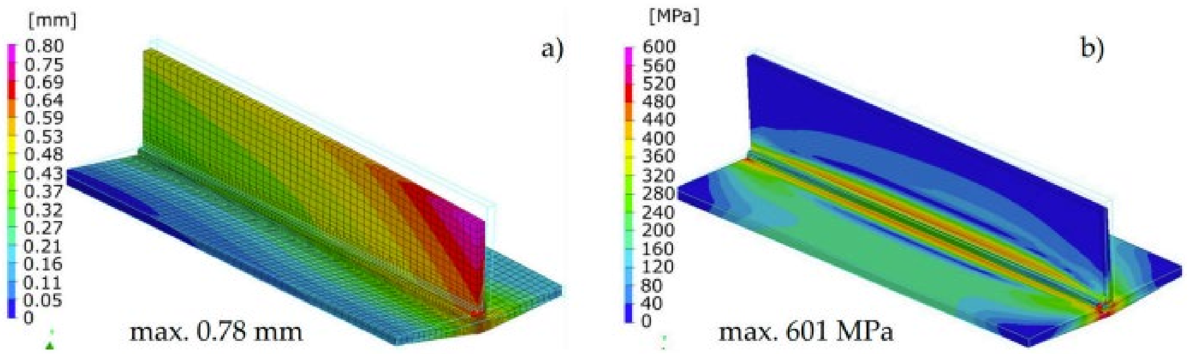

Transient	MBD (MBD DE) [1]	Shrinkage
2h 44 min 2 s	12 min 10 s (119 s)	55 s

Figure 2.5 : Simulation results with related calculation time

2.1.4 Parameters estimation

In welding simulation process, heat source parameters are often recommended by experience, but this choice can induce errors in the results. For this reason it is necessary to find out a method which allow to accurately estimate the source parameters [5]. In particular we will focus our attention on the relationships between these parameters and the welding pool characteristics: fusion width (W), penetration depth (D) and peak temperature (T_p). This analysis is a fundamental part of the simulation because it can avoid the necessity of large numbers of expensive and time-consuming experiments.

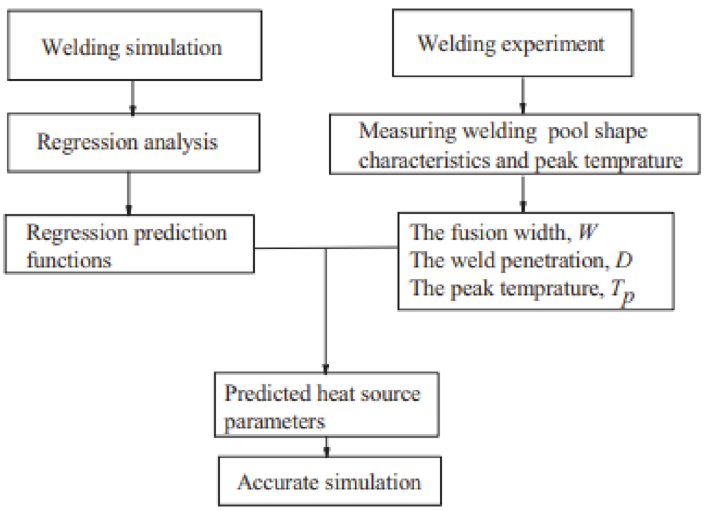

Figure 2.6 : Optimal procedure to predict heat source parameters

Two methods are now presented:

- Multiple regression analysis (MRA)
- Partial least-squares regression analysis (PLSRA)

In this case the regression analysis is made on a pipe model welded with GMAW method.

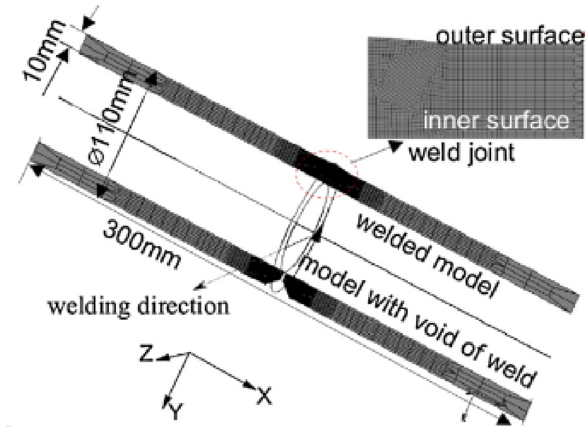

Figure 2.7 : GMAW pipe model

Multiple regression analysis

In this study two MRA were used:

- Nature logarithm regression model

$$f_{\log,i}\left(Q, a, b, c_f, c_r\right) = \alpha_i Q^{\beta 1_i} a^{\beta 2_i} b^{\beta 3_i} c_f^{\beta 4_i} c_r^{\beta 5_i} \quad (20)$$

- Linear regression model

$$f_{l,i}\left(Q, a, b, c_f, c_r\right) = \alpha_i + \beta 1_i Q + \beta 2_i a + \beta 3_i b + \beta 4_i c_f + \beta 5_i c_r \quad (21)$$

Where:

- $f_{\log,i}$ and $f_{l,i}$ are characteristic parameters of welding pool
- Q, a, b, c_f, c_r are heat source parameter of the simulation
- a_i, $\beta 1_i$, $\beta 2_i$, $\beta 3_i$, $\beta 4_i$, $\beta 5_i$ are coefficients

By performing multiple regression analysis comparing the experimental data with the simulation, the coefficients can be calculated.

Partial least-squares regression analysis

In this case four models were studied:

- Linear model

$$f_{l,i} = \alpha x + \varepsilon \quad (22)$$

- Quasi linear model

$$f_{\log,i} = \varepsilon' x^{\alpha} = \alpha x' + \varepsilon \quad (23)$$

- Quadratic regression model

$$f_{qu,i} = \alpha x_1^2 + \beta x_2 + \varepsilon \quad (24)$$

- Exponential regression model

$$f_{in,i} = \alpha e^{x_1} + \beta x_2 + \varepsilon \quad (25)$$

Where:

- x and x' are linear combination of the independent variables and the linear combination of the logarithmic independent variables respectively
- x_1 and x_2 are linear combinations of heat source parameters
- ε is the intercept
- α and β are regression coefficients

2.1.5 Verifying methods

Once we have defined all the possible equations for regression, we can choose between two verifying methods: temperature method and residual stress method.

The first method is the most used: it consists of measuring temperatures at specific points and fitting the heat parameters to match the simulated temperature with the experimental one. Then, the parameters can be further refined observing the macrographs of cross-sections.

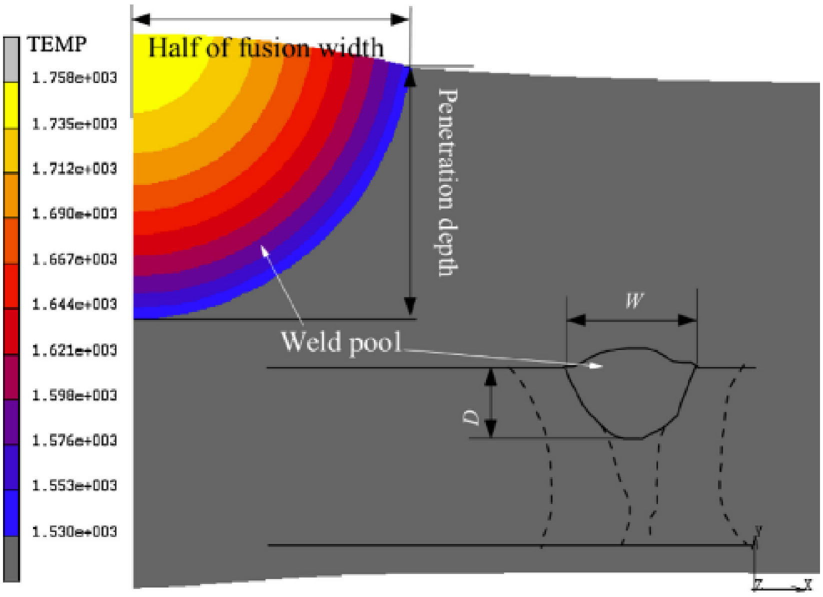

Figure 2.8 : Weld pool measurements for temperature method

The peak temperature T_p can also be taken into account in the matching, because it has critical influence on temperature gradient and, therefore, on the heat affected zone.

Finally ten parameters are involved in the simulation:

- Q, η and v are considered fixed values
- a, b, c_f, c_r are the independent input parameters
- D, W, T_p are the output values of welding pool

After cutting transverse sections of the weld bead, the evaluation of depth, width and peak temperature, is carried out thanks to the traditional method of grinding, polishing and etching, which allow us to analyze the metallographic structures with a microscope.

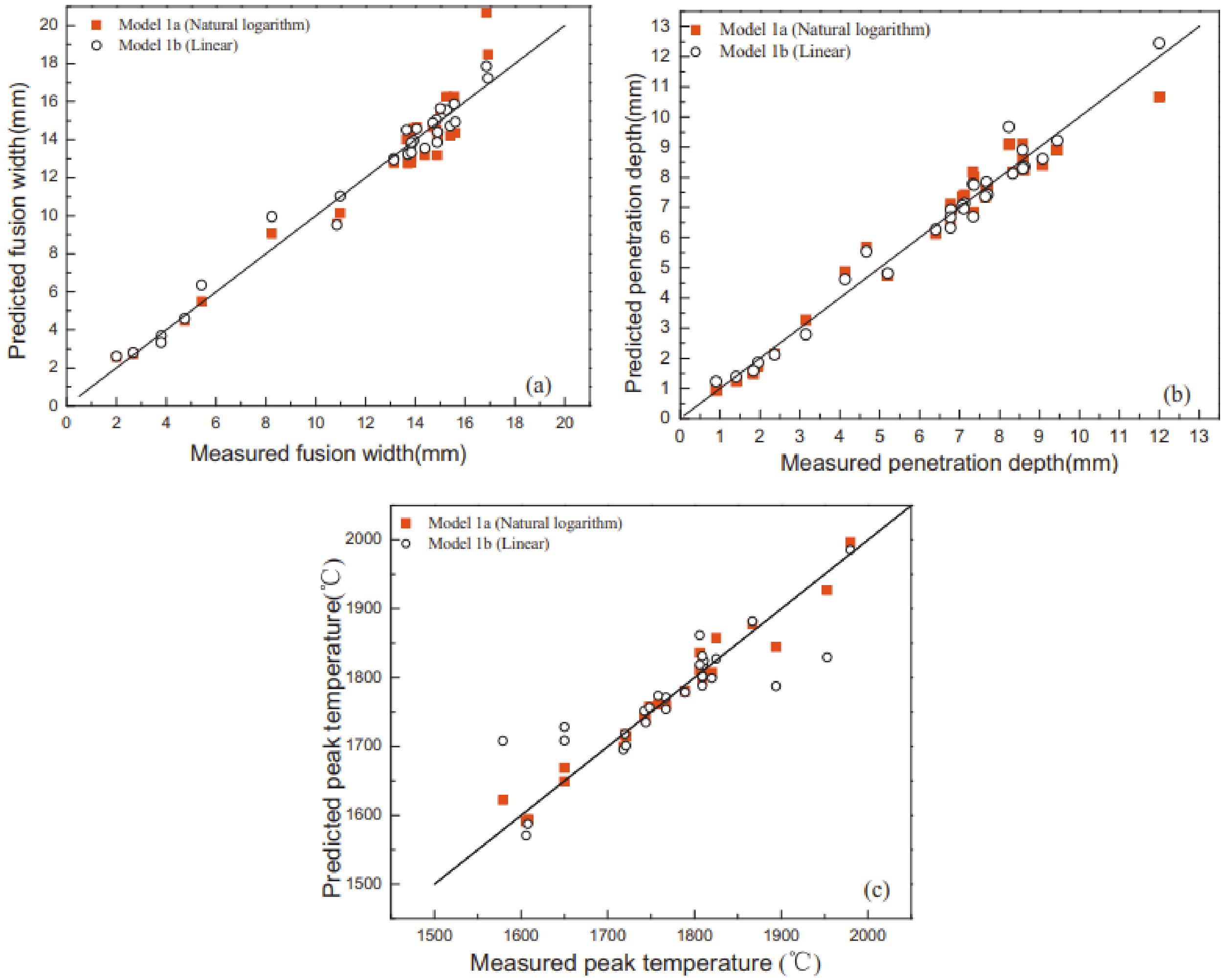

Figure 2.9 : Measured and predicted MRA width, depth and peak temperature

As we can observe from the figures there are no significant differences in the accuracy of predicted results between model 1a and model 1b for W (width) and D (depth). For the peak temperature however, the results obtained with the natural logarithm method seemed much better than the linear model.

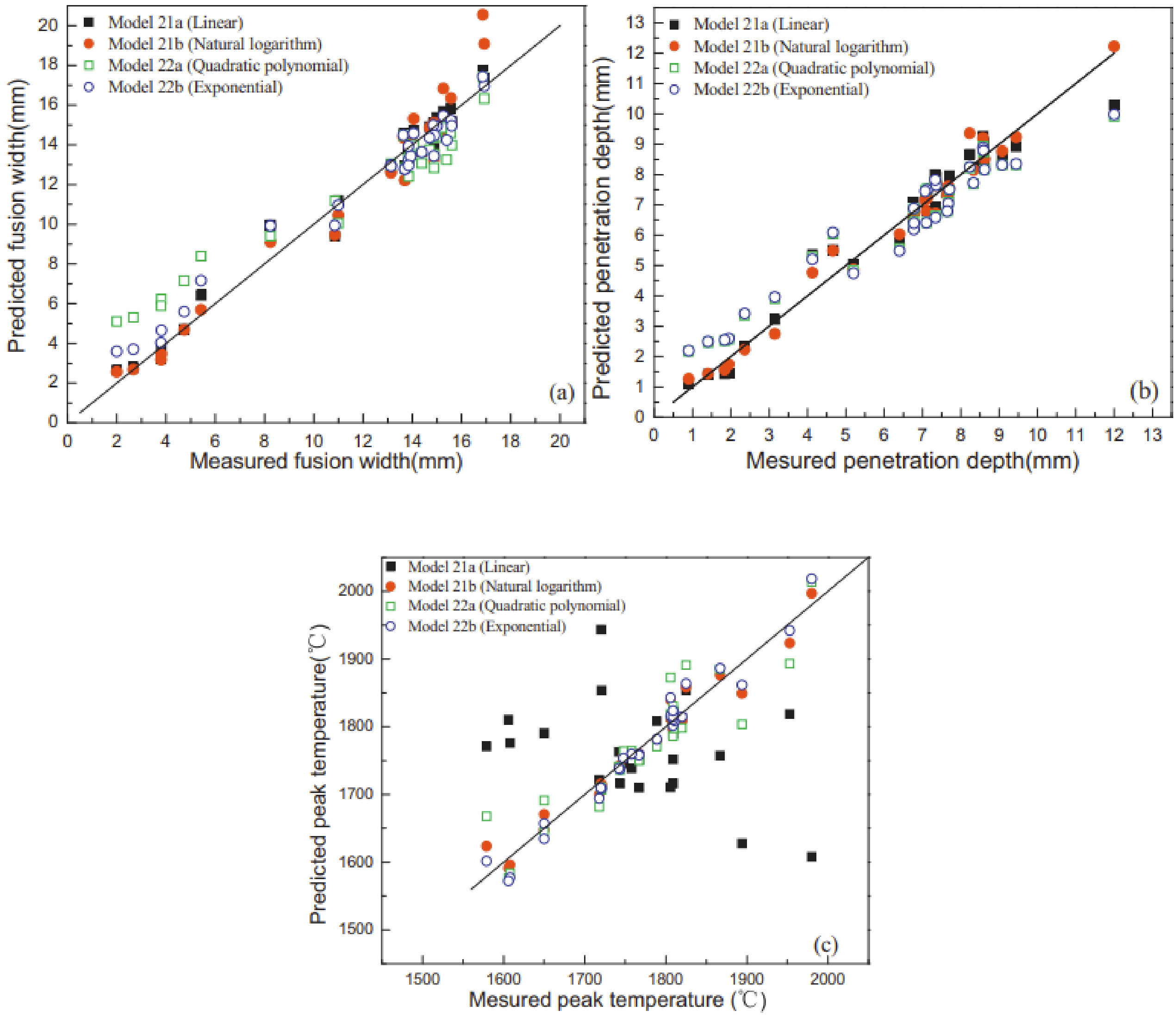

Figure 2.10 : Measured and predicted PLSRA width, depth and peak temperature

On the other hand, looking at the results of the PLSRA methods, it is clear that both model 21a and 21b give us solutions which are similar to those obtained from the MRA model, regarding the fusion width and the penetration depth. For the peak temperature, instead, models 22a and 22b seemed to be more accurate in matching with experimental data.

However a simplified way to define the parameters of double-ellipsoidal heat source is to directly refer to experimental macrograph [6] in such way that dimensions of the melted area in the simulation are the same as weld bead dimensions.

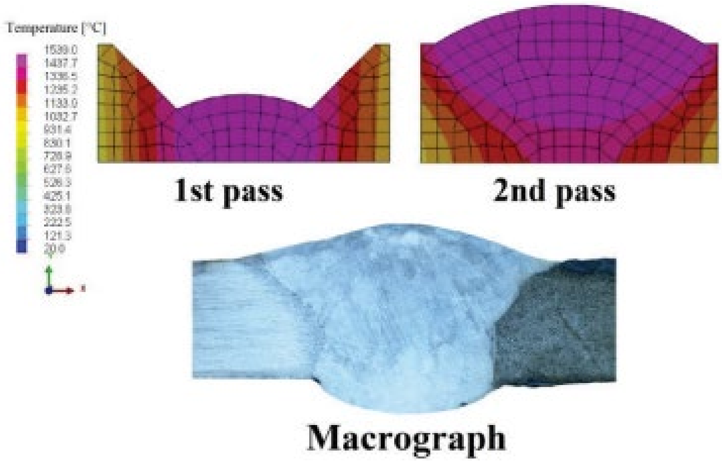

Figure 2.11 : Comparison between experimental macrograph and numerical model of melted area

2.1.6 Global sensitivity analysis

Now that we have studied several methods to compare the experimental data with the simulation, in the work [7] a global sensitivity analysis has been carried out to define which are the input parameters that mostly influence the variability of the results. This procedure will lead us to avoid doing numerous difficult and expensive experiments. In order to do so, only the most relevant properties need to be measured with a good accuracy, while the others can be simply extrapolated or taken from a similar material. For the elastoplastic mechanical model taken into account in this paper, for example, only three of the 35 input parameters explains 90% of the output variability.

For the same reason in [8] they tried to evaluate the influence of the change in welding heat input on welding simulation results, in particular fatigue crack propagation (FCP) and stress intensity factor (SIF).

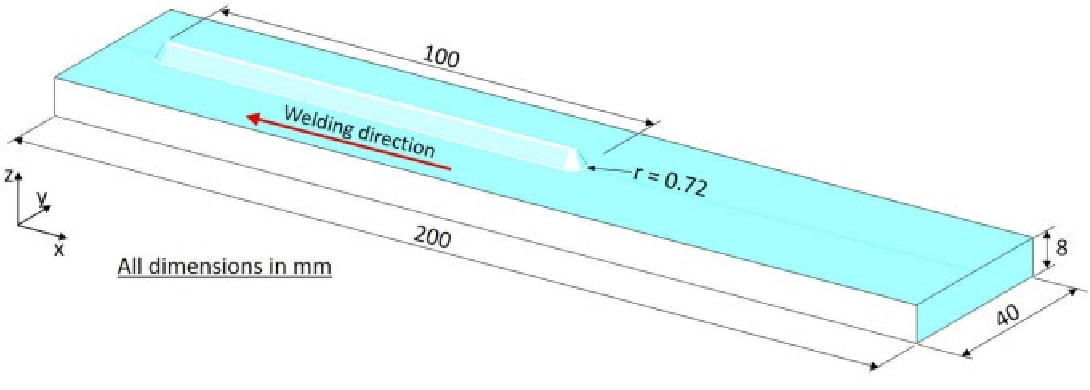

Figure 2.12 : Welding sample for global sensitivity analysis

From the following figure we can easily observe that when the HI increases the induced welding RS decreases, due to the increase of the average temperature that brings to a general decrease of the restraint of the model.

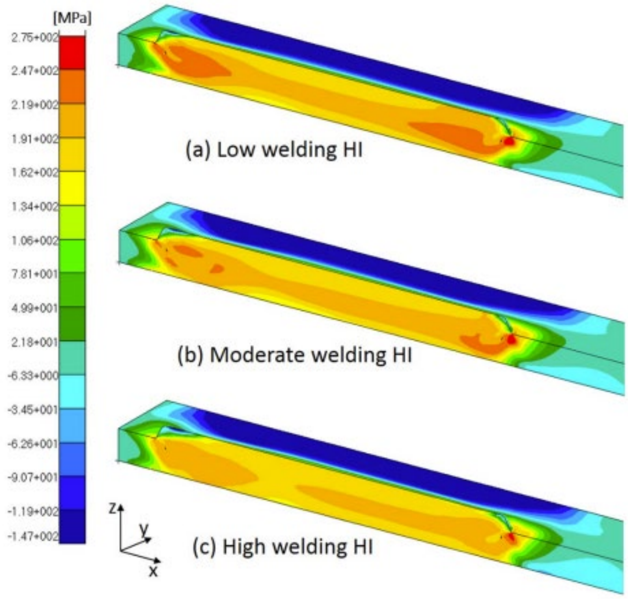

Figure 2.13 : Effect of heat input variations on Residual Stress

On the other hand, as it is probably more predictable, welding distortion increases when heat input increases. This phenomenon is strictly correlated to the non-uniform expansion and contractions of the material during thermal cycles.

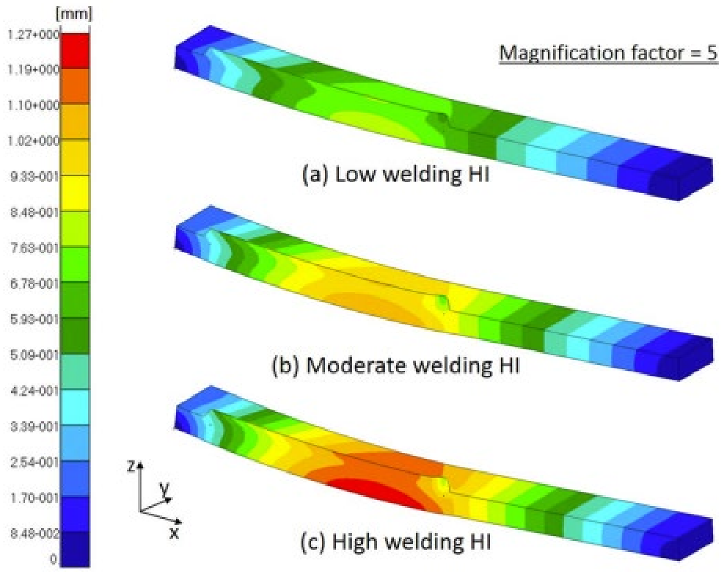

Figure 2.14 : Effect of heat input variations on Distortion

In conclusion of this analysis we can say that changing the HI has a great influence on RS distribution but it also has almost no influence on RS magnitude.

2.1.7 New heat source models

As we have already mentioned before, a good way to evaluate the accuracy of the heat source model is to compare the experimental weld profile of the fused zone with the numerical simulation. In the work [2] an interesting analysis of two different materials (carbon steel and stainless steel), two thicknesses (3 and 6 mm), two welding methods (GTAW and GMAW) and four heat source models (Conical, Goldak, VCP and FVP) has been carried out.

Conical and Goldak model are the most used, even though conical model is preferred to simulate electron-beam melting or laser power sources.

On the other hand, new heat sources such as Variable Conical Profile (VCP) and Full Variable Profile (FVP) are based on the fact that the information of the heat input distribution must be taken into account in the formulation. In the FVP source, for example, the maximum power density decays along the thickness. Both these sources shapes are defined by the Fusion Zone boundary experimentally measured and they have the advantage of relying on a single equation with a low number of geometric parameters.

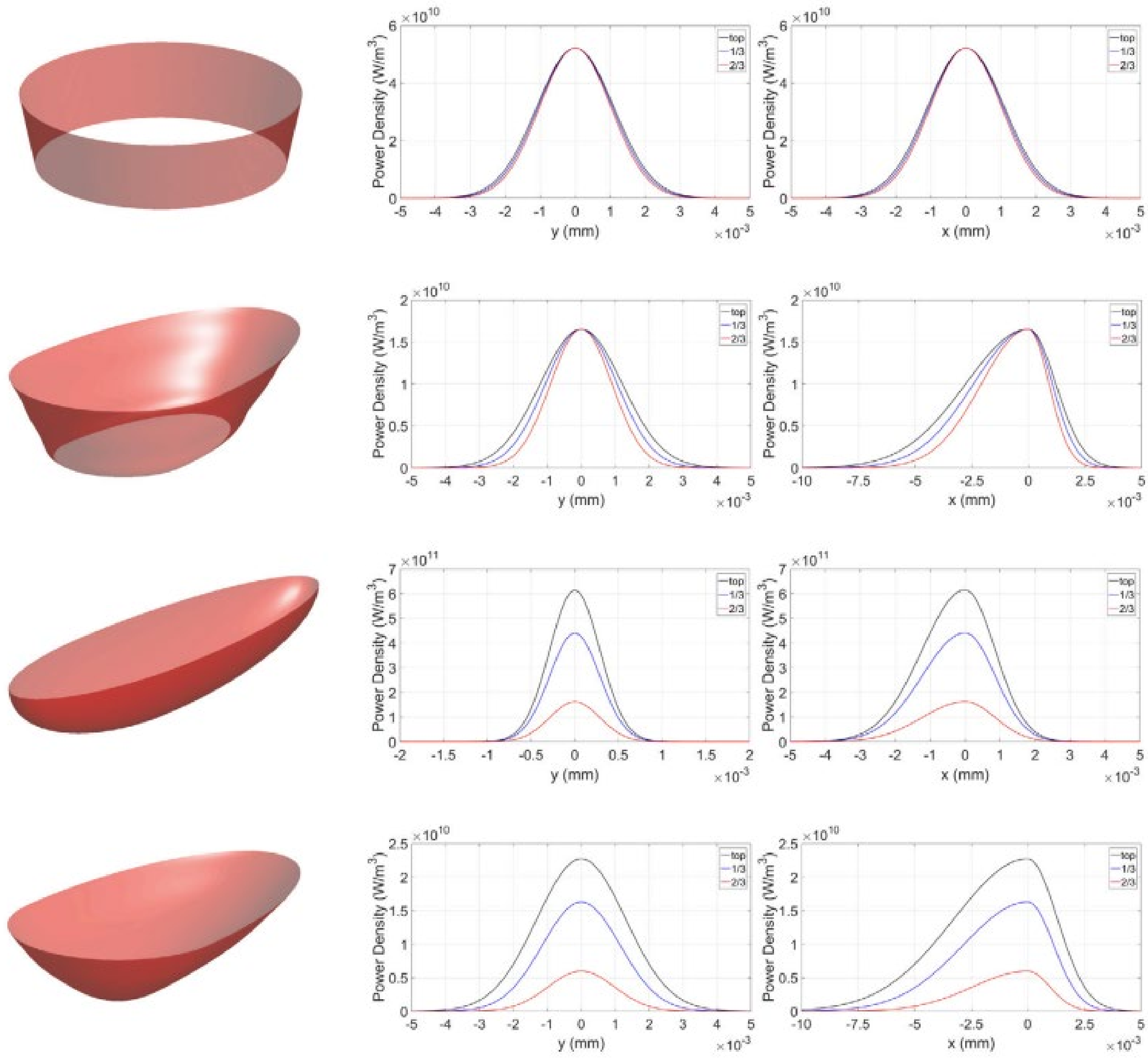

Figure 2.15 : Alternative heat sources and power density distribution over x and y axes

In the case of GTAW with 3mm thickness the NRMSE (Normalized Root Mean Squared Error), obtained comparing real with simulated temperatures along the weld bead, is lower than 1.6% for carbon steel and lower than 4% for stainless steel. This example shows that even if new heat sources are more accurate, especially with stainless steel, traditional model as Goldak give us still acceptable results.

Another way to evaluate the heat source model accuracy is to compare the experimental (yellow line) with the simulated (black dotted line) weld profile and their related temperature distributions. In this example all four models returned very good results for carbon steel and slightly less accurate but still acceptable results for stainless steel.

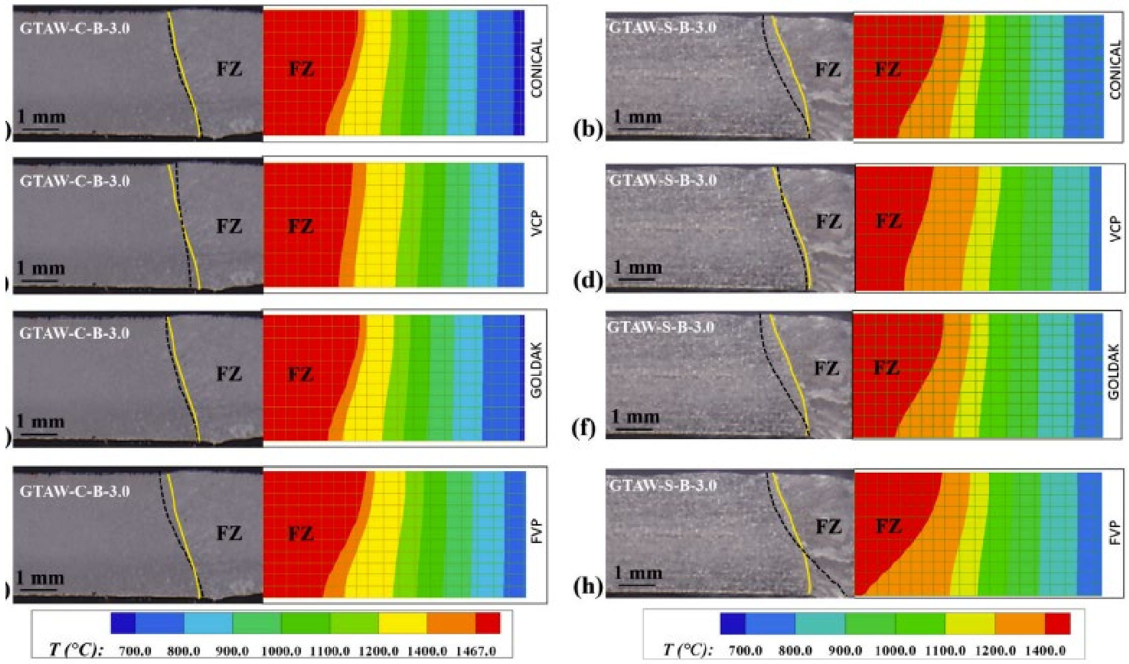

Figure 2.16 : Comparison between experimental and simulated weld profile with SMAW method

2.1.8 Thermal model validation

To enrich the data set that will be useful to compare experimental data with simulation, in the work [9] an analysis of two different welding procedures has been carried out: a double pass GTAW and a five-pass SMAW. Using thermocouples placed at 10mm, 15mm and 20mm from the weld bead it is possible to validate the predicted thermal cycles.

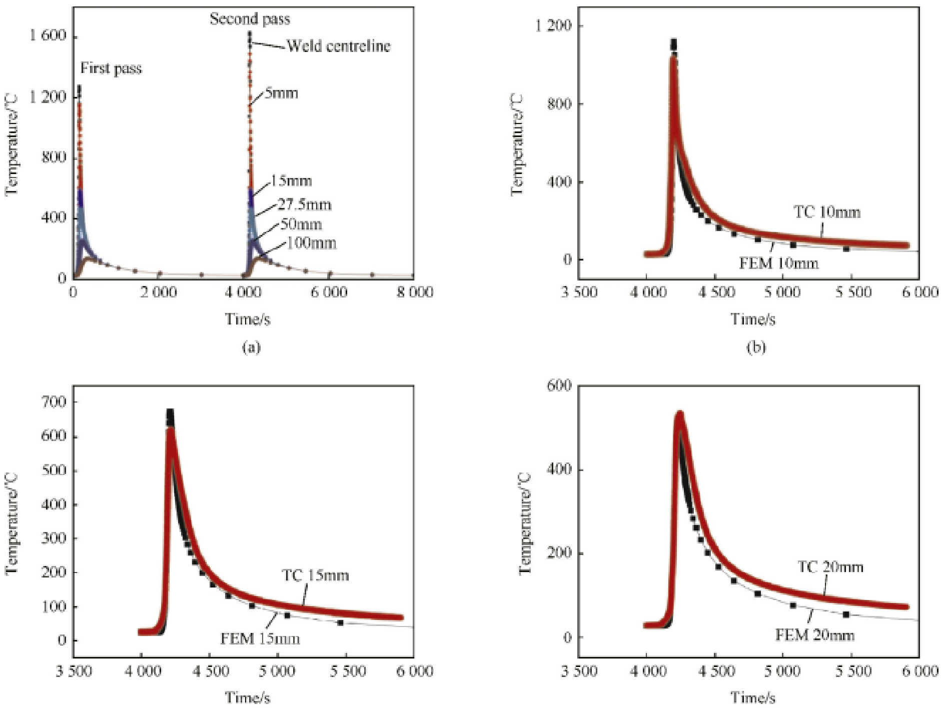

Figure 2.17 : Double pass GTAW thermal model validation with thermocouples

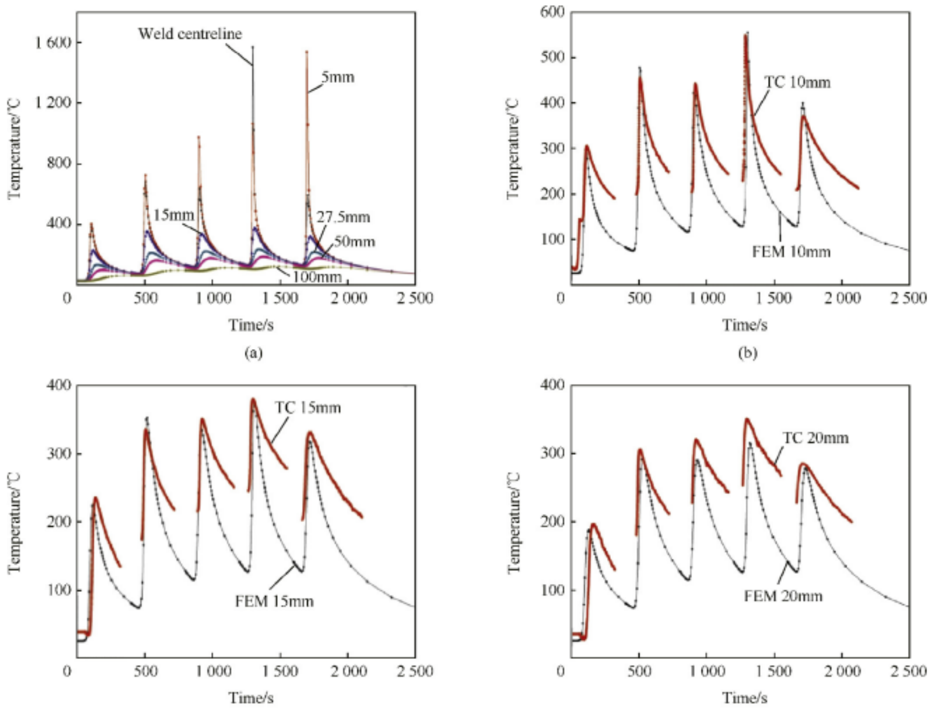

Figure 2.18 : Five-pass SMAW thermal model validation with thermocouples

In both cases the peak temperatures match each other quite well and slowly decrease with the increasing measuring distance from the weld bead. The only difference is that the cooling rate of the thermocouples is quite slower compared to the simulated one. The higher heat input of 5kJ/mm for GTAW instead of 2kJ/mm for SMAW resulted in higher temperatures in the GTAW process. In this work it was demonstrated that using large heat inputs reduces the cooling rate, so that larger quantities of Widmanstatten ferrite are obtained, reducing the quantity of acicular ferrite. The GTAW weld joint, in this case, will have a lower impact toughness compared to the SMAW weld joint.

2.1.9 Residual stress analysis

At this point, in the same work [9], a residual stress analysis has been carried out using two different techniques: X-ray diffraction (XRD) and longitudinal critically refracted waves (LCR). The XRD is more sensible to surface conditions with depth between 5 and 30 micron while with LCR residual stress is the average over effective penetration of 3mm. These results are compared to a FEM simulation obtained with SYSWELD.

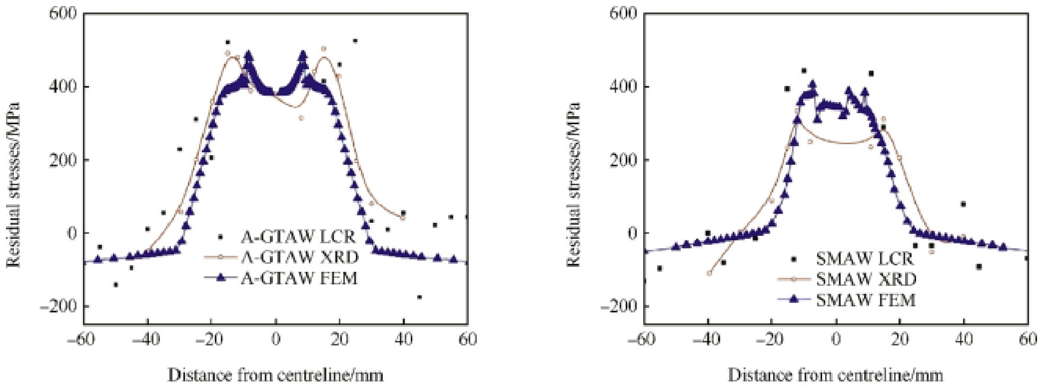

Figure 2.19 : Residual stress analysis – Comparison between FEM, LCR and XRD methods

In both cases the distribution of residual stresses is similar (tension near the weld bead and a little compression on the base material) and experimental values seem to be comparable with the numerical prediction.

2.1.10 Heat source parameter estimation

As we have already mentioned before, there are three main acceptable methods to compare parameter fitting of the heat source model:

- Measuring temperatures with thermocouples
- Measuring residual stresses with destructive or non-destructive techniques at specific points
- Observing geometric dimensions of the fusion zone, molten pool and heat affected zone (HAZ) with macrographs of cross-sections

In particular, as described in the work [10], we will now discuss about the third method.

In addition to comparing cooling curves, the most relevant results are obtained by comparing microstructures and macrographs between the FE meshed model and the experimental results. This experiment was made up of two overlapping beads on a substrate steel plate, joined with GMAW method.

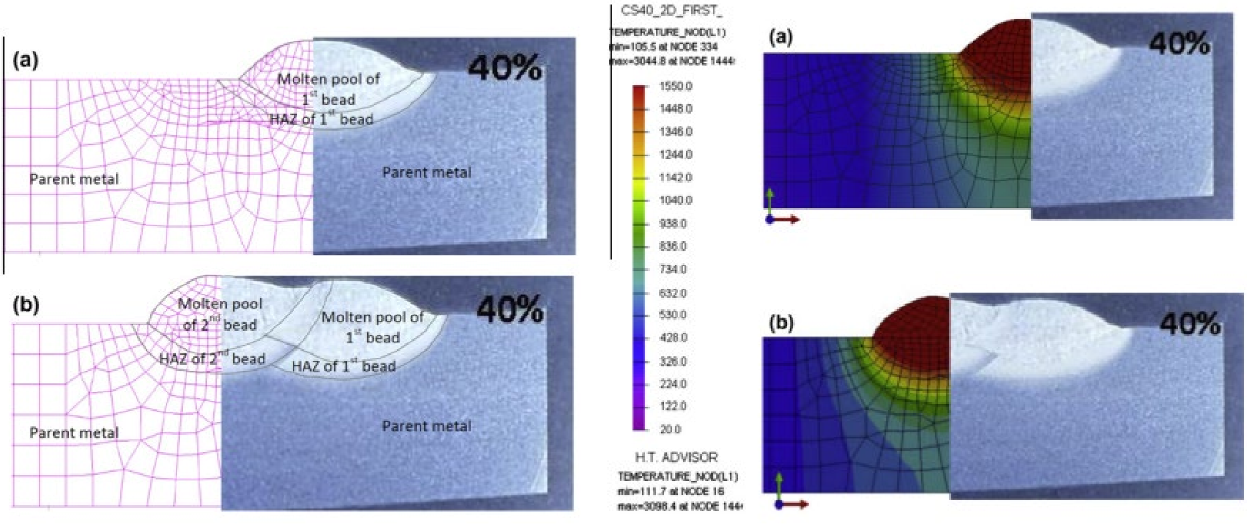

Figure 2.20 : GMAW Macrographs comparison

Observing the percentages of the different microstructures at the end of the process, they were able to define the Goldak model parameters that fitted the experimental curves and dimensions.

As mentioned earlier, another effective method is to compare the temperature profiles obtained with thermocouples [11].

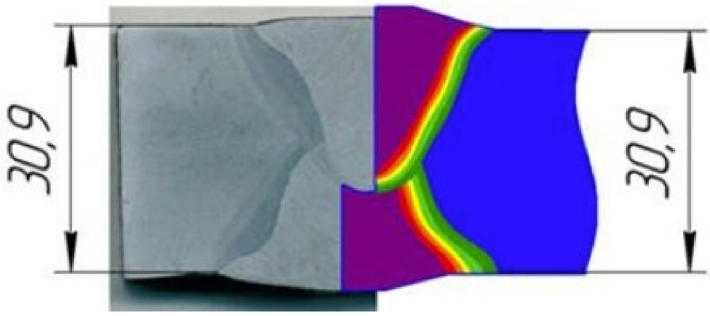

Figure 2.21 : Numerical and experimental comparison on thermal distribution

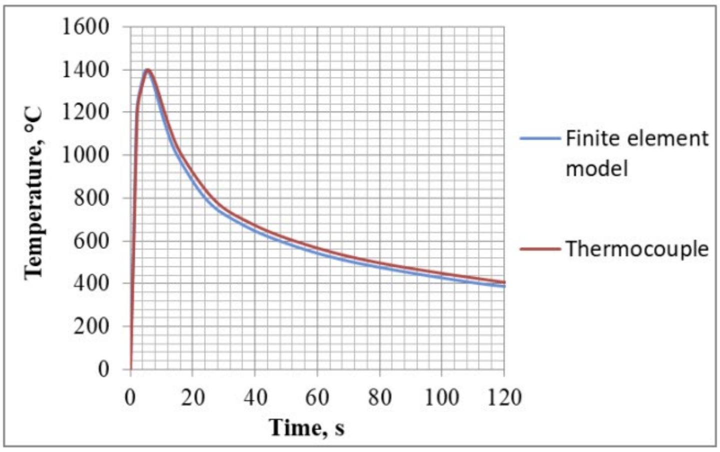

Figure 2.22 : Comparison between FEM temperature profile and thermocouple measurements

Each kind of welding process has its own peculiarities which can therefore make adjustments to certain parameters more or less important. In the work [12], for example, a MIG welding is taken into account. Here the most important parameters are:

- Arc current
- Wire feed rate
- Workpiece thickness
- Welding speed

By tuning these parameters the performance of the arc welding can be predicted. In particular we will focus our attention on the relationship between workpiece thickness and arc current. In the next figure we can summarize the data flow of the simulation result.

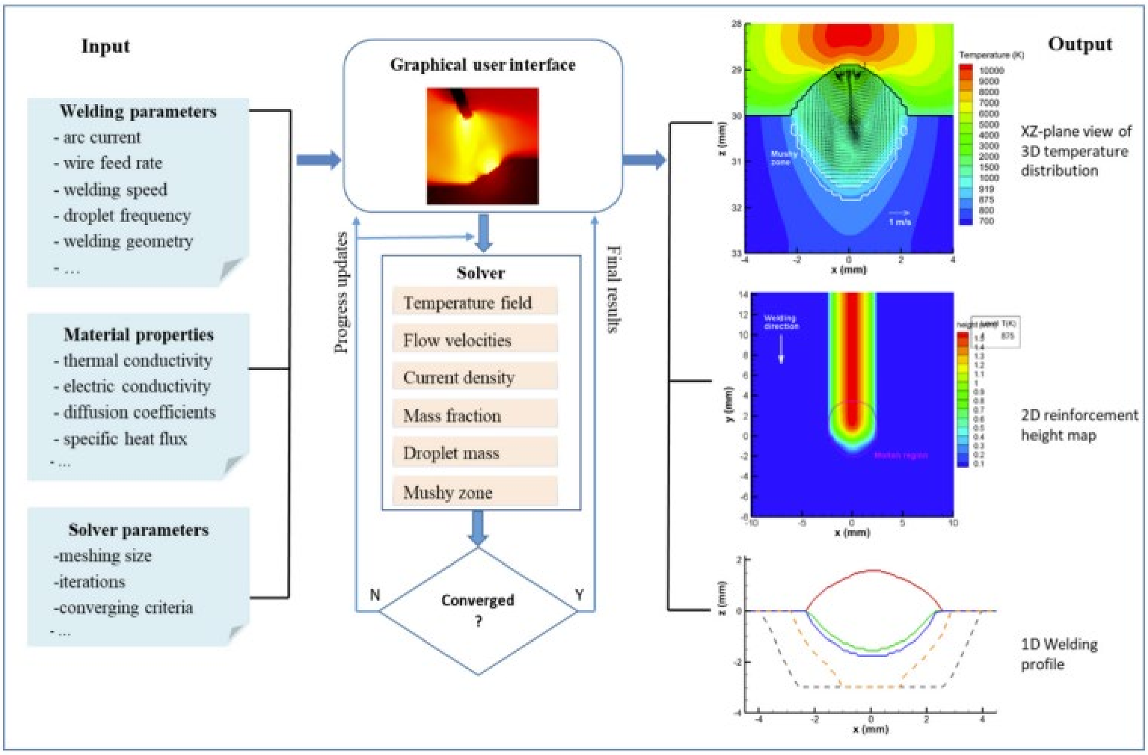

Figure 2.23 : Optimal procedure for accurate model definition

2.1.11 Arc current effect on penetration and thickness

As a general rule higher arc current is usually used for welding thicker workpieces; to generate higher temperatures and to facilitate this process, the welding speed can be reduced, in order to generate a deeper welding pool.

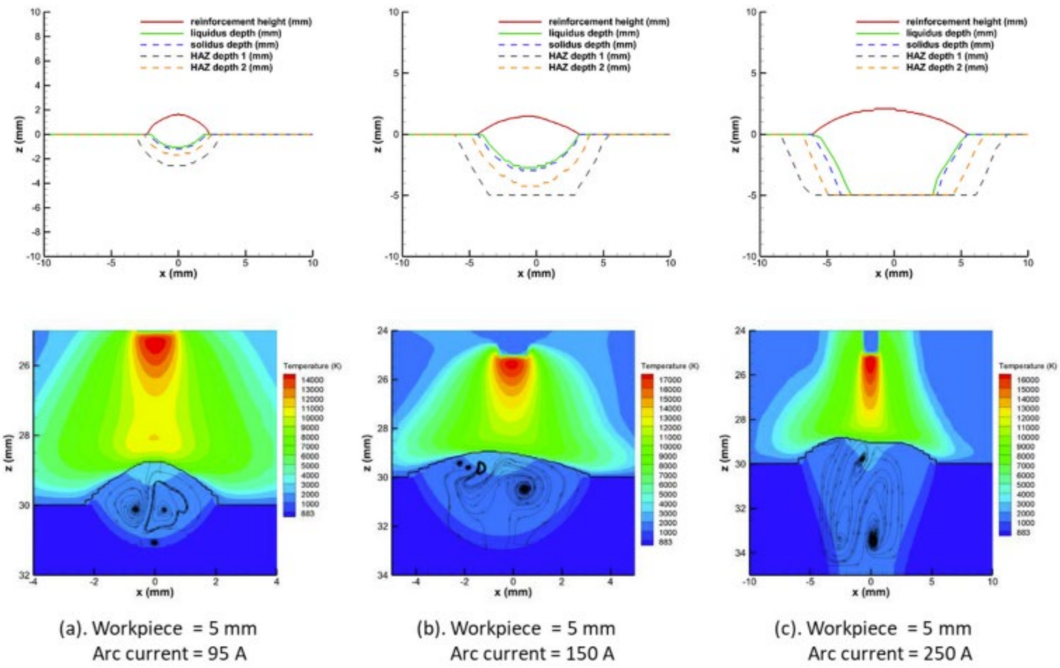

Figure 2.24 : Effect of arc current on penetration

As we can easily observe a too low current generates insufficient heat for significant penetration, while a too high current produces a very large region that penetrates through the bottom of the workpiece. For this reason it is easy to see how if the thickness of the pieces increase also the arc current have to increase proportionally, so that each single separation line (liquidus, solidus and HAZ) it is still distinguishable from the others [12].

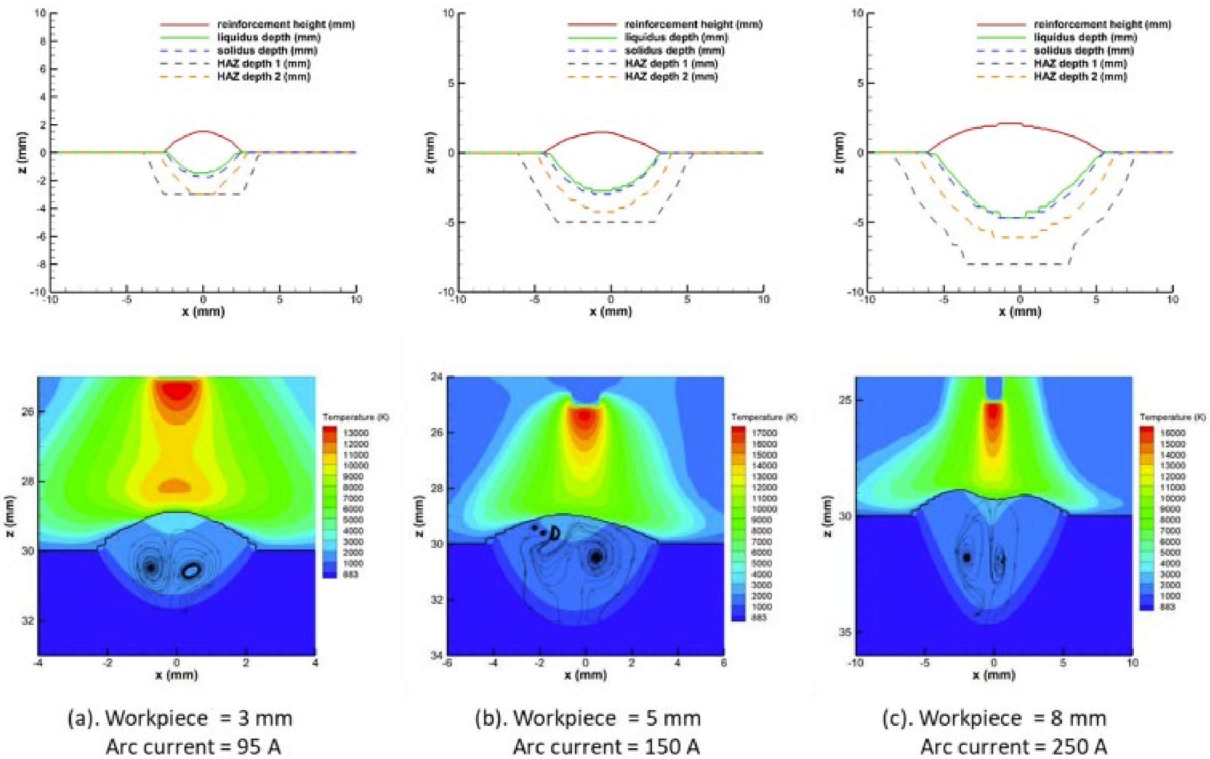

Figure 2.25 : Effect of arc current and thickness on penetration

2.1.12 Microstructures analysis

At this point, another analysis which could be useful to our simulation is to study the impact that the variation of heat input and the type of welding have on microstructures and toughness. In the work [9] a comparison between the base material and the weld joints (SMAW and GTAW) has been made to predict the characteristics of the material.

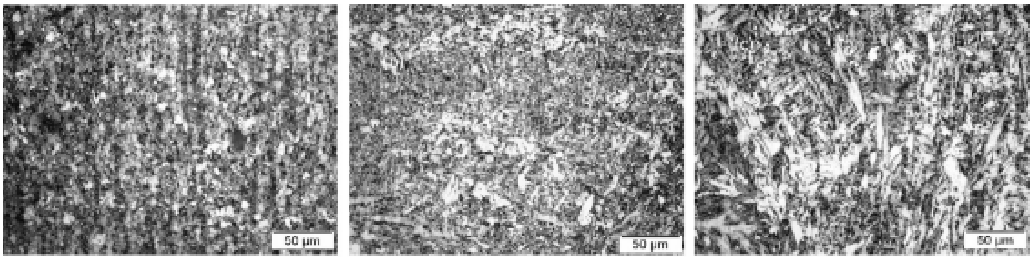

Figure 2.26 : Optical images of base metal, SMAW joint and GMAW joint

The base metal is predominantly composed of fine grained equiaxed ferrite and some pearlite. Whereas welded joints showed grain boundary ferrite, Widmanstatten ferrite, acicular ferrite and microphases. The typical M shape profile of Residual Stress is probably due to the phase transformations of equiaxial ferrite to grain boundary ferrite (reconstructive), acicular and Widmanstatten ferrite and bainite (displacive), which causes volume changes.

Then a test to evaluate and compare the impact toughness of the two different welding processes has been carried out, showing that GTAW gives us slightly better results.

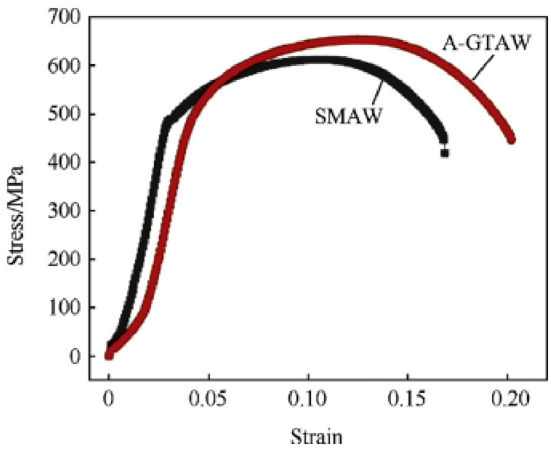

Figure 2.27 : Stress vs Strain curve for SMAW and GMAW joint

Finally a micro hardness test has been made at two different depths, showing that GTAW has a more regular distribution moving from the center of the weld to the base material.

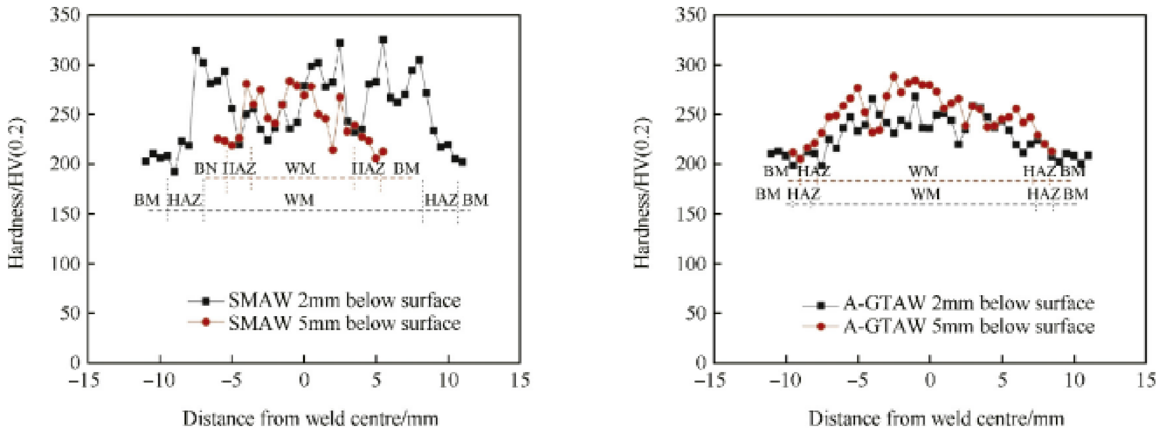

Figure 2.28 : Vickers hardness test for SMAW and GMAW joints

The evaluations made in [13] showed that the hardness decreases with increase in the heat input, while the toughness first increases and then decreases. However we have to remember that all the changes involved in the microstructures strongly depend on temperature heating and cooling rate and for this reason, different results can be achieved depending on the type of welding.

In the next figure we can observe an example of how the microstructure of a HAZ evolves at four different cooling rates, measured as the time taken to cool from 800 °C to 500 °C ($t_{8/5}$): 10s, 20s, 60s and 120s. In fact, the faster the cooling rate, the more displacive transformations are favored: this leads to the formation of martensite and bainite.

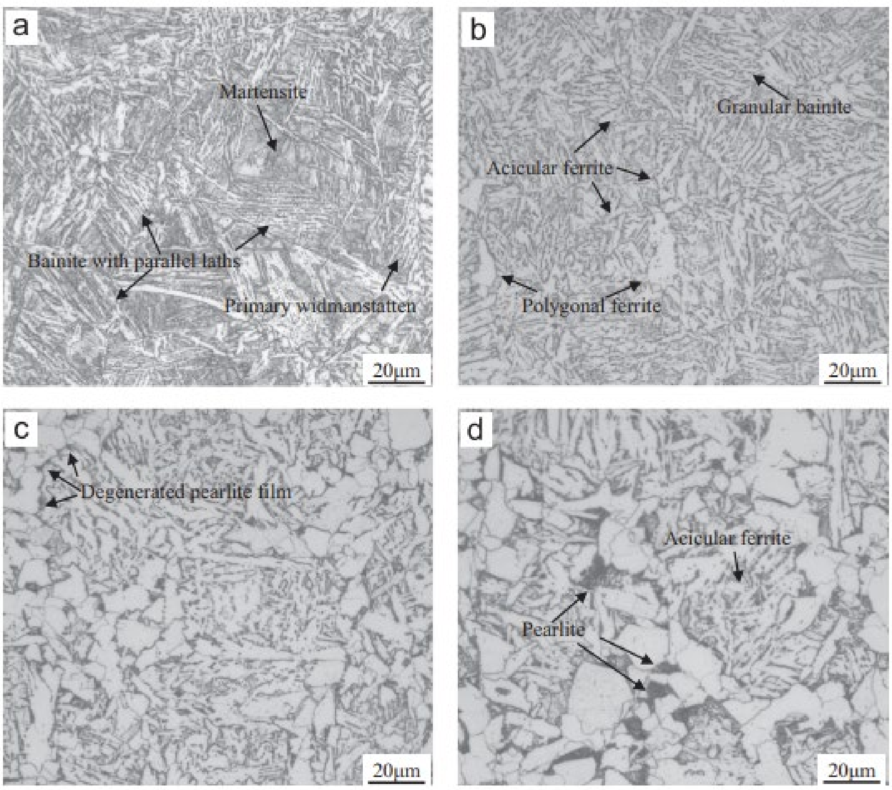

Figure 2.29 : Microstructures after four different cooling rates

In general we can summarize the material behavior and its microstructure as follows:

- with low heat input it is mainly composed of martensite and bainite, making the structure hard but fragile
- with medium heat input it consists of acicular and polygonal ferrite and granular bainite, maximizing the total impact energy
- with high heat input it is mainly composed of ferrite and pearlite, which decreases the hardness

Finally in the work [14] a thermal–metallurgical model is developed to predict the temperature fields and spatial distribution of volume fraction of phases during laser beam welding of 1020, 1045, and 1060 steels. In particular their model is focused on the different thermal properties of each phase, considering that a higher thermal conductivity leads to a lower temperature.

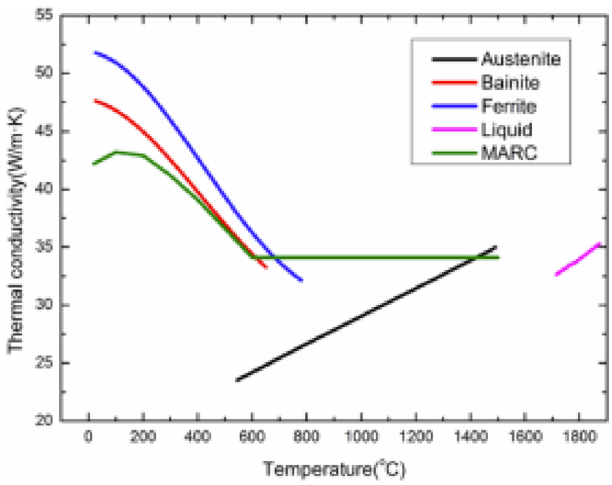

Figure 2.30 : Thermal conductivity depending on temperatures and phases

After comparing the conduction model with the experimental measurements and demonstrating that the temperature distributions curves matched quite well for each material, we can now observe the microstructure of weld at the centerline of the three steel and compare it with the simulated results.

Here it is visible how the starting material can strongly influence the evolution of the distribution and quantity of the different microstructures along the weld bead. Here in particular, the different distributions of ferrite and pearlite are shown.

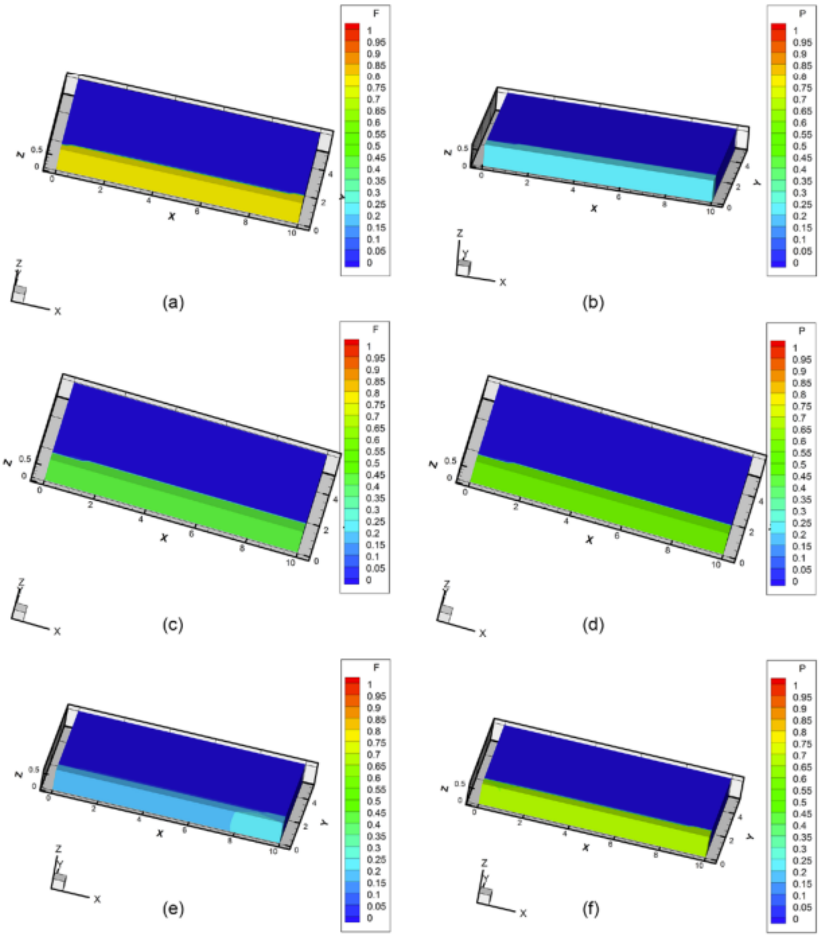

Figure 2.31 : Distribution of ferrite and pearlite on three different steel : 1020, 1045, 1060

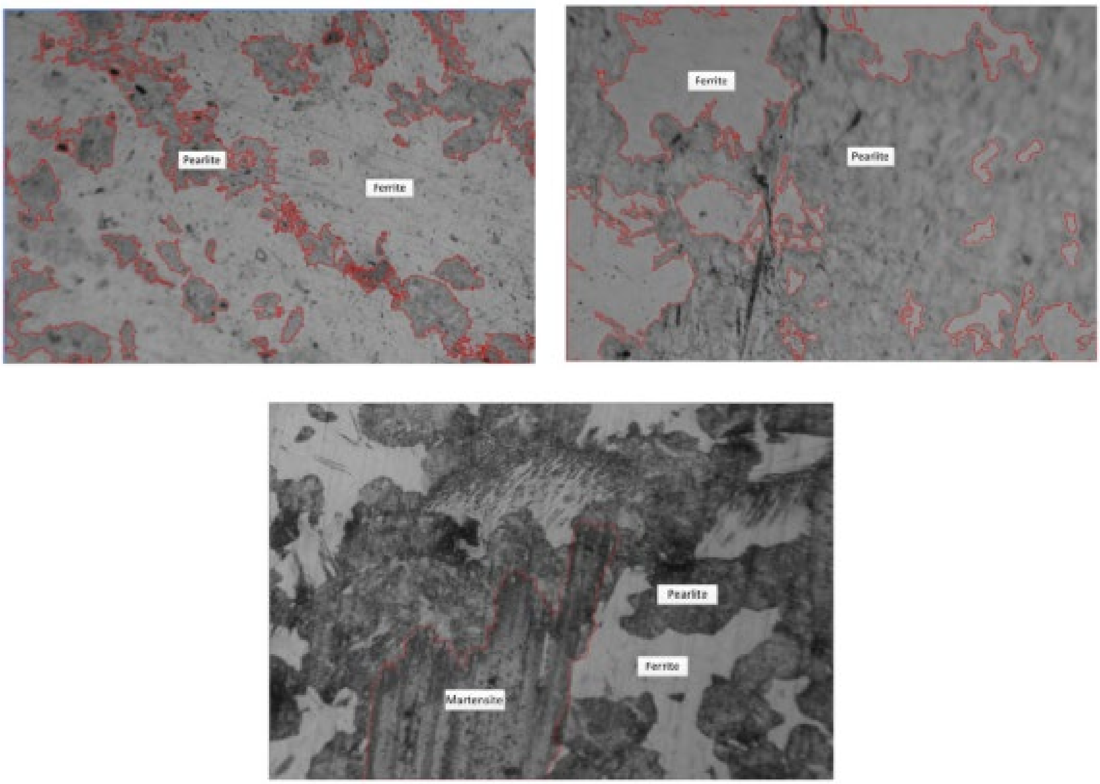

Figure 2.32 : Micrographs and phases of 1020, 1045 and 1060 steel

From experimental analysis after welding, the 1020 and 1045 steels show a ferritic and pearlitic structure while the 1060 also shows martensite formation. From this analysis it is possible to evaluate the accuracy of the model comparing these distributions of microstructures with those of the simulation.

2.2 Active thermography

2.2.1 Physical laws

Among the most used thermographic techniques, flying spot thermography is an efficient non-destructive test to detect surface breaking cracks [15]. After heating the surface with a moving laser spot, surface temperature distribution is recorded with an infrared camera. The presence of a crack is highlighted by a discontinuity in the temperature field on the surface, due to the fact that the presence of a defect itself changes the way heat is transmitted. This study will mainly discuss about thermal diffusivity and determination of the width of cracks.

Basically this phenomenon is based on the photothermal effect, which consists in heat generation by light absorption. The heat is first generated at the surface and then propagates, by conduction, into the bulk.

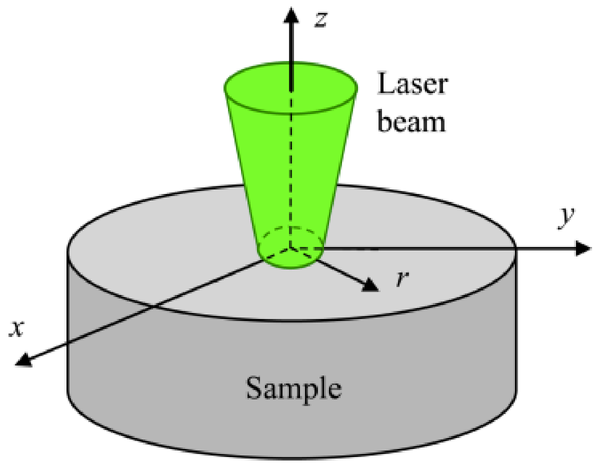

Figure 2.33 : Example of laser beam effect on a workpiece

To introduce this analysis let's consider a continuous wave laser of power P_0 harmonically modulated at frequency f. As a direct consequence, the sample temperature oscillates at the same frequency. This phenomenon is based on the modified Helmholtz equation:

$$\nabla^2 T(r,z) - q^2 T(r,z) = 0, \quad (26)$$

Where $q^2 = i\omega/D$, with D being the thermal diffusivity.

After a few passages, considering the Hankel transform space and boundary conditions with prescribed heat flux, we obtain an equation that fully illustrates the Gaussian temperature trend in all directions, for an infinitely small laser spot (a=0).

$$\frac{d^2\tilde{T}(\delta, z)}{dz^2} - \beta^2\tilde{T}(\delta, z) = 0. \tag{27}$$

$$\tilde{T}(\delta, z) = A(\delta)e^{\beta z} + B(\delta)e^{-\beta z}, \tag{28}$$

$$-K\frac{d\tilde{T}}{dz}\bigg|_{z=0} = \frac{\eta P_o}{4\pi} e^{-\frac{(\delta a)^2}{8}}, \tag{29}$$

$$\tilde{T}(\delta, z) = \frac{\eta P_o}{4\pi K}\frac{e^{\beta z}}{\beta} e^{-\frac{(\delta a)^2}{8}}. \tag{30}$$

$$T(r, z) = \frac{\eta P_o}{4\pi K}\int_0^\infty \delta J_o(\delta r)\frac{e^{\beta z}}{\beta} e^{-\frac{(\delta a)^2}{8}} d\delta, \tag{31}$$

$$T(R) = \frac{\eta P_o}{4\pi K}\frac{e^{-\sqrt{\frac{i\omega}{D}}R}}{R} = \frac{\eta P_o}{4\pi K}\frac{1}{R}e^{-\frac{R}{\mu}}e^{-i\frac{R}{\mu}} = |T|e^{-i\Psi}, \tag{32}$$

Where:

- R = $\sqrt{x^2 + y^2 + z^2}$
- |T| and Ψ are the amplitude and phase of the temperature oscillation
- μ = $\sqrt{\frac{D}{\pi f}}$ is the thermal diffusion length
- η is the power fraction absorbed by the sample
- K is the thermal conductivity

To simulate a Dirac laser pulse of energy Q_0 the following equation has been used:

$$T(x, y, z, t) = \frac{\eta Q_o}{8K\sqrt{D}}\frac{1}{(\pi t)^{3/2}}\int_{-\infty}^{\infty} dx'\int_{-\infty}^{\infty}\frac{2e^{-\frac{2(x'^2+y'^2)}{a^2}}}{\pi a^2}e^{-\frac{(x-x')^2+(y-y')^2+z^2}{4Dt}}dy' = \frac{\eta Q_o}{\varepsilon\sqrt{\pi^3 t}}\frac{e^{-\frac{z^2a^2+8Dt(x^2+y^2+z^2)}{4Dt(a^2+8Dt)}}}{a^2+8Dt} \tag{33}$$

Where ε = K/$\sqrt{D}$ is the thermal effusivity of the sample.

We can now consider two particular cases: the gaussian profile of the surface temperature field and the case of a tightly focused spot (a=0). We can easily observe how the peak of the gaussian profile progressively decreases with time.

$$T(r,0,t) = \frac{\eta Q_o}{\varepsilon\sqrt{\pi^3 t}} \frac{e^{-\frac{2r^2}{a^2+8Dt}}}{a^2+8Dt}, \tag{34}$$

$$T(r,0,t) = \frac{\eta Q_o}{8\varepsilon D\sqrt{\pi^3 t^3}} e^{-\frac{r^2}{4Dt}}, \tag{35}$$

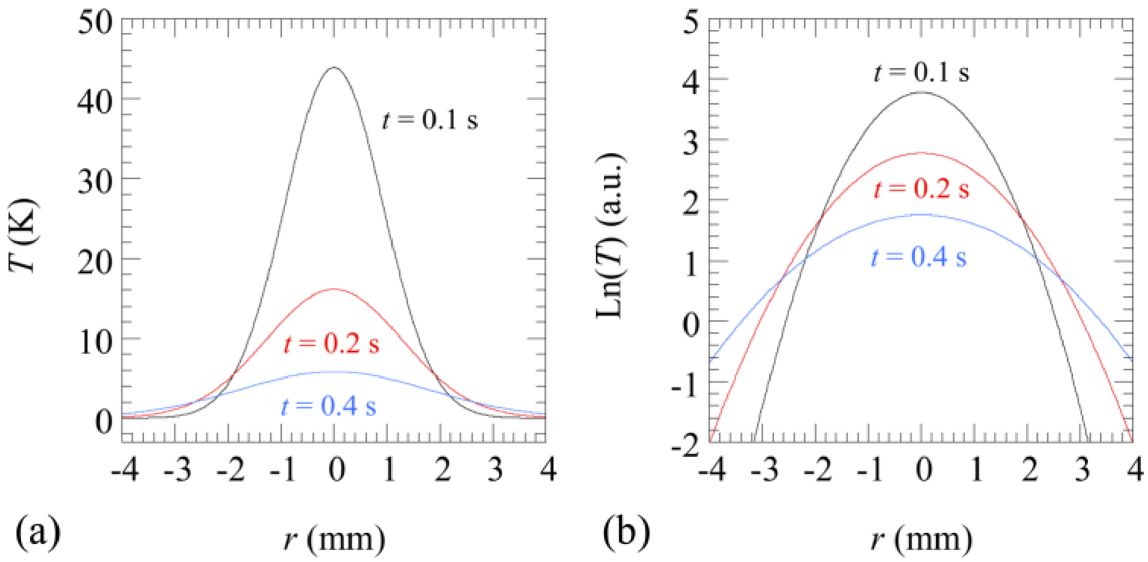

Figure 2.34 : Temperature distribution without defect over time

To evaluate the effect of a defect, three different crack widths are considered at two times after the pulse (75ms and 100ms). In this experiment an infinite vertical crack positioned at plane x=0 is detected by a Dirac laser pulse of energy 1J with a radius of 0.4 mm and centered at d = 1 mm.

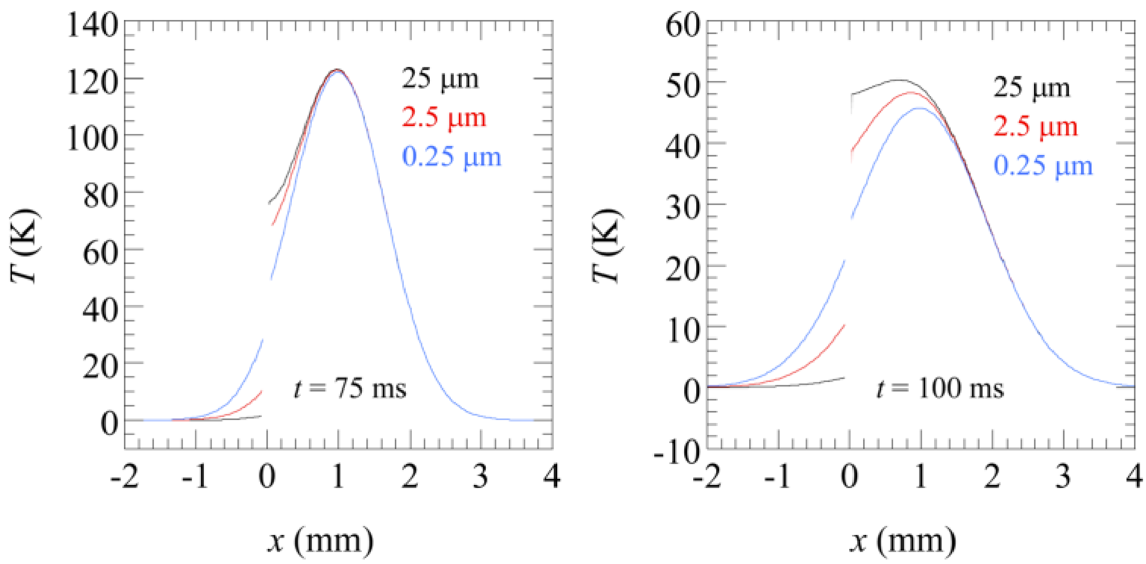

Figure 2.35 : Temperature distribution with three different defects at two times after the pulse

If we want to analyze what happens when the laser is moving along the workpiece, we need to use a more complex equation.

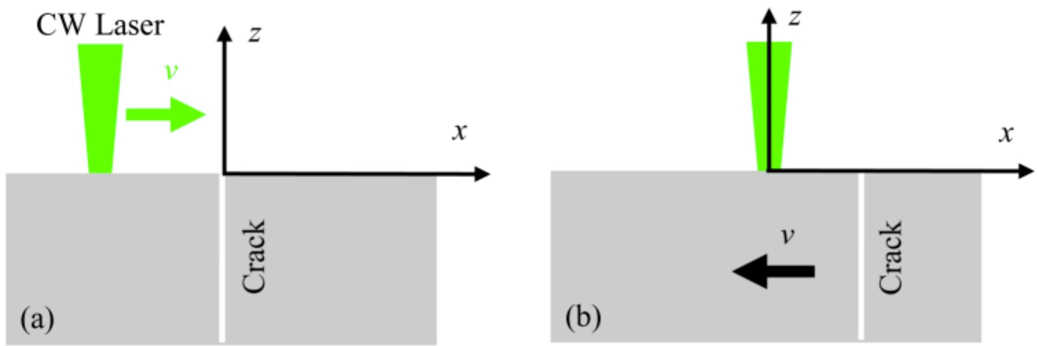

Figure 2.36 : Example of a moving laser beam on a workpiece

Thanks to a simple Galilean transformation, we obtain the temperature profile with the material moving at constant velocity and the workpiece at rest, which is more useful from the point of view of industrial processes.

$$T(x,0,0,t) = \frac{2P_o\eta}{\varepsilon\sqrt{\pi^3}}\int_{t_o}^{t}\frac{1}{\sqrt{t-\tau}}\frac{e^{-\frac{2(x-v\tau)^2}{a^2+8D(t-\tau)}}}{a^2+8D(t-\tau)}d\tau + sign(x)\frac{P_o}{\varepsilon\pi^2 a\sqrt{D}}\int_{-\infty}^{\infty} sign(x_o)dx_o\int_{t_o}^{t} d\tau\frac{1}{t-\tau}\frac{e^{-\frac{2(x_o-v\tau)^2}{a^2}-\frac{u^2}{4D(t-\tau)}}}{\sqrt{a^2+8D(t-\tau)}}$$
$$\times\left[1-\frac{\sqrt{4\pi D(t-\tau)}}{KR_{th}}\exp\left(\frac{\sqrt{4\pi D(t-\tau)}}{KR_{th}}-\frac{u}{\sqrt{4\pi D(t-\tau)}}\right)^2\right]\mathrm{erfc}\left(\frac{\sqrt{4D(t-\tau)}}{KR_{th}}+\frac{u}{\sqrt{4D(t-\tau)}}\right). \quad (36)$$

2.2.2 Optimal conditions for defect detection

To analyze the influence of the distance between the laser spot and the crack, an experiment with four different laser position has been carried out to see in which case we observe a wider temperature discontinuity that increases with the crack width [15].

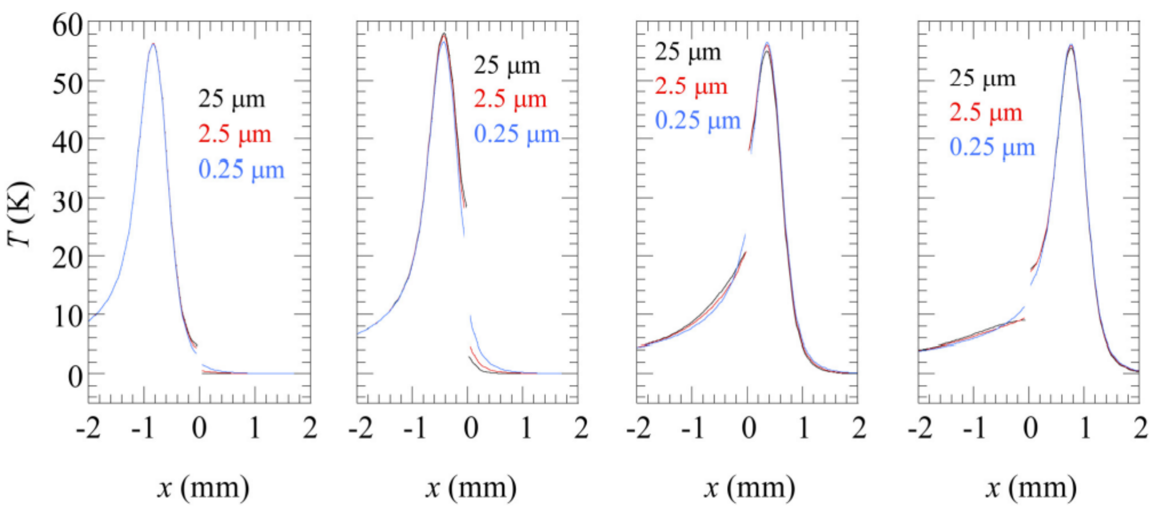

Figure 2.37 : Detecting defects at four different distances (-0.8, -0.4, 0.4, 0.8) from the center of the laser beam

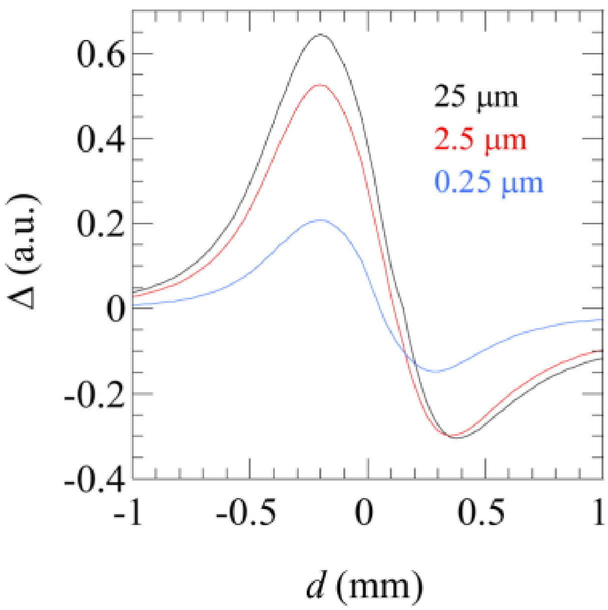

Figure 2.38 : Optimal distances to maximize the temperature gap caused by the defect

In this particular case with a velocity v = 10 mm/s and a laser radius a = 0.4 mm, the minimum difference is produced when the distance $d \approx a$, whereas the maximum appears for $d \approx a/2$.

Once we understand how to set the various parameters, it is possible to analyze the experimental thermograms recorded by the IR camera. First of all, in the next figure, we can see a thermogram without defects both for the static and for the moving laser. Then we will observe how the presence of a crack can influence the results.

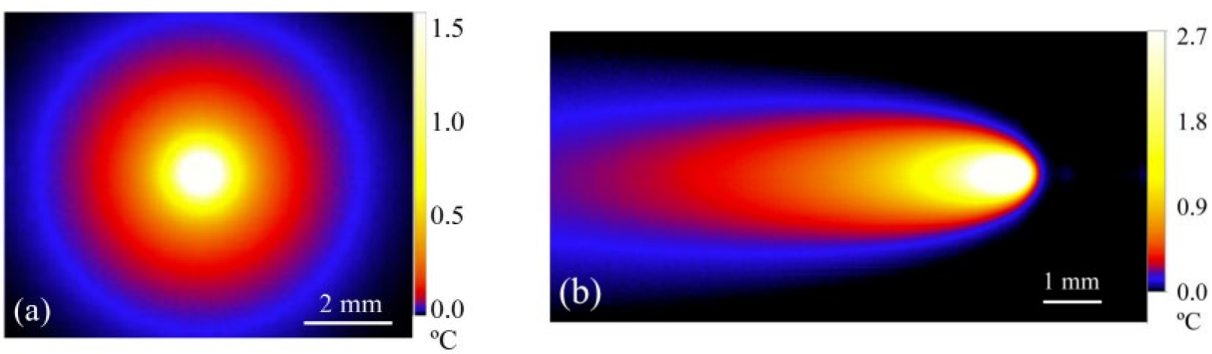

Figure 2.39 : Thermogram of a static (a) and a moving (b) laser without defects

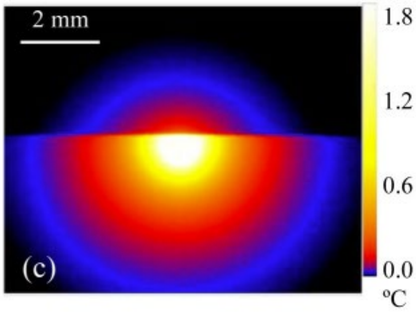

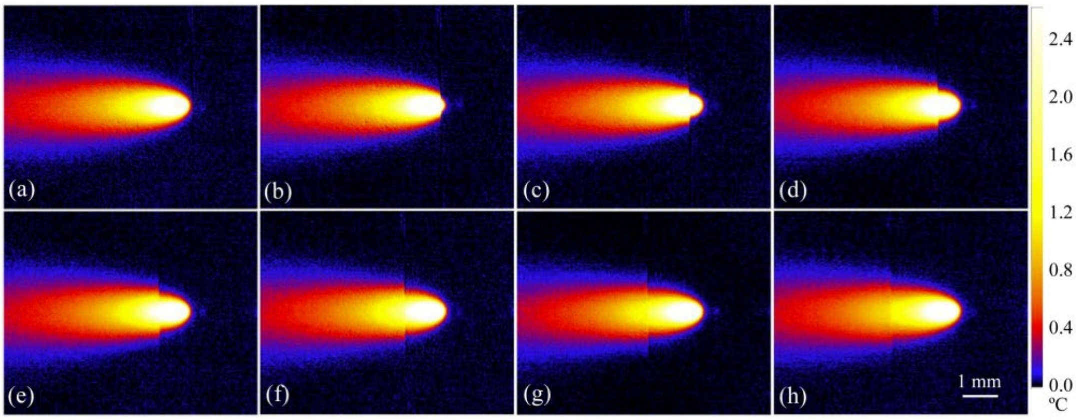

Figure 2.40 : Thermogram of static and moving laser with defects

In the last figure the sample is moving at 4 cm/s and it is quite evident the position of the crack, identified by the vertical discontinuity of the temperature distribution.

However we have to say that this method is only valid for infinite vertical cracks when the laser is moving in the direction perpendicular to the crack and, unfortunately, no analytical solutions has been found for more realistic applications. Furthermore one of the main problems to find an accurate analytical description of the process is due to the effect of lens diffraction, which causes a softening of the theoretically abrupt temperature jump at the crack position [15], making the defect more difficult to identify.

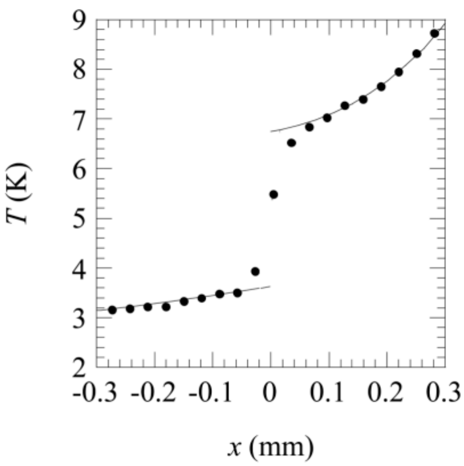

Figure 2.41 : Theorical and experimental temperature gap

2.2.3 Emissivity

One of the main issues in infrared thermographic measuring procedure is the emissivity evaluation. An infrared thermal camera, in fact, is only able to detect the radiation emitted by a body (which involves emitted, reflected and transmitted radiation) and, to convert this energy into temperature, we need to know the specific value of the emissivity. This expression describes the capacity of a body to emit in comparison with an ideal black body: values of emissivity can oscillate between 0 (perfect reflector) and 1 (perfect emitter). An important role is also played by wavelengths, which can influence material properties regarding energy absorption or transmission. In the work [16] Avdelidis and Moropoulou developed an empirical procedure to calculate emissivity. The samples were placed in an oven for 24h at three different temperatures (0, 48.8, 100 ^{o}C), attaching as a reference emitter a piece of electrical tape with a known emissivity of 0.95. The results showed an higher emittance at higher temperatures in short wavelength range (3-5.4 µm) whereas the emissivities are higher at lower temperatures in the long wavelength range (8-12 µm). In conclusion we can say that correction of emissivity, considering material properties, temperature and wavelength, is fundamental to build an accurate thermographic analysis.

2.2.4 Exposure times and emissivity optimization

At this point we can deeply analyze how other parameters of active thermography can be tuned to clearly highlight the presence of defects. As a reference to analyze shape and size of internal pores, in the work [17] they used the technique of X-ray Micro Computed Tomography (µCT). This method, however, is time consuming and quite expensive. For these reasons the results obtained with active thermography will then be compared with the optimal solution of the µCT.

First of all, to facilitate the detection of inner defects, the material is usually coated with a thin layer of graphite, which increases the portion of energy absorbed (the emissivity increases).

Figure 2.42 : Workpiece with and without the covering layer of graphite

In this experiment the µCT revealed the presence of different defects with various complex shapes and dimensions. These results will then be simulated in the FEM model.

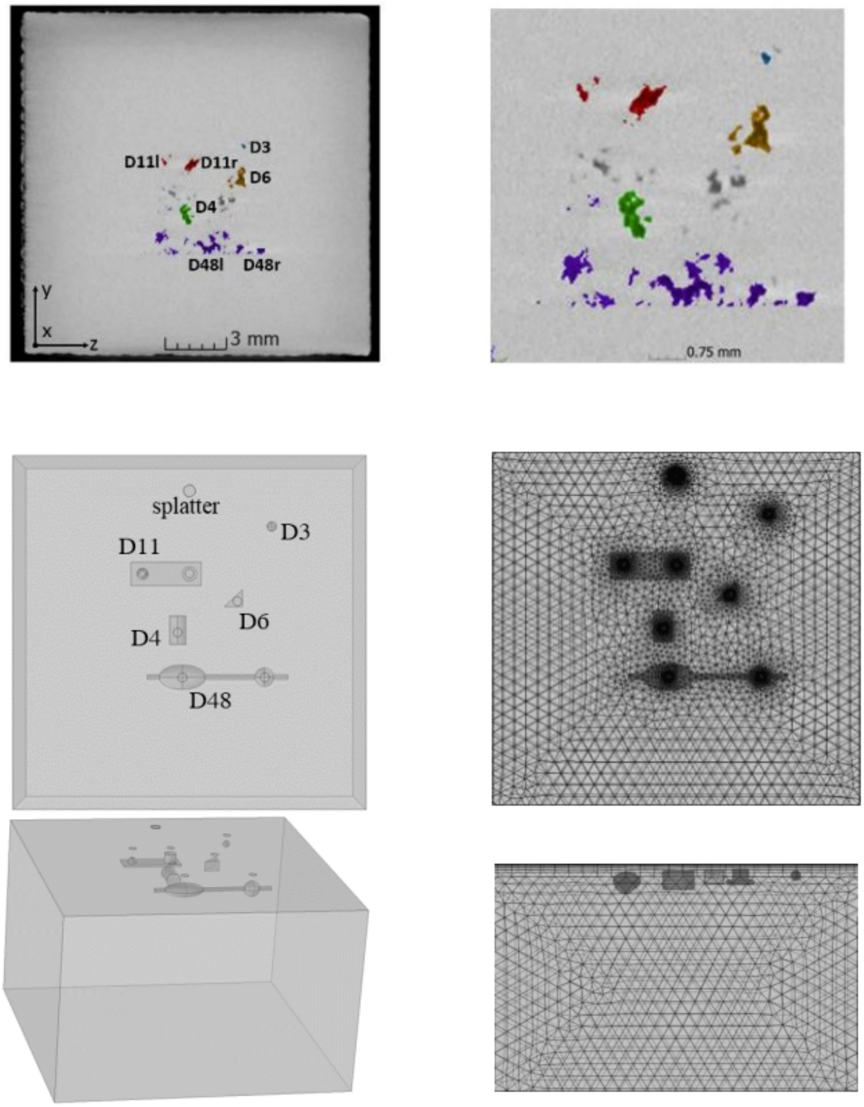

Figure 2.43 : FEM model to reproduce the presence of different defects (on the top)

The importance of the coating is then investigated. In the next figure, indeed, we can easily observe how a too low emissivity or an inhomogeneous emissivity distribution can negatively affect the results.

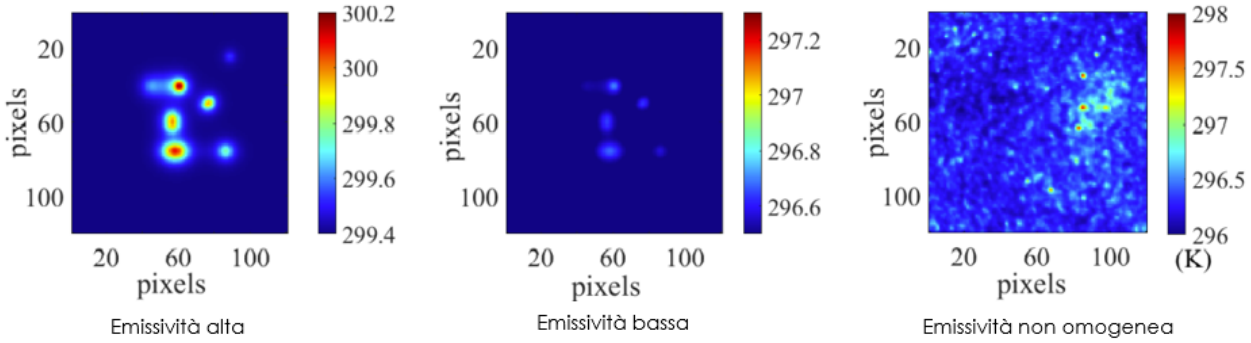

Figure 2.44 : Thermogram results with high emissivity, low emissivity and non-homogeneous emissivity

For the same reasons, the time after the heating pulse in which the recording take place strongly affects the possibility to highlight the defects. This evaluation was made both for the uncoated and for the coated sample. It is easy to observe how a too long exposure generates a background noise that makes it impossible to detect irregularities. Using post data processing, however, it is still possible to detect some defects.

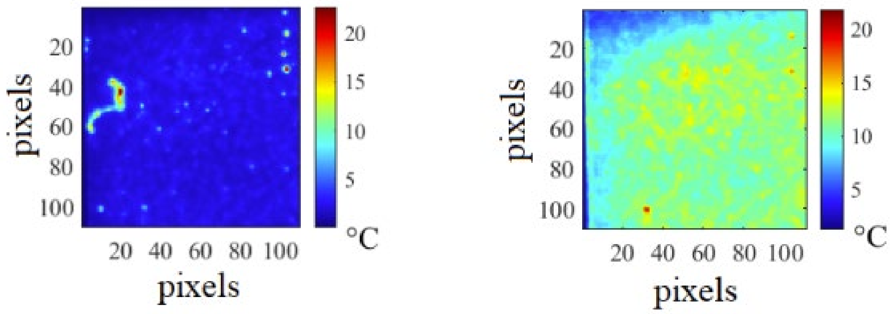

Figure 2.45 : Thermogram results with too short exposing time (30 ms) and too long exposing time (100 ms)

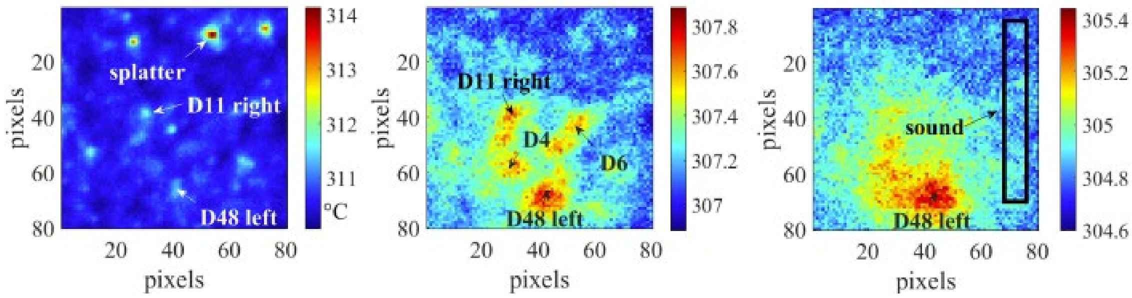

Figure 2.46 : Thermogram results with three different exposing times (0 ms, 20 ms and 100 ms) using post data processing

2.3 Welding methods

In this chapter we will briefly summarize the main characteristics of the two welding methods used and the variation in results based on changing certain parameters.

2.3.1 SMAW

Shielded metal arc welding is a manual arc welding process that uses a consumable electrode. Thanks to an alternating or direct current coming from a power supply, an electric arc is generated between the electrode and the workpieces to be joined. Then both the base metal and the electrode form a weld pool that after cooling becomes a joint. In the meantime, the flux coating that covers the electrode disintegrates, releasing vapors that serve as a shielding gas to protect the welded area from contamination. The slag that forms around the weld bead needs to be removed due to the corrosive properties which could lower the weld quality. However, in SMAW the electrode is not continuously fed hence it needs to be changed after a specific time. This leads to wastage of time and electrode as the electrode cannot be used after it is consumed up to a certain length [18].

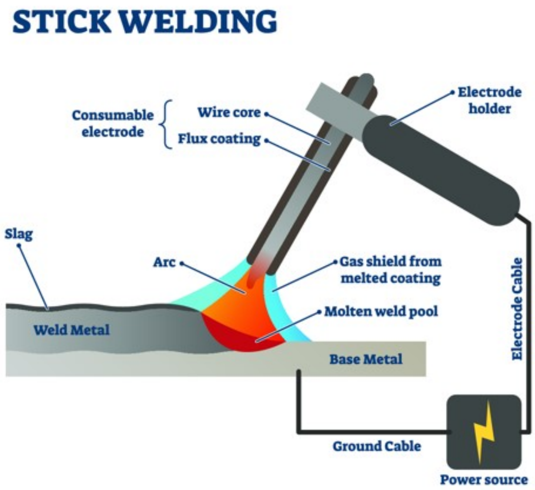

Figure 2.47 : SMAW materials and method

2.3.2 GMAW

Gas metal arc welding is a continuous wire process in which the protection of the weld pool is provided by a covering gas, which flows from the torch. GMAW welding process has several disadvantages, the most important being sensitivity to wind and contaminants. In this case we can observe a faster cooling of weld zone because no slag is present at the top of the weld. The presence of slag in the SMAW process, in fact, allows slower cooling of weld zone, giving to residual stresses the possibility to release the tension during this period [18].

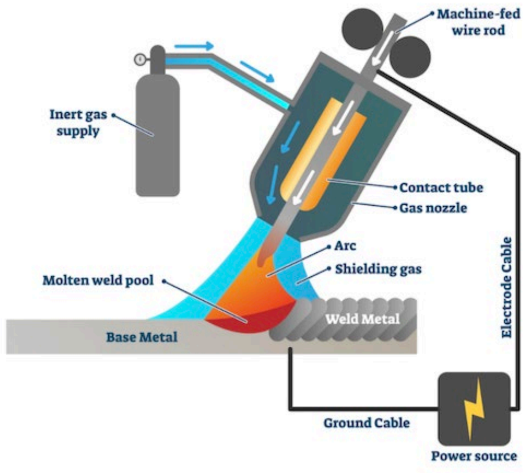

Figure 2.48 : GMAW materials and method

2.3.3 Effects of changing welding parameters

In general, for both methods, we can summarize the weld bead behavior depending on how voltage and current change

- Too low voltage : decrease in width, incomplete groove filling
- Too high voltage : too wide weld bead
- Too low current : decrease in heat generated and deposition rate, incomplete groove filling
- Too high current : excessive heat generation
- Too high wire feed rate : increase of current and heat input, increase of HAZ

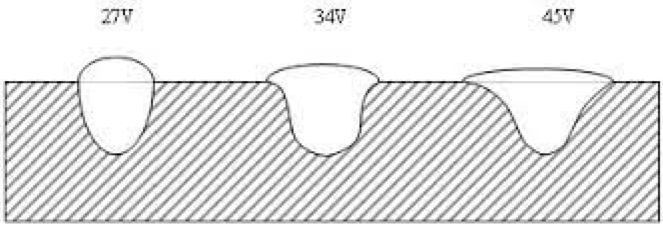

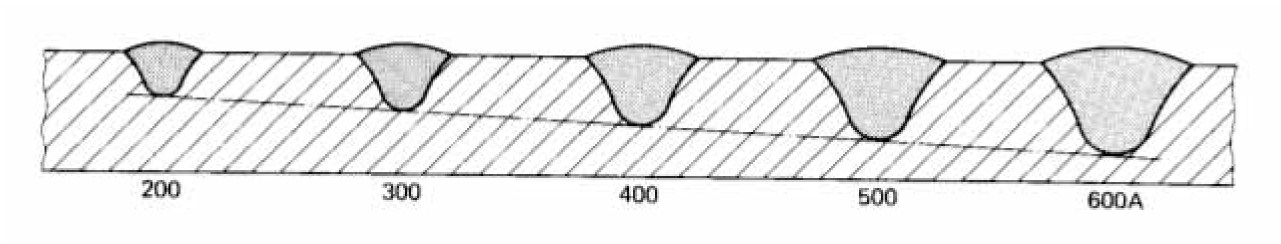

Figure 2.49 : Effects of voltage and current

Other factors that can influence the penetration profile are :

- Stick orientation
- Polarity
- Shielding gas
- Welding speed

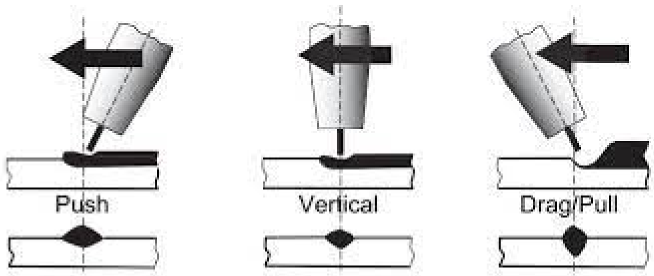

Figure 2.50 : Effects of stick orientation

CURRENT TYPE	DCEN	DCEP	AC (BALANCED)
ELECTRODE POLARITY	NEGATIVE	POSITIVE	
ELECTRON AND ION FLOW PENETRATION CHARACTERISTICS	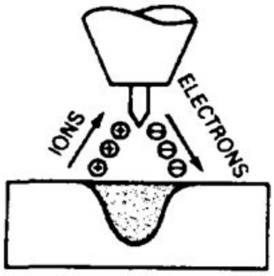	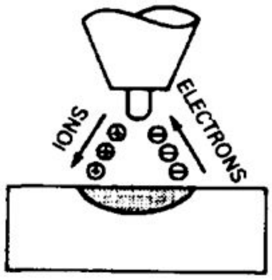	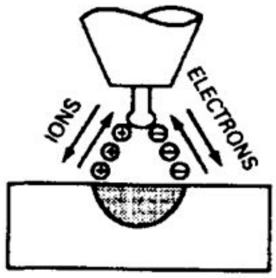
OXIDE CLEANING ACTION	NO	YES	YES-ONCE EVERY HALF CYCLE
HEAT BALANCE IN THE ARC (APPROX.)	70% AT WORK END 30% AT ELECTRODE END	30% AT WORK END 70% AT ELECTRODE END	50% AT WORK END 50% AT ELECTRODE END
PENETRATION	DEEP; NARROW	SHALLOW: WIDE	MEDIUM
ELECTRODE CAPACITY	EXCELLENT e.g., 1/8 in. (3.2 mm) 400 A	POOR e.g., 1/4 in. (6.4 mm) 120 A	GOOD e.g., 1/8 in. (3.2 mm) 225 A

With Direct current straight polarity welding (DCEP) the plates are positive and the electrode is negative. It is generally considered that two-thirds of the arc heat is generated at the electrode while only one-third of the heat is generated at the base plate. This method leads to a fast electrode melting and a high deposition rate but, on the other hand, it could cause lack of penetration. With Direct current reverse polarity there is a total inversion of the proportions of heat input distribution and, as a result, a deeper penetration with more heat generated at the base plate.

The primary function of the shielding gas is to protect the weld pool from the atmosphere and to provide a medium which can allow the flow of electricity from an electrode to a workpiece. This phenomenon is strongly related to the thermal conductivity of the gas. Gases with low thermal conductivity, such as Argon, tend to have a deep and narrow profile while, on the other hand, gases like Helium with a high thermal conductivity, show a wide evenly distributed area with low penetration [25].

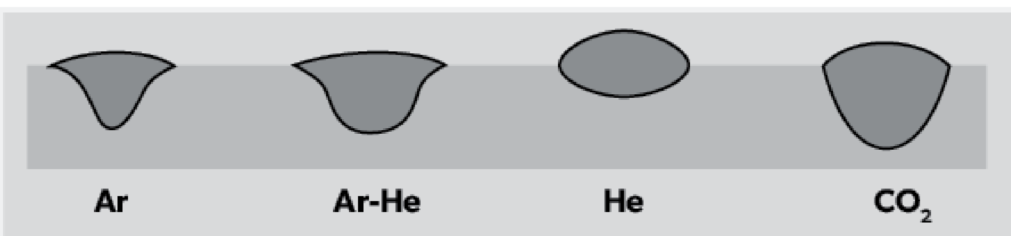

Figure 2.51 : Effects of shielding gas

3 MATERIALS AND METHODS

3.1 Materials

In order to have sufficient data to analyze, we decided to carry out four welding samples:

1. 5 mm SMAW Butt Joint
2. 5 mm GMAW Butt Joint
3. 3 mm GMAW Tee Joint
4. 3 mm SMAW Tee Joint

The material used for all tests is S275JR steel, whose characteristics are given below.

Qualità materiale	**S275JR**	Acciaio Strutturale	*Scheda Dati*
Norma di riferimento	**EN 10025-2: 2004**		***Lucefin Group***
Numero	**1.0044**		*rev. 2018*

Composizione chimica

C% max	**Si%**	**Mn%** max	**P%** max	**S%** max	**N%** max	**Cu%** max	
0,21 c)	-	1,50	0,035	0,035	0,012 a)	0,40	Analisi di **colata**
0,24 c)	-	1,60	0,045	0,035	0,014 b)	0,45	Analisi di **prodotto**

Metodo di disossidazione FN acciaio effervescente non ammesso

c) per spessori > 40 mm fino a 100 mm max 0.22 in colata / 0.25 sul prodotto

c) per spessori > 100 mm il contenuto di C va concordato

a) il valore max di N non si applica se la composizione chimica mostra un contenuto di Al (totale) ≥ 0.020%

b) il valore max di N non si applica se la composizione chimica mostra un contenuto di Al (totale) ≥ 0.015%

Temperature in °C

Deformazione a caldo	**Normale stato di fornitura +U**	**Ricottura di lavorabilità +A**	**Ricottura isotermica +I**	**Le temperature valgono per analisi che si approssima a:** C%	Mn%	Si%
1150-850	Stato naturale	650-700 aria	-	0.19	0.65	

In alcuni casi i particolari sono sottoposti anche a normalizzazione e rinvenimento **+NT** oppure tempra e rinvenimento **+QT**

Normalizzazione Rinvenimento	**Tempra Rinvenimento**	**Distensione +SR**	**Preriscaldo per saldatura**	**Distensione dopo saldatura**
880-900 aria 550-660 aria	860-900 acqua 550-660 aria	50 sotto la temp. di rinv.	non richiesto	raffreddamento lento

Ac1	**Ac3**	**Ms**	**Mf**
-	-	-	-

Proprietà meccaniche

Laminati a caldo EN 10025-2: 2004 **S275JR** 1.0044

Prova di trazione e resilienza in longitudinale a + 20 °C

sezione mm oltre	fino a	**R** N/mm²	**ReH** N/mm² min	**A%L** min (L)	**A%** min (T)	**Kv** +20 °C J min d) (L)	***HB*** *per inf.*	**Modulo Elastico** GPa +20 °C long.	tang.
	3	430-580	275	-	-	-	-		
3	16	410-560	275	23	21	27	*122-162*	200	77
16	40	410-560	265	23	21	27	*122-162*		
40	63	410-560	255	22	20	27	*122-162*		
63	80	410-560	245	21	19	27	*122-162*		
80	100	410-560	235	21	19	27	*122-162*		
100	150	400-540	225	19	19	27	*119-158*		
150	200	380-540	215	18	18	27	*110-158*		
200	250	380-540	205	18	18	27	*110-158*		
250	400 c)	380-540	195	18	18	27	*110-158*		

d) Per spessori > 100 mm i valori devono essere concordati. I valori di resilienza vanno verificati solo se specificati in fase di ordine. (la normalizzazione **+N è consigliata)**

c) Valori applicabili ai prodotti piani

Figure 3.1 : S275JR steel characteristics

Before proceeding with welding, we checked in which zone of the Graville Diagram our material is located, according to carbon content and carbon equivalent.

$$CE = C + Mn/6 + (Cr + Mo + V)/6 + (Ni + Cu)/15 = 0.21 + 1.5/6 + 0.4/15 = 0.49$$

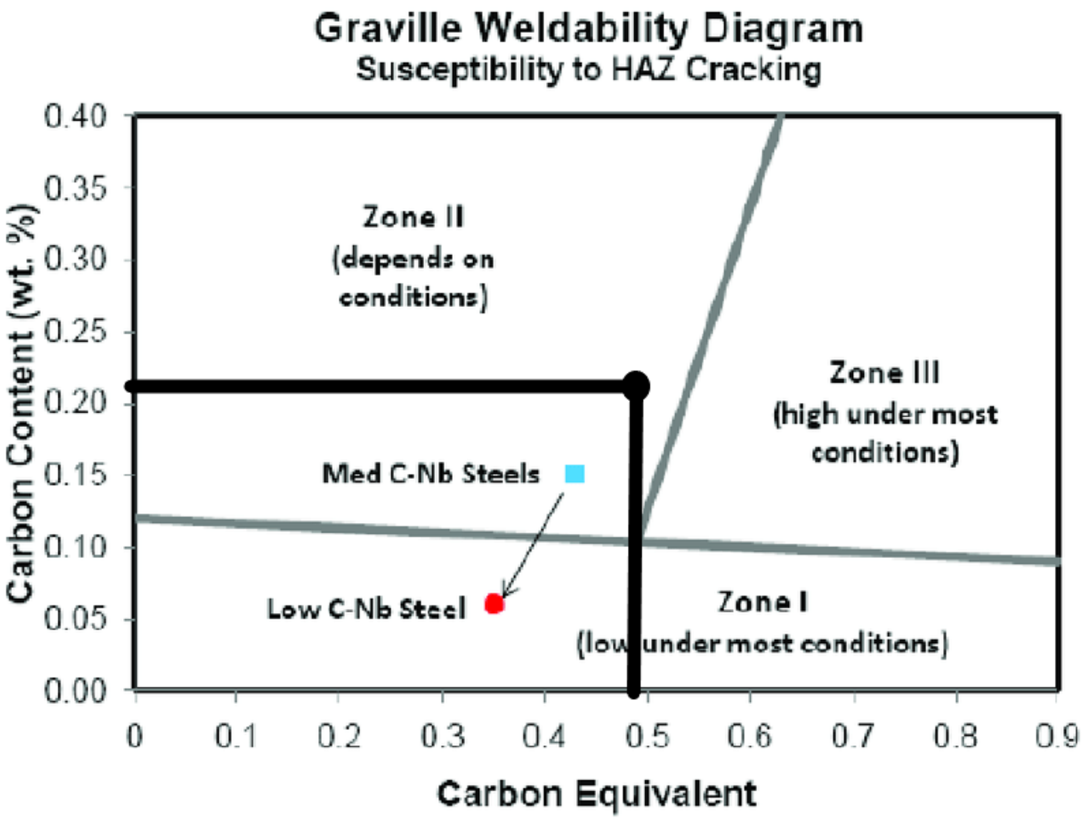

Figure 3.2 : Graville Weldability Diagram

Fortunately the point falls in Zone II and this allows us to avoid a series of treatments that we would have been forced to do if the point had been in Zone III such as preheating and post weld heat treatment (PWHT) [19].

The welding machines used are:

- TECNOWELD MIG 110, 35-100 A, 0.6-0.8 mm (2 kW absorbed at 60%)
- AWELCO ARC 250 coupled with Oerlikon TENAX 35S basic coated low hydrogen electrodes

Analysis of all-weld metal (Typical values in %)

C	Mn	Si	P	S	Cr	Ni	Mo	Nb	V	N	Cu
0.075	1.35	0.35	≤ 0.020	≤ 0.015	-	-	-	-	-	-	-

All-weld metal Mechanical Properties

Heat Treatment	Yield Strength N/mm^2	Tensile Strength N/mm^2	Elongation A5 (%)	Impact Energy ISO - V (J) -50°C	Hardness
PWHT 620°C x 1h	≥ 400	490 - 560	≥ 22	≥ 100	-
As Welded	≥ 420	510 - 640	≥ 22	≥ 100	-

Materials

S(P)235-S(P)420, GP240-GP280

SA 516 gr.60; SA 516 gr.70; SA 106 gr.B

Storage and redrying

Keep dry and avoid condensation.
HD ≤ 5: Re-dry at 400-420 °C for 1 hour, 3 times max.
HD ≤ 10: Re-dry at 350-370 °C for 1 hour, 3 times max

Current condition and welding position

DC+; AC

PA PB PC PF PE PF2

Packaging data

Diameter (mm)	Length (mm)	Current (A)	Electrode average weight (g)	Weld metal weight per electrode (g)
2,0	300	25-50	13,0	7,8
2,5	300	70-100	20,1	12,1
2,5	350	70-100	23,5	14,1
3,2	450	90-130	49,5	29,8
4,0	450	110-170	70,9	42,6
5,0	450	170-220	106,5	63,9
6,0	450	210-280	150,3	90,1

Figure 3.3 : From left to right: GMAW and SMAW welding machines, basic coated electrodes and their related properties

To detect temperature variations we used a FLIR A40 Infrared Thermal Imaging Camera. This is a long wave camera, which is able to operate in three different ranges:

- From -40 to 120 °C
- From 0 to 500 °C
- From 350 to 1500 °C

In our experiments we will use the highest temperature range.

Figure 3.4 : FLIR A40 thermal imaging camera with its own characteristics

Imaging Performance	
Field of view/min focus distance	24° x 18° / 0.3 m
Spatial resolution (IFOV)	1.3 mrad
Thermal sensitivity @ 50/60Hz	0.08° C at 30° C
Focusing	Built-in focus motor
Detector type	Focal Plane Array (FPA), uncooled microbolometer
Spectral range	7.5 to 13 µm
Image Presentation	
FireWire output	IEEE-1394 8/16-bit monochrome and 8-bit color
Video output	RS170 EIA/NTSC or CCIR/PAL composite video
Measurement	
Temperature ranges	Range 1: -40°C to +120°C (-40 to +248°F) Range 2: 0°C to +500°C (+32 to +932°F) Optional: Up to +1500°C (+2732°F) Optional: Up to +2000°C (+3632°F)
Accuracy (% of reading)	± 2°C or ± 2%
Measurement modes	Spot, Area, Isotherm, Difference
Automatic emissivity correction	Variable from 0.1 to 1.0
Individual emissivity settings	Individually settable
Measurement corrections	Reflected ambient, distance, relative humidity, external optics. Automatic, based on user input
Supplementary Lenses*	
Field of view/min. focus distance	7° Telescope (7° x 5.3°/4m) 12° Telescope (12° x 9°/1.2m) 45°Wide angle (45° x 34°/0.1m) 80° Wide angle (80° x 60°/ 0.1m) Close up: 64/150 mm (FOV=64 x 48 mm at 150 mm); 34/80 mm (FOV=34 x 25 mm at 80 mm) Macro: 50 micron (14.3 to 18.7 mm focus; FOV=14.3 x 10.8 mm at 14.3 mm; FOV=15.1 x 11.2 mm at 18.7 mm; IFOV=45 µm at 14.3 mm; 47 µm at 18.7 mm)
Lens recognition	Automatic lens recognition and measurement corrections

Power Source	
AC operation	AC adapter 110/220 VAC, 50/60Hz (included)
DC operation	8-30V nominal, <6W
Environmental	
Operating temperature range	-15°C to +50°C (5°F to 122°F)
Storage temperature range	-40°C to +70°C (-40°F to 158°F)
Humidity	Operating and storage 10% to 95%, non-condensing
Encapsulation	IP 40 (Determined by connector type)
Shock	Operational: 25G, IEC 68-2-29
Vibration	Operational: 2G, IEC 68-2-6
Physical Characteristics	
Weight	1.4 kg (3.0 lbs)
Size	207mm x 92mm x 109mm (8.1" x 3.6" x 4.3")
Tripod mounting	1/4" – 20

User Configuration Table		
TYPE	**FUNCTION**	**REMARK**
Digital Input	TTL level • Shutter disable • Store image • Batch enable	Isolation and relay function in external module
Digital Output	TTL level • Spot/Area threshold ALARM • Internal temperature sensor ALARM • V-sync	Isolation and relay function in external module
Analog Output	• Spot/Area out: 0-5V • Internal temperature sensor out: 0-5V	Scaled to Tlow – Thigh Isolation in external module
Analog Input	• External temperature sensor in: 0-5V	Scaled to Tlow – Thigh Isolation in external module

Once the camera has been correctly positioned on a tripod, we can proceed with welding. All data collected were subsequently processed on FLIR ResearchIR software.

Figure 3.5 : Positioning the tripod and taking measurements

3.2 Welded plates

All welds were deliberately made by making mistakes, so that the presence of defects can be detected both visually or by thermographic analysis. Welds results are now presented front and back in the same order shown at the beginning of the chapter.

Figure 3.6 : 5 mm SMAW Butt Joint front and back

Figure 3.7 : 5 mm GMAW Butt Joint front and back

Figure 3.8 : 3 mm GMAW Tee Joint

Having tried both types of welding and having understood how to handle voltage and amperage correctly, these last two tee joining experiments were performed more regularly and less discontinuously than in previous tests, leading to a lower presence of defects. We can therefore use these results as a reference of correctly executed welding.

Figure 3.9 : 3 mm SMAW Tee Joint

In general, as it can be easily seen from an initial visual inspection, the breaks and subsequent restarts that separate the various sections play an important role in the formation of defects, especially in the first electrode welding. In the 5 mm SMAW Butt joint experiment, in particular, there is a considerable presence of suction pore defects.

3.3 ResearchIR tuning

However, not all defects are observable with a simple visual inspection but they require the use of a specific software to visualize anomalies in temperature distributions.

First of all with ResearchIR we need to select the distance of the measurement between the Thermal Camera and the welding (1 m in our experiment). Then we can proceed selecting the emissivity. Once these parameters have been adjusted, we can place cursors and lines (ROI) on the map.

The following figure shows the basic data the program displays.

Statistic [units]	Cursor 1
Mean [°C]	1234.0
Std. Dev. [°C]	103.4
Center [°C]	(183.0, 122.0) 1298.4
Maximum [°C]	(184, 122) 1363.0
Minimum [°C]	(182, 121) 1050.9
Number of Pixels	9
Single Pixel Area [cm²]	N/A
Area [cm²]	N/A
Length [cm]	N/A
u Emissivity	✓ 0.85
u Distance [m]	✓ 1

Figure 3.10 : Selecting emissivity and measuring distance

Once the emissivity is properly tuned we can proceed with the evaluation of temperature distributions along profile and section of the weld bead. In particular we will compare the results of the correctly executed welding with those which included defects.

3.4 Results

In the following figures we can observe a difference in the temperature distribution where the electrode detaches from the workpiece. The irregular shape is due to the fact that the melt pool, which has a high reflection and low emissivity, is still visible at the time of detachment.

Figure 3.11 : Temperature distribution immediately after the electrode detachment and after a few seconds

5 mm SMAW Butt Joint – Profile

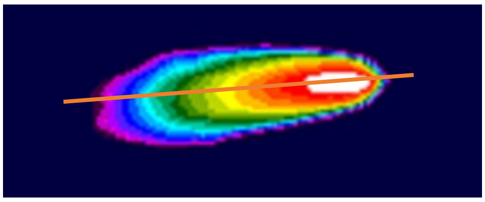

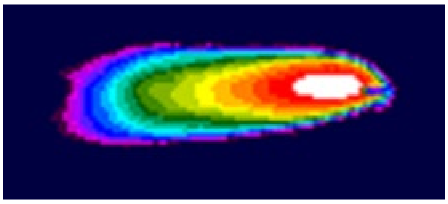

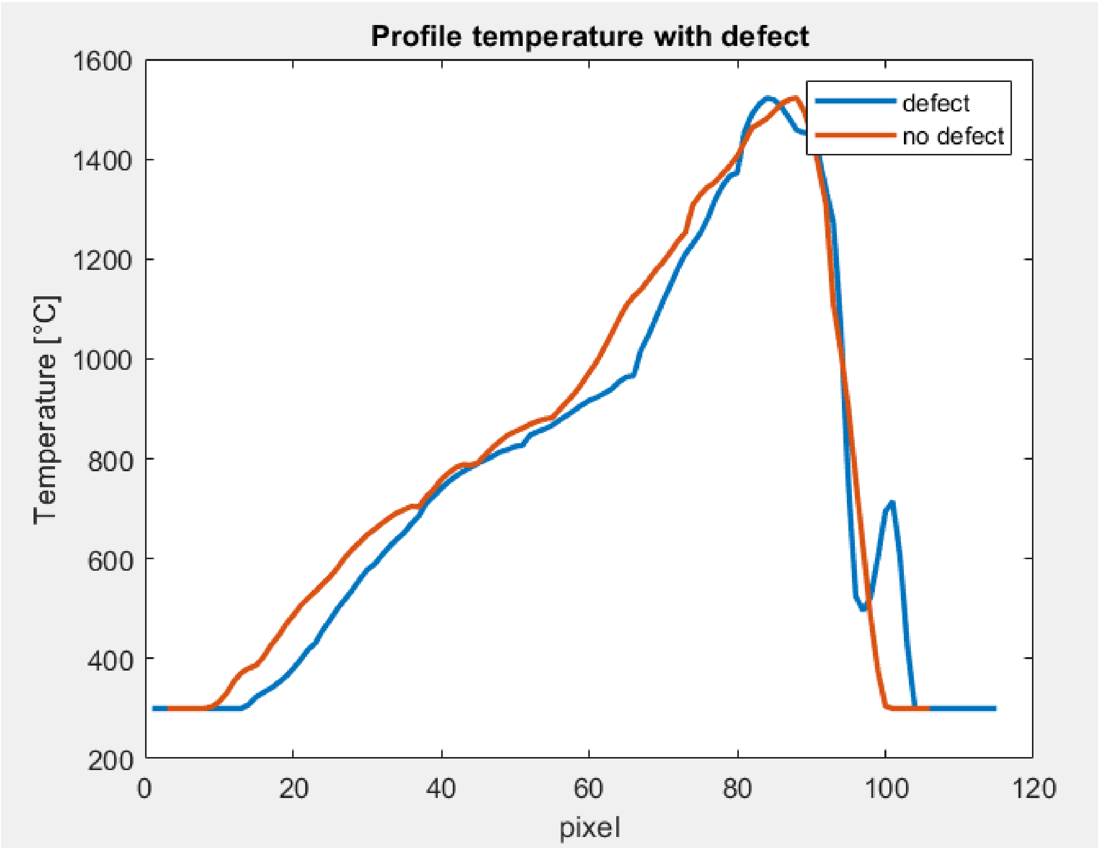

In this figure at top right we can observe the effect of a suction pore, probably due to excessive retention of the electrode in the same spot. This will cause a discontinuity both on the profile and section thermal distribution.

5 mm SMAW Butt Joint – Section

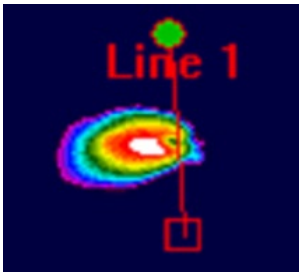

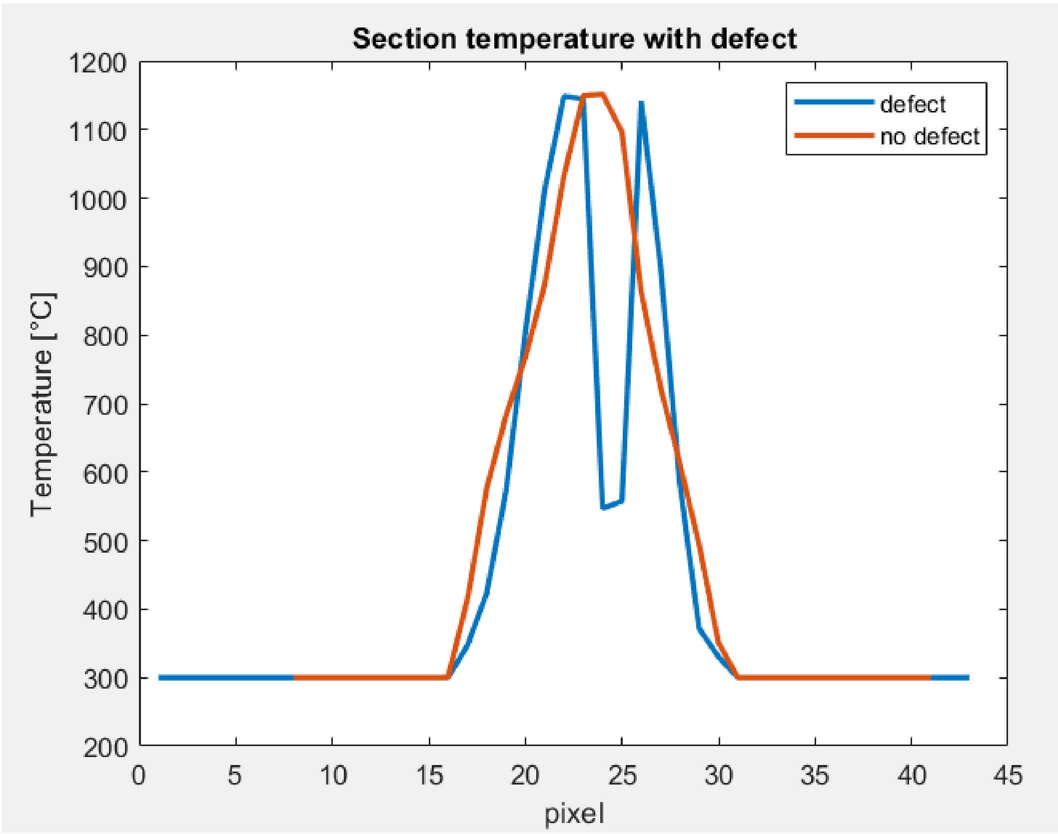

5 mm GMAW Butt Joint – Profile

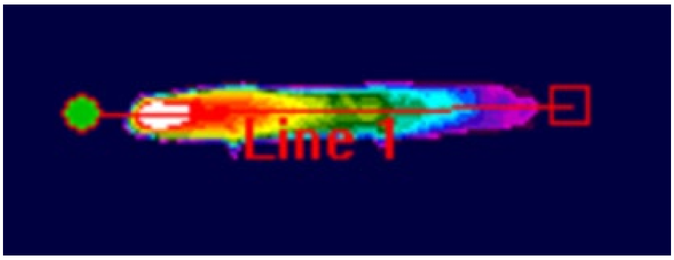

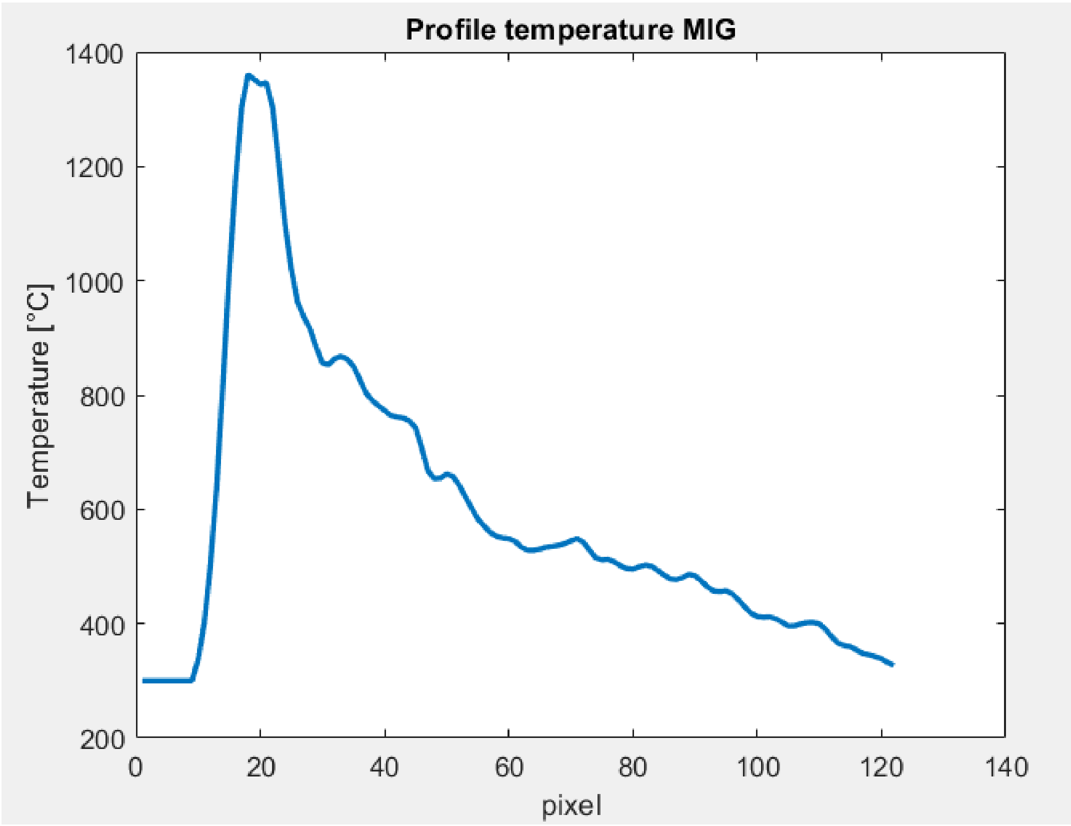

By adopting GMAW method, the temperature distribution shows a longer profile and a slightly narrower section. It also seems to have a little bit more irregular distribution, in particular around lower temperatures.

5 mm GMAW Butt Joint – Section

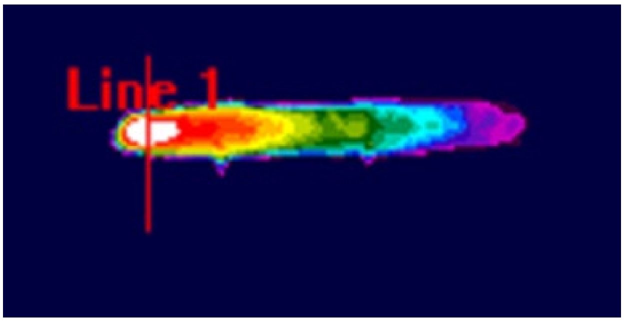

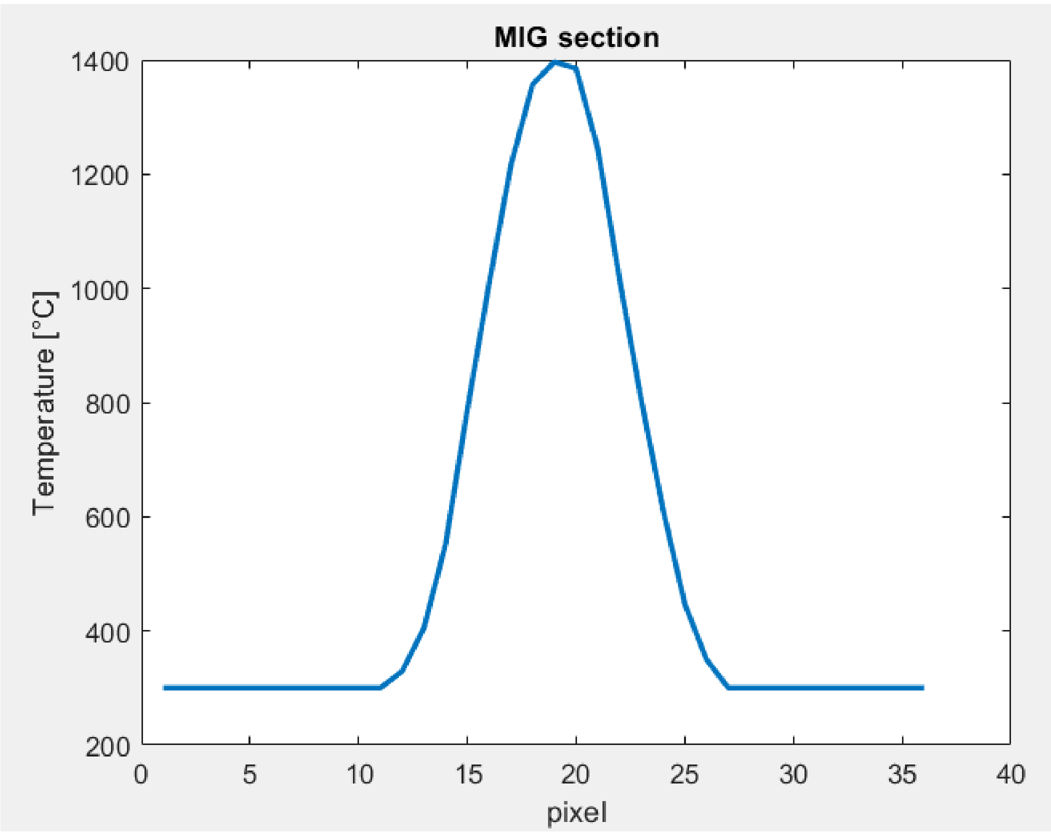

5 mm GMAW Butt Joint (2nd pass) – Profile

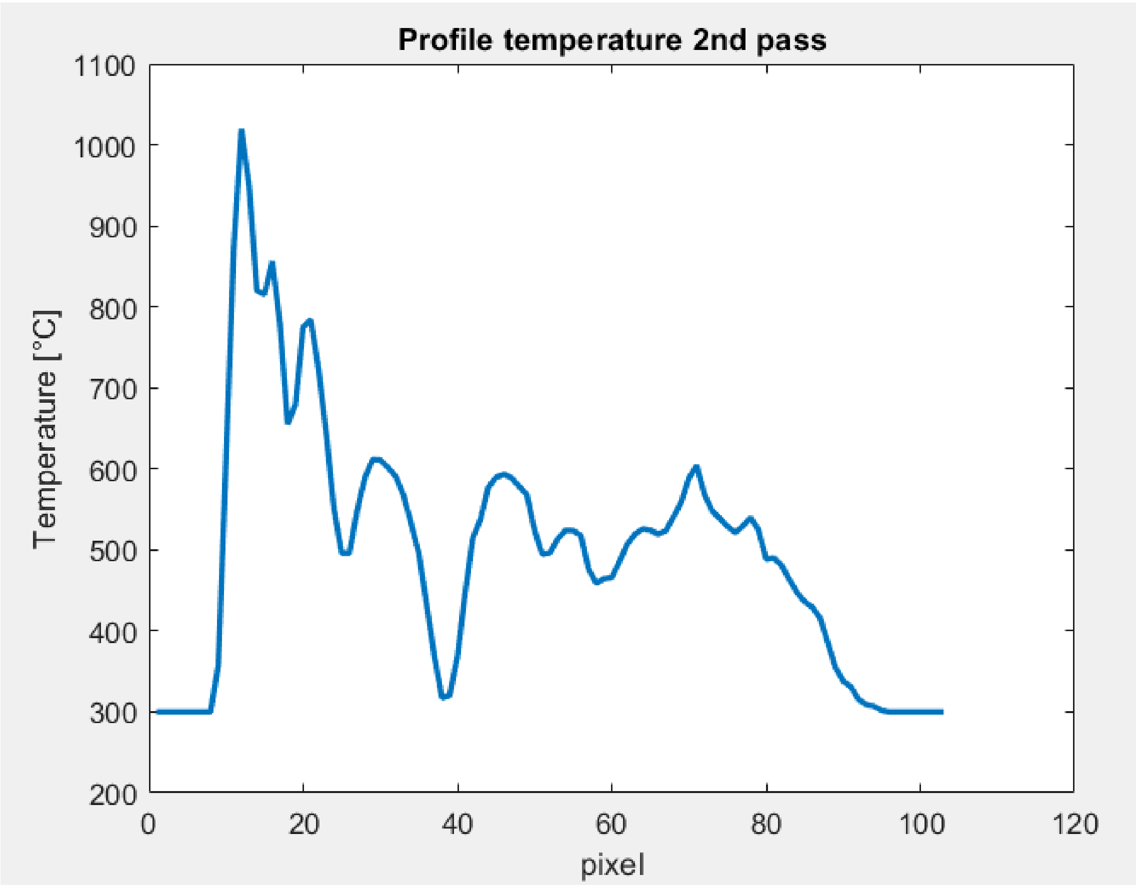

From this figure it is quite evident the bad result obtained with this second pass, realized above the first pass after cooling. The profile is extremely irregular and this will lead to hot cracking on the weld bead (we will analyze this defect in the next chapter).

3 mm GMAW Butt joint - Profile

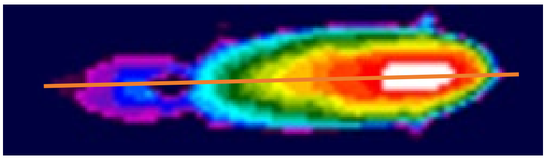

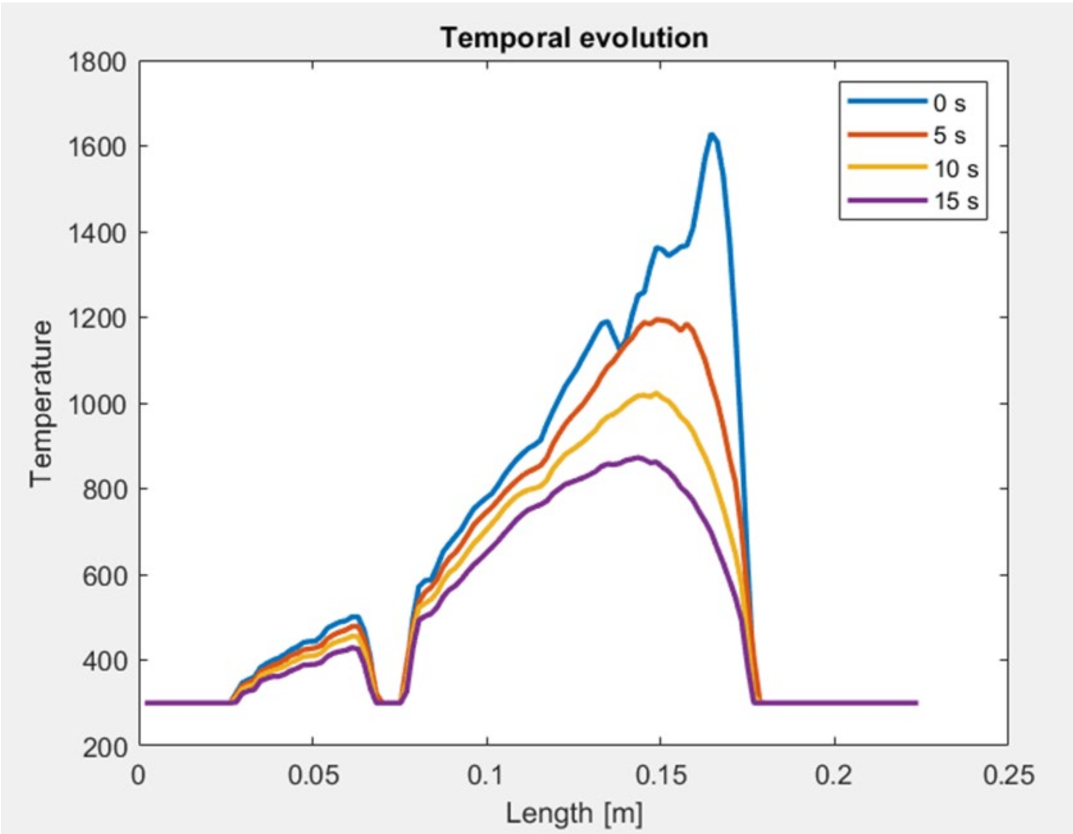

In this case, the evolution of the temperature distribution of the weld bead profile is analyzed at four different time steps: from 0 to 15 seconds after electrode detachment. This figure shows how the position of the defect doesn't change over time, thus allowing it to be easily identified. In addition it is possible to observe how after a few seconds, the irregularities at high temperatures of the blue curve, due to the oscillating movement of the welder disappear.

3 mm SMAW Tee Joint – Temporal Cursor

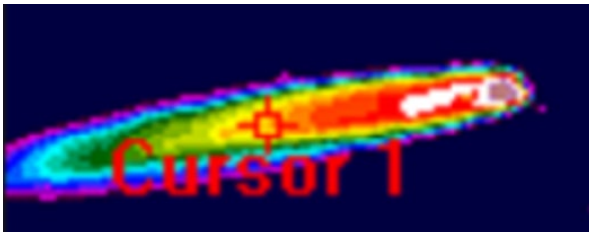

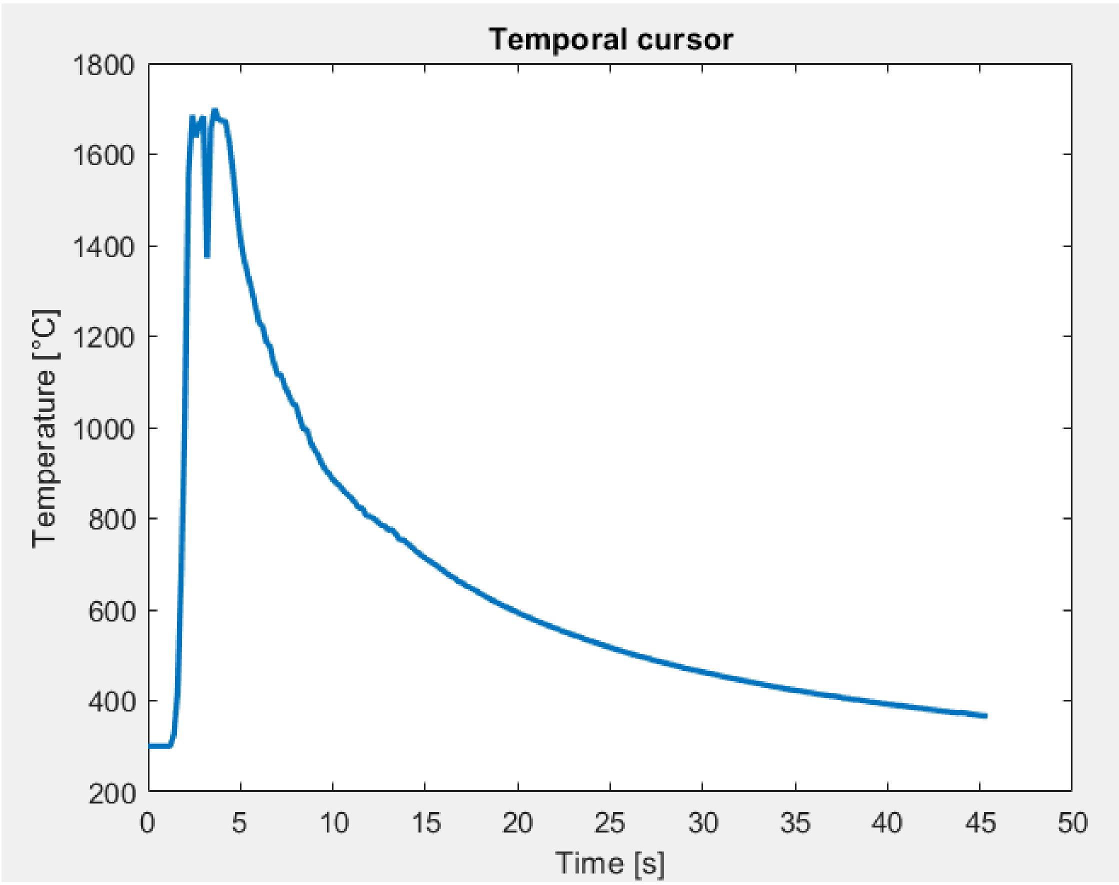

5 mm SMAW Butt Joint – Temporal Cursor

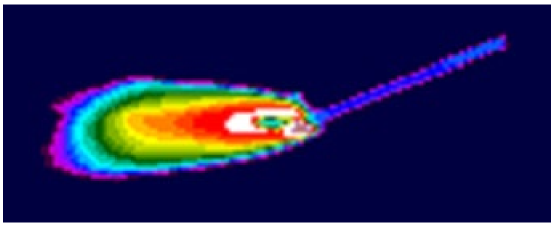

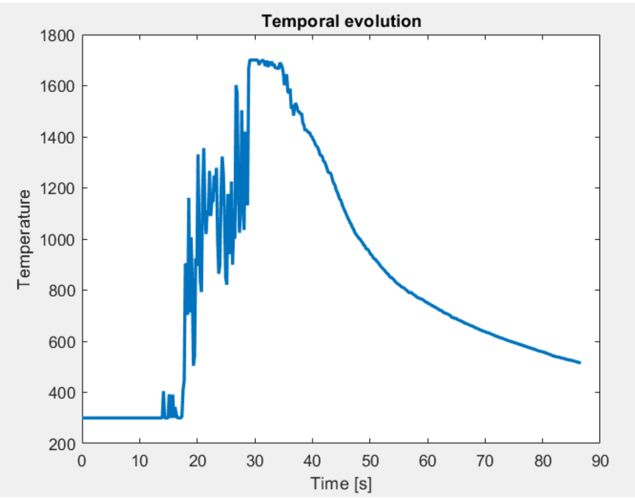

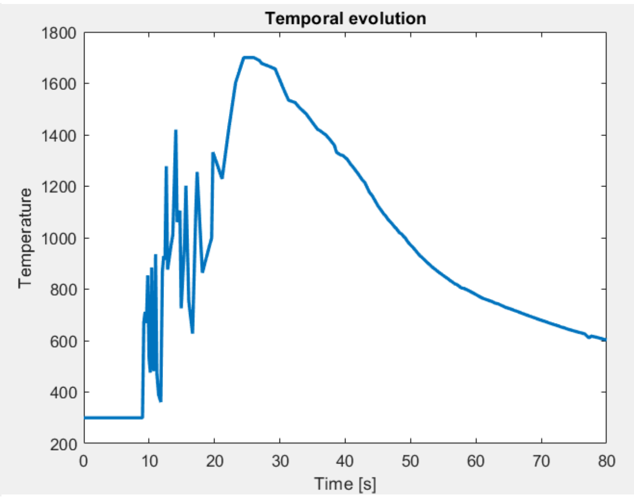

We have to remember that the temporal evolution graphs need to be read with particular attention because the thermal imaging camera it is made to work in an optimal range between 350 and 1500 °C. ResearchIR shows us temperatures up to 1700 °C but the results in this range could not be always accurate. In addition the heating transient seems to be very irregular: this phenomenon, however, it is due to the passage under the cursor of the electrode over the melting area which, being liquid, emits a little and reflects a lot, creating this background noise, in addition to having a temperature above that recommended by the thermal imaging camera. For all this reasons we will only consider valid the part related to the cooling transient below 1500 degrees.

3 mm GMAW Butt joint – Temporal Cursor

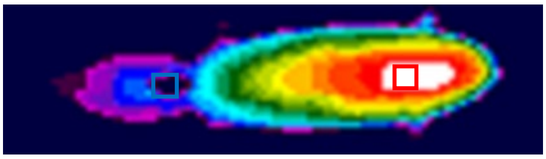

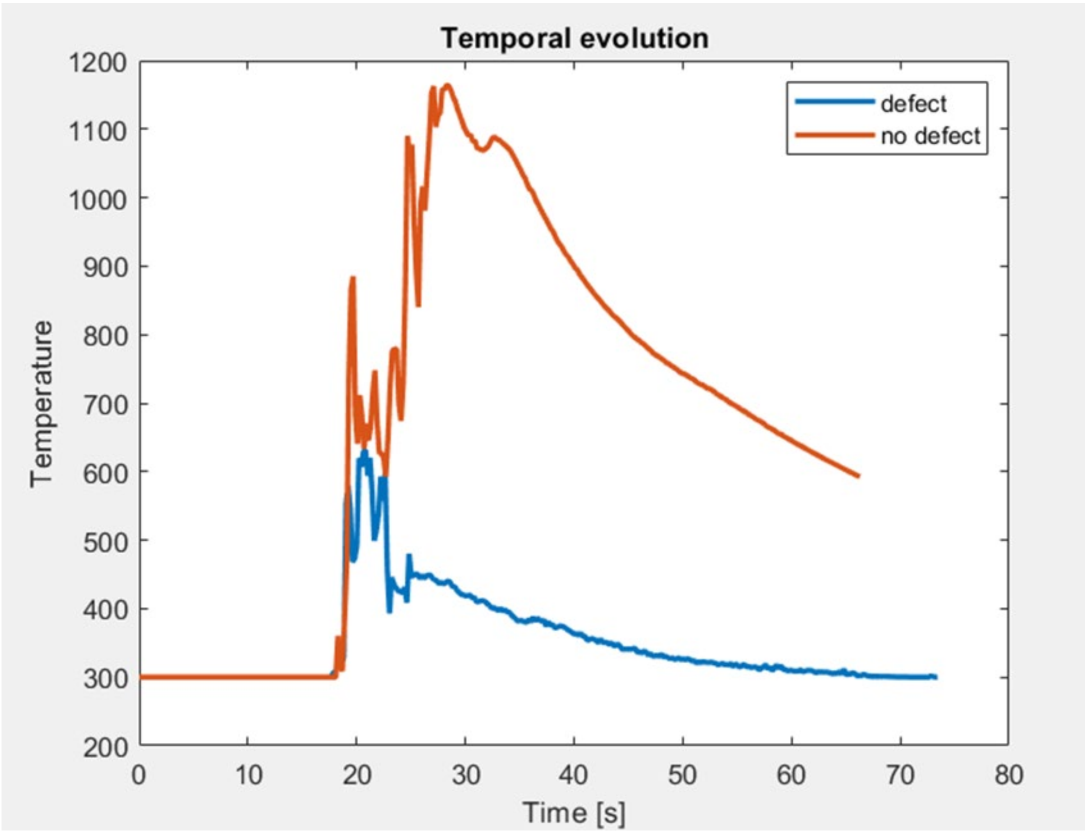

5 mm SMAW Butt Joint – Temporal Cursor

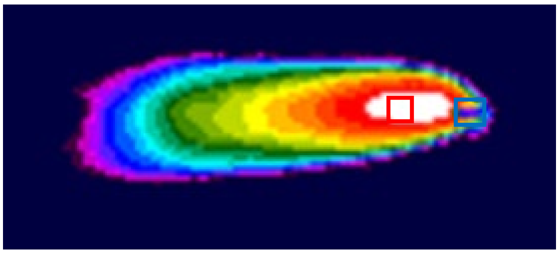

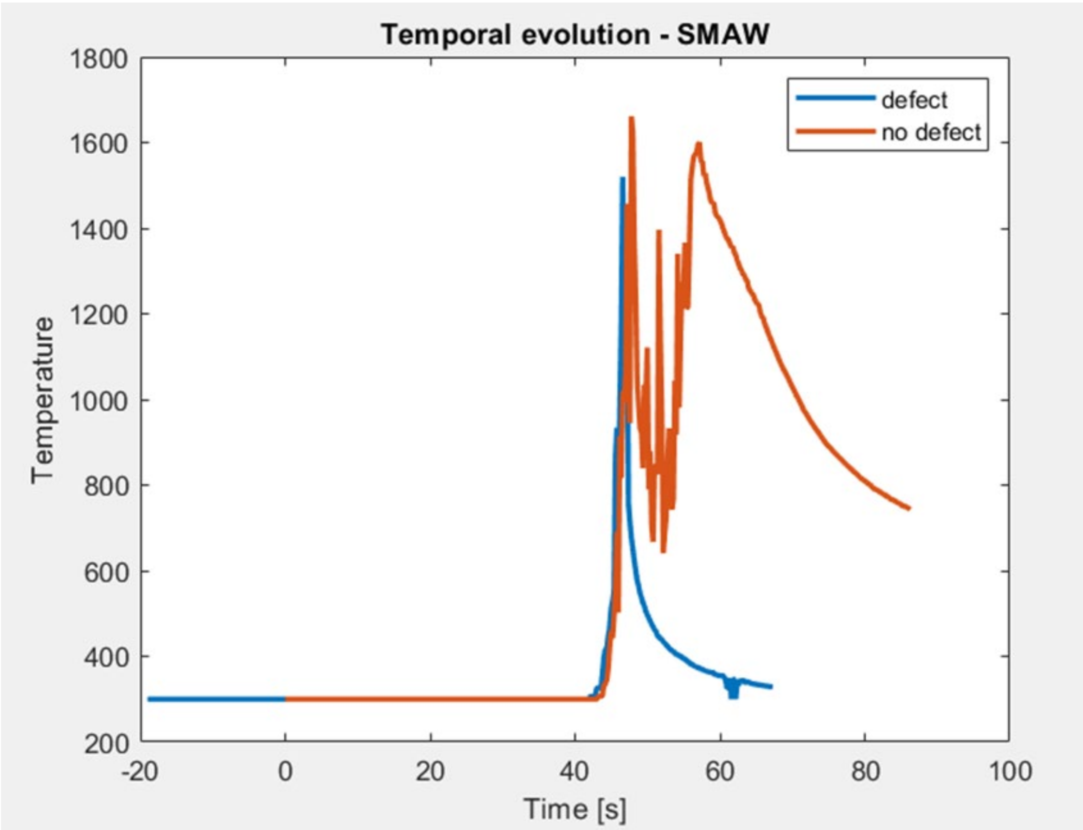

In the last two figures we can observe, with the presence of a defect, an abrupt temperature drop. This phenomenon is more visible using the SMAW method but, in both cases, it is very clear the huge temperature gap between the curves with and without defects.

4 SIMULATION

4.1 Laser thermal input simulation

To introduce the problem in a more simplified way, we will show by means of the software Matlab and his complementary PDE Toolbox, the behavior of a staircase in response to a thermal input that simulates the effect of the laser.

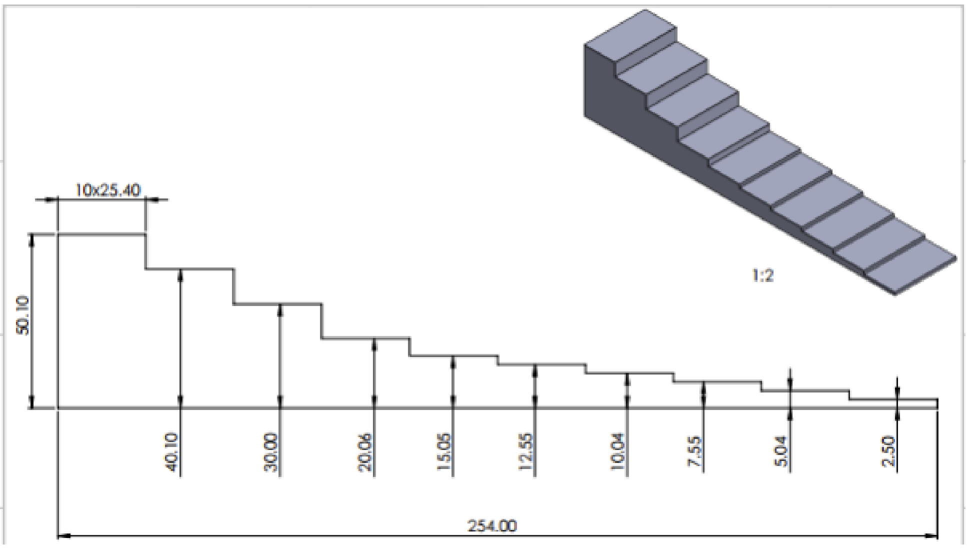

Figure 4.1 : Staircase geometry

The staircase is made of steel which has the following properties:

- Thermal conductivity 60.5 $\frac{W}{m*K}$
- Mass density 8000 kg/m^3
- Specific Heat 434 $\frac{J}{kg*K}$

Boundaries conditions:

- Convection coefficient 5 $\frac{W}{m^2*K}$
- Ambient temperature 26 °C

Let's start by importing into matlab the geometry from a stl file of the staircase.

```
model = createpde('thermal','transient');

gm=importGeometry(model,'SYS.stl');
```

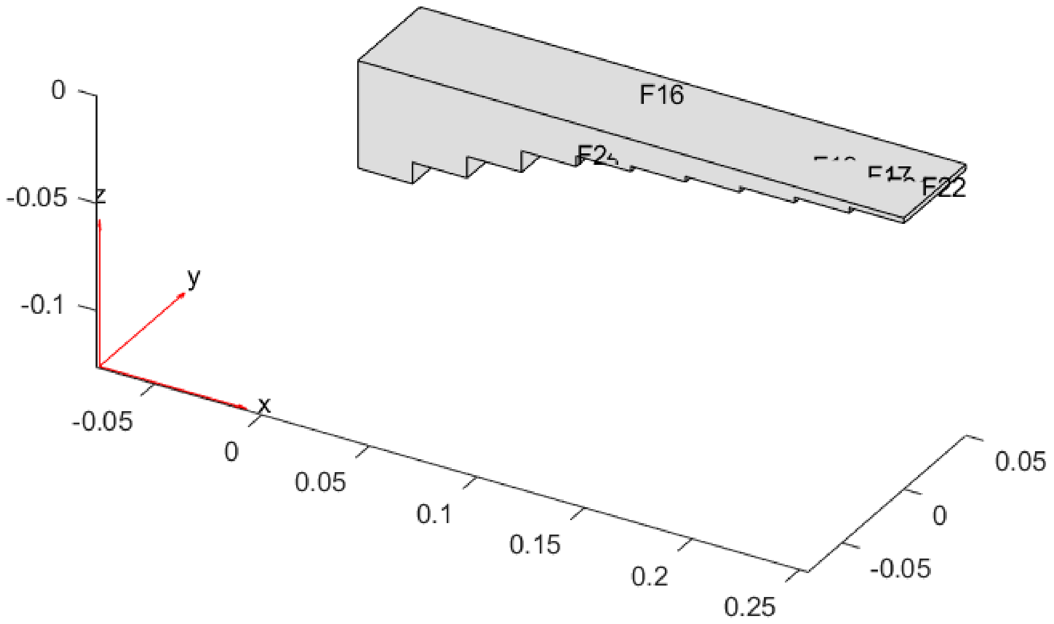

Figure 4.2 : Staircase stl file imported on MATLAB

After having identified the face in which we want to simulate the heat source (F16), we can proceed generating an appropriate mesh. In this case a compromise has to be found between the accuracy of the result and the computational cost. For this reasons, after a few attempts, we chose to use the following values:

- Hmax all over the model 0.01 m
- Hface (only on face 16) 0.003 m
- Growth rate 1.5

```
mesh=generateMesh(model,'Hmax',0.01,'Hface',{[16],0.003},'Hgrad',1.5);
```

Judging from the subsequent comparison with the experimental data, it would have been better to have a denser mesh on the upper surface. However, this would have resulted in excessively long calculation times. Therefore, it was planned to thicken the mesh exclusively along a hypothetical line of laser action (a sort of midline), but, unfortunately, Matlab only allows the application of a specific mesh with reference to well-defined geometric elements of the model such as faces, edges or vertices.

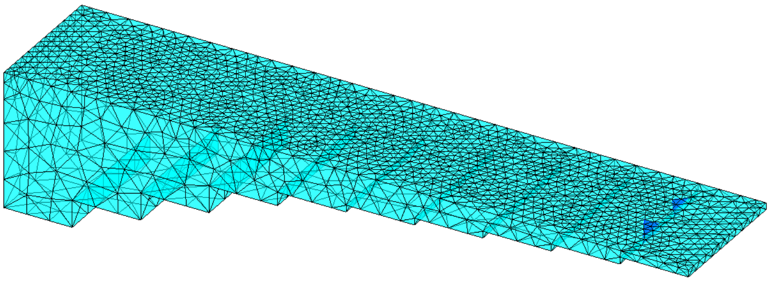

Figure 4.3 : Mesh definition

Thanks to the function FindNodes we were able to isolate the projection of the surface of the seventh step on face 16. This will allow to analyze the thermal transients on this part of the surface later.

```
Ef7step=findNodes(mesh,'box',[0.152 0.178],[0 0.06],[-0.001 0]);
```

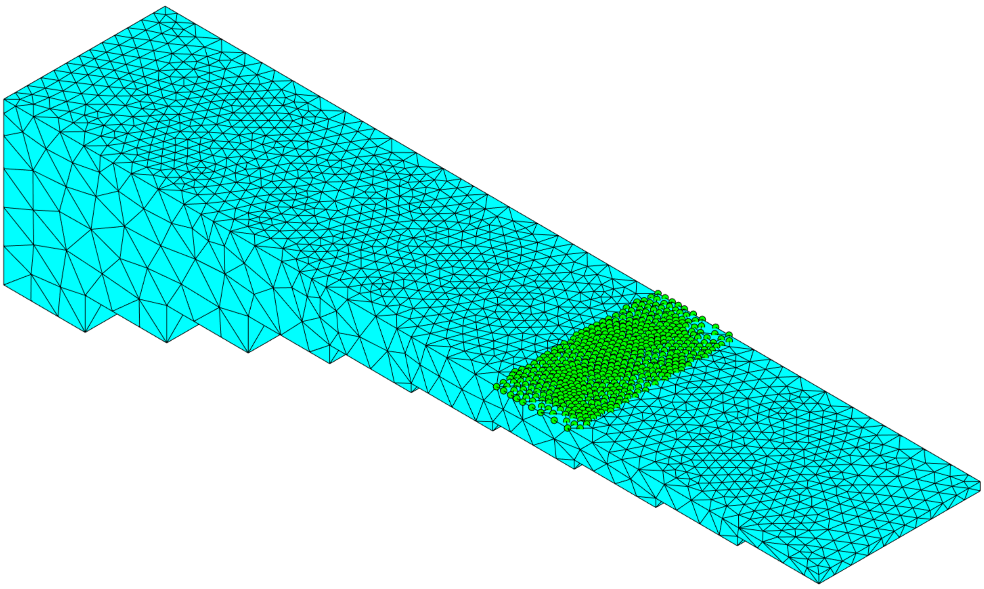

Figure 4.4 : Identifying the seventh step

We chose to simulate a laser heat source with a radius of 3 mm and a total power of 12.5 W.

```
global  r
r=0.003; % [m]
global    qtot
qtot=12.5;  % [W]
```

We can now evaluate the specific power output on the surface.

```
p=qtot/(pi*((2*r)^2)/4);  % [W/m2]
```

p $\cong$ 0.44 W/mm^2

The thermal transient consists of 3 seconds of heating with the laser switched on, followed by 7 seconds of cooling with the laser switched off. On the following figures it is possible to observe both the results after 3 and 10 seconds from the lighting of the laser source.

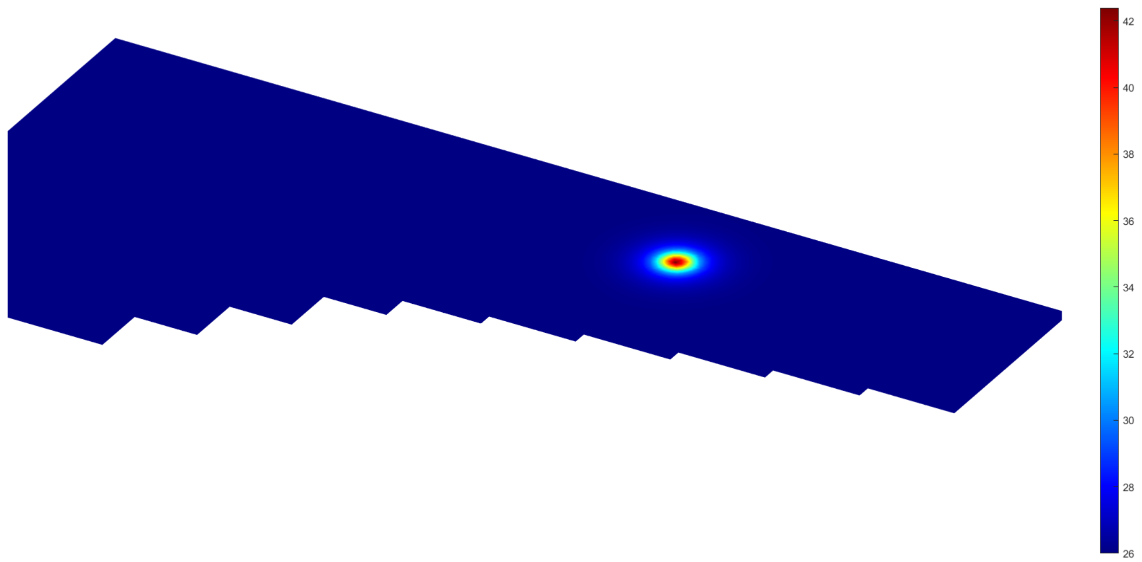

Figure 4.5 : Thermal response after 3 seconds of heating

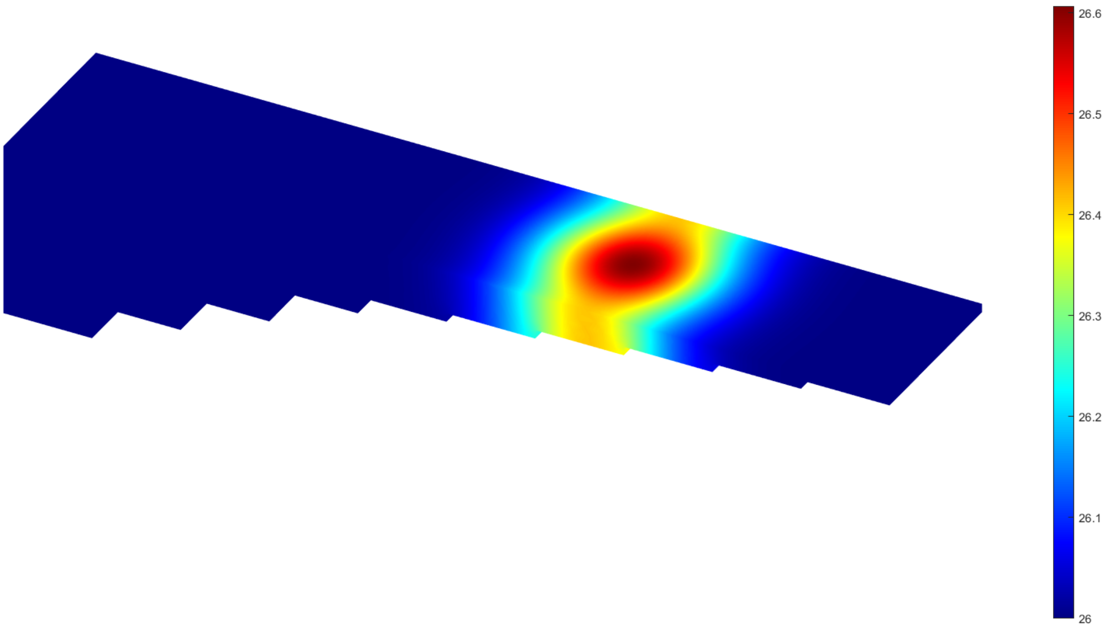

Figure 4.6 : Thermal response after 3 seconds of heating and 7 seconds of cooling

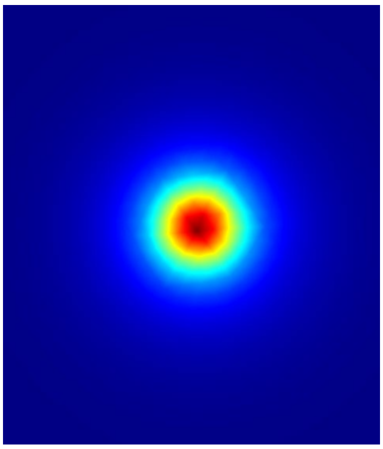

Figure 4.7 : Detail of gaussian input equation thermal response

As you can observe from this detail, the function in input is a gaussian equation:

$$q \;=\; C_2\, e^{-\frac{[(x-x_0)^2+(y-y_0)^2+(z-z_0)^2]}{c_1{}^2}}$$

Where:

- q = heat flux on the desired surface
- C_1 = radius of the beam [m]
- C_2 = Source Power Intensity [W/m^2]

At this point we decided to evaluate the maximum and the mean value of the temperature on the surface of the seventh step over time. Then, a few simulations were carried out, modifying some of the model parameters to see which of them had the greatest influence on the results.

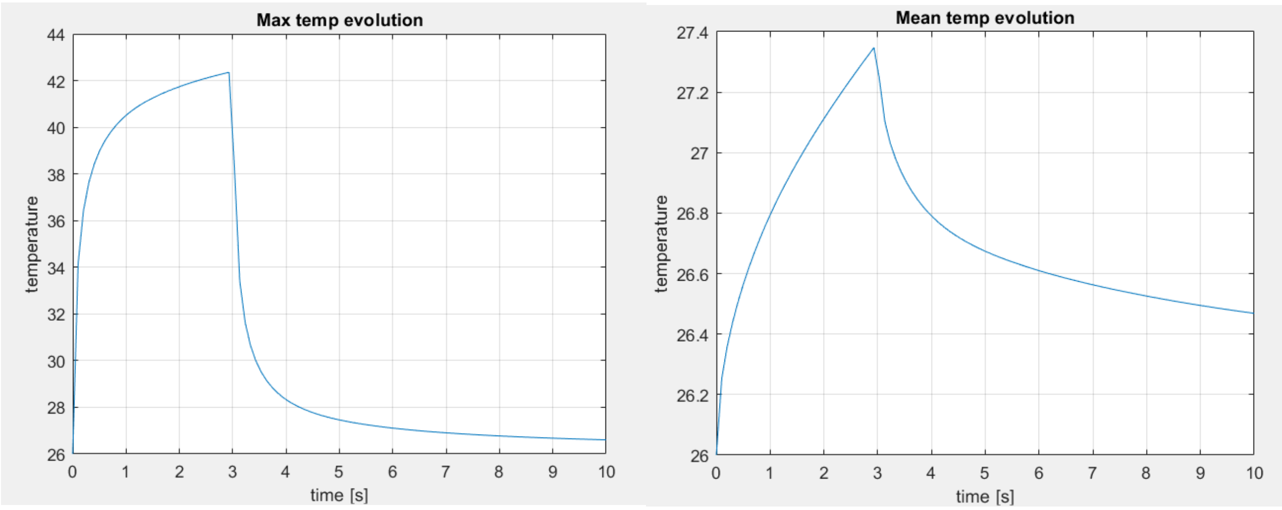

Figure 4.8 : Max temperature and mean temperature evolution of the seventh step

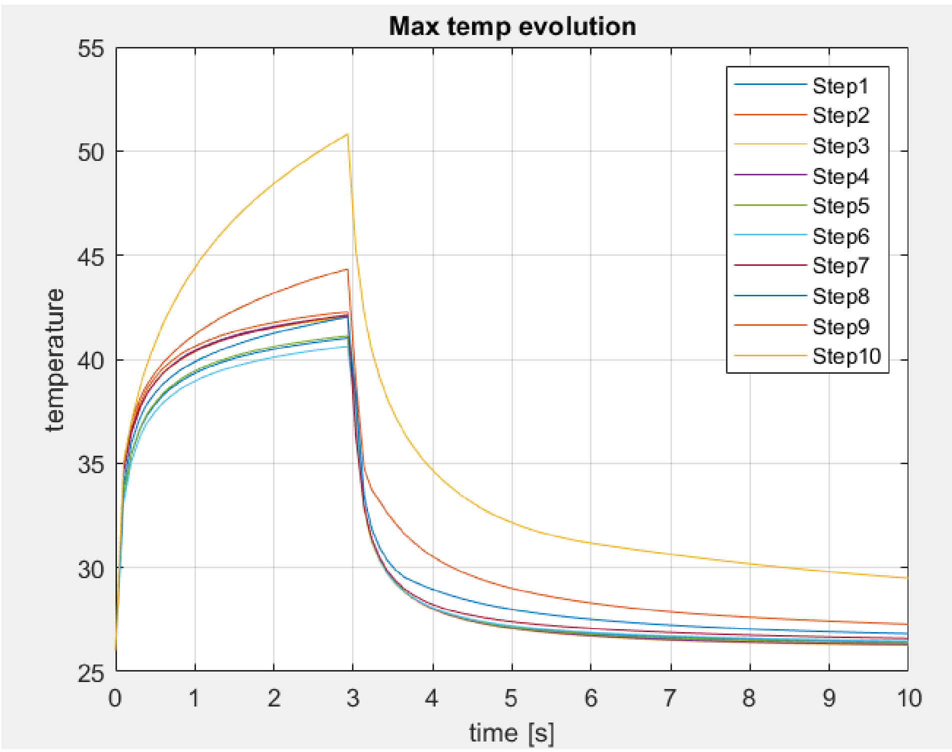

Figure 4.9 : Max temperature evolution of each single step

In this last figure we can observe an overview of the max temperature evolution in each step, where the thinnest steps reach higher temperatures. These results were also compared with those of the Ansys software, which confirmed the validity of the model. With the use of commercial finite element simulators, particular attention must be paid both to the choice of the appropriate tool for the problem to be analyzed and to the way in which the equations are processed. In contrast to solving by means of self-built algorithms, e.g. with the help of MATLAB, we don't know the simplifications or assumptions made behind the automatic interface. In the search for solutions, commercial solvers will always try to provide an output even if this has nothing to do with the actual physical behavior.

However, proceeding with the welding simulation on Matlab would have been extremely complex from the point of view of programming. For this reason we started investigating which software was best suited to our needs.

Therefore the choice now depends on whether we prefer a generic non-linear thermo-structural analysis software or a specific welding software. Although the latter may provide a simpler programming interface, it often has to cope with a less extensive management of variables, not allowing in some cases an efficient and precise parameterization of the welding process. For this reason, we decided to use the MSC Marc Mentat software. We will explain all the process in detail in the chapter dedicated to simulation.

Figure 4.10 : MSC Marc Mentat

4.2 MSC Marc Mentat simulation

4.2.1 3D Modeling

As we have already explained in the previous chapters, the process of simulation starts with the creation of a 3D model on Solidworks which is composed of three parts: two symmetrical plates 500x125x3 mm and the weld filler of the size shown in the following pictures.

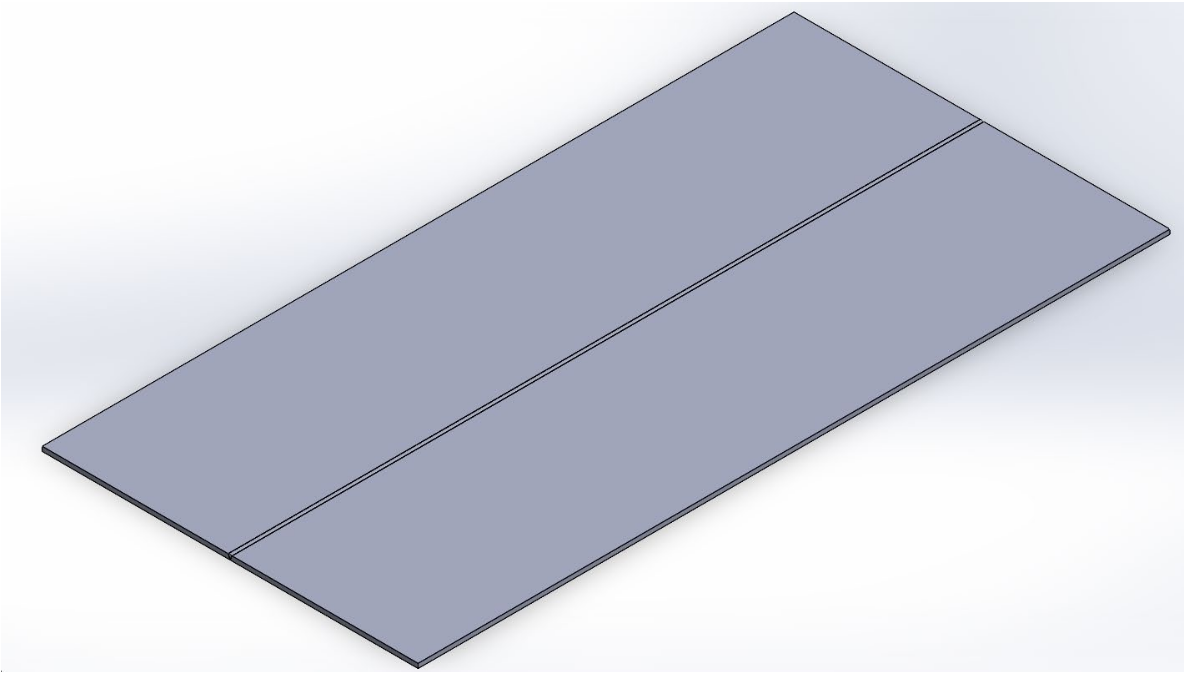

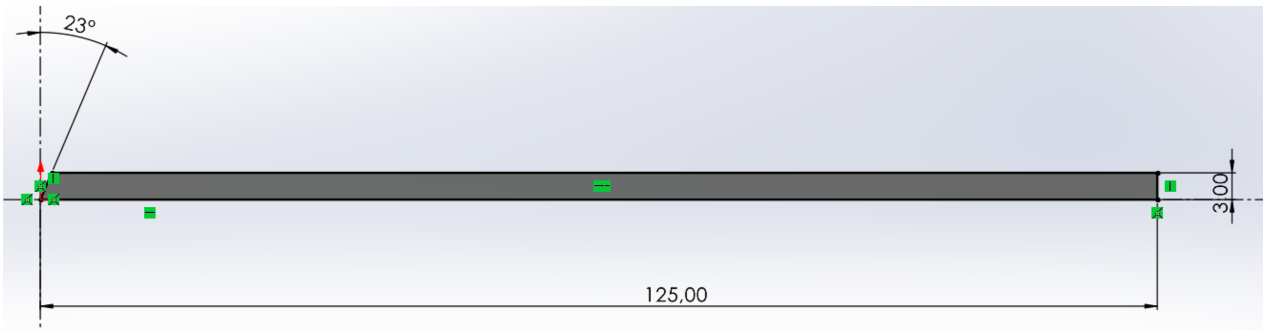

Figure 4.11 : Building of 3D Model on Solidworks

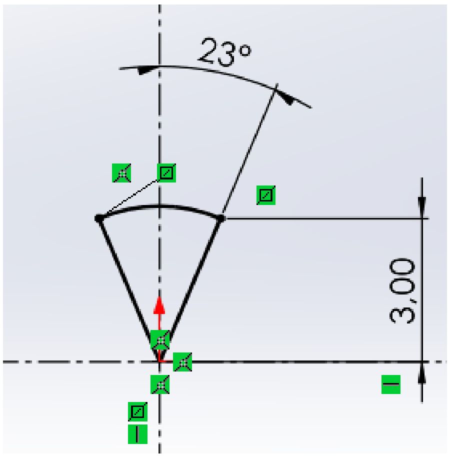

Figure 4.12 : V-shape Weld filler geometry

4.2.2 Meshing

Once the assembly, composed of two symmetrical plates as base material and the weld filler, is ready, we can start with meshing. As usual it is necessary to find a balance between the accuracy and the run time.

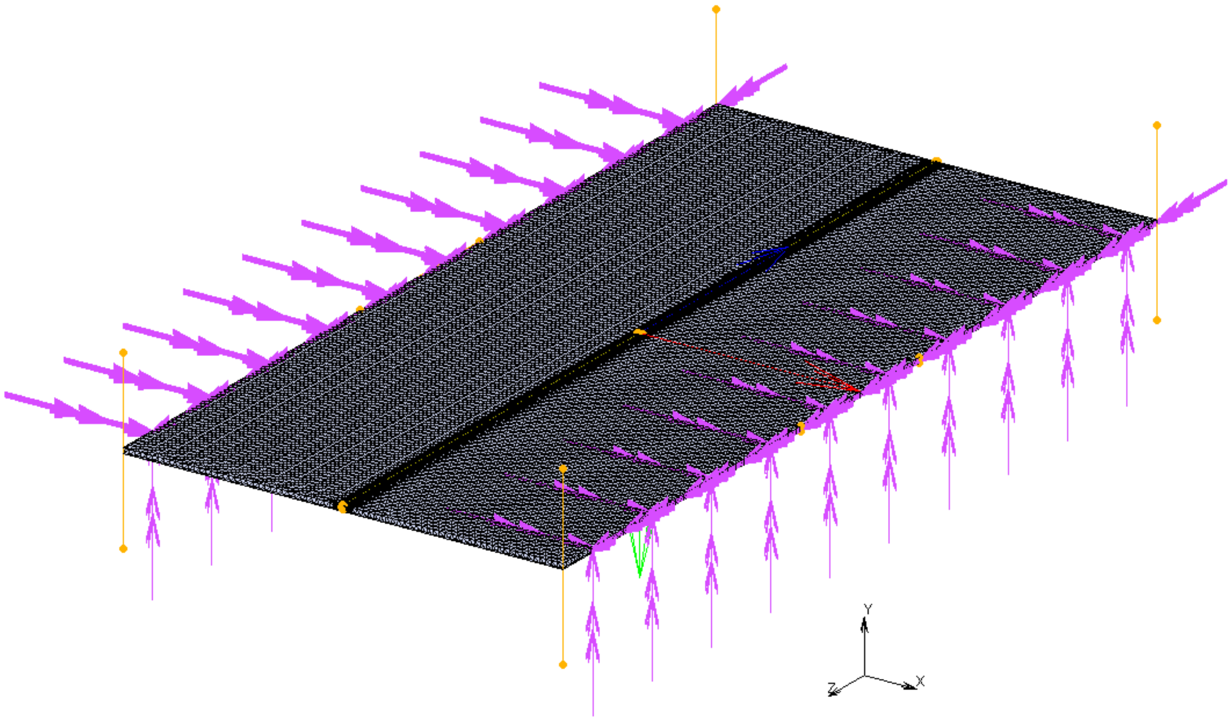

Figure 4.13 : Mesh definition

This model has a mesh which becomes finer and finer as it approaches the weld bead and it is composed of 39316 nodes and 123620 elements.

4.2.3 Material definition

For this simulation we used a DB.20MnCr5 as a multi-phase material, which takes into account all the structural and thermal properties of different phases of steel: austenite, ferrite, pearlite, bainite, martensite. This system is based both on TTT and CCT phase transformation types. All tables and material values were taken from the annexes directly on MSC Marc Mentat.

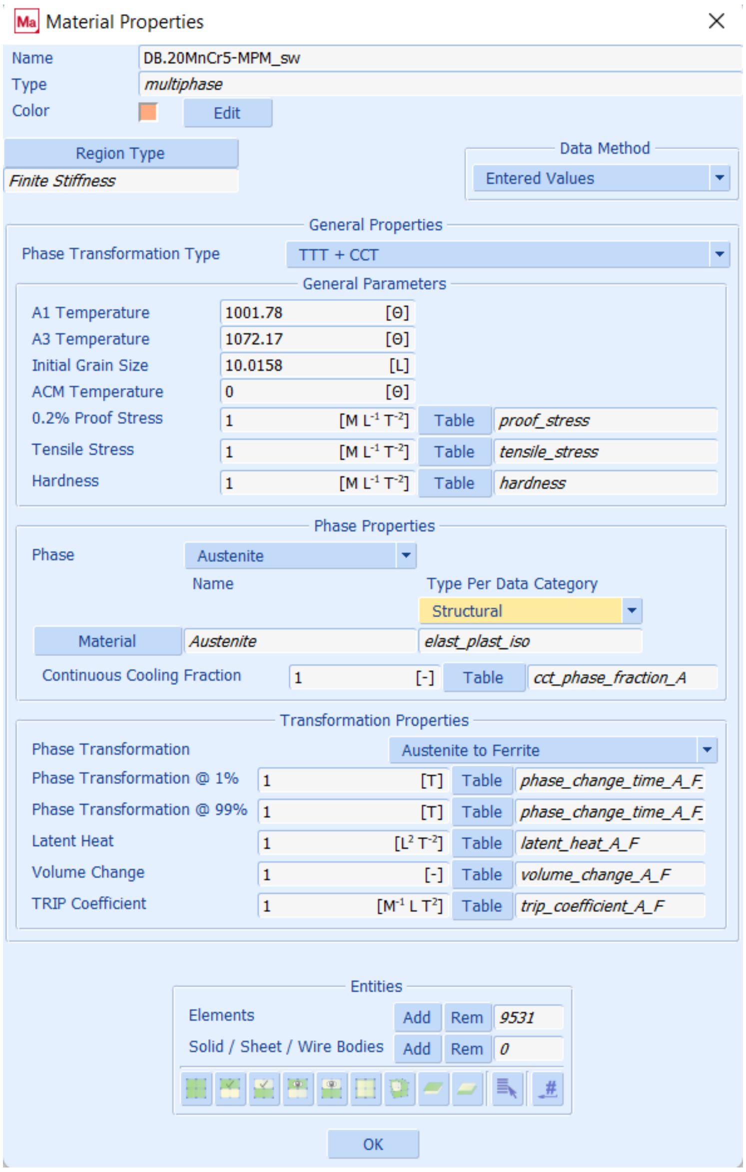

Figure 4.14 : Material definition

The tables illustrate the changes in all thermal and structural properties as temperature changes. As an example, we show the trend of the Young's modulus of austenite.

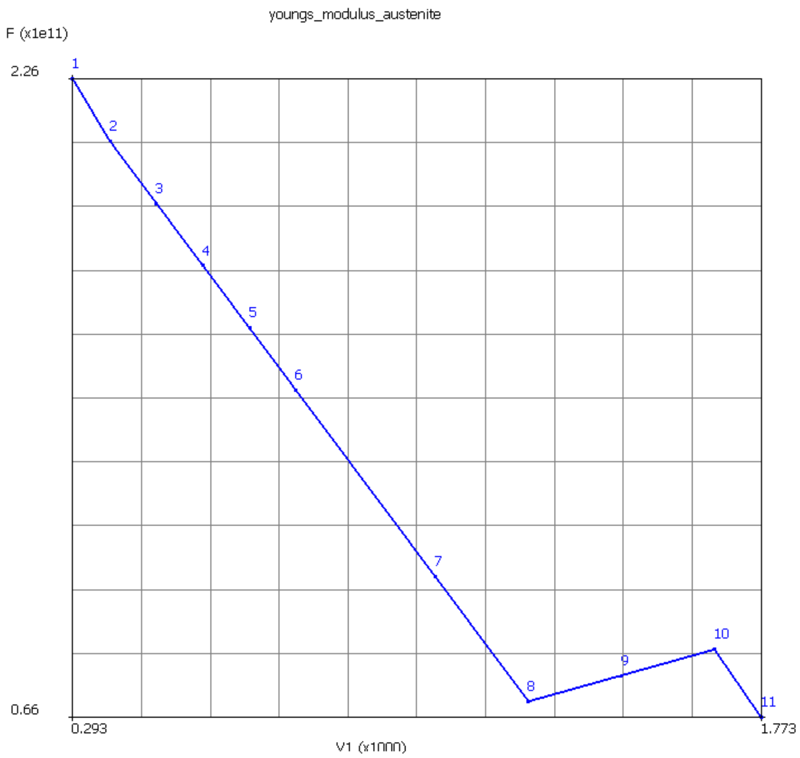

Figure 4.15 : Young modulus of austenite depending on temperature

4.2.4 Contact bodies

In the next step we defined contact bodies and interactions. We assumed that all three bodies are deformable while the interactions can be of two types: glued or touching. Usually the user must specify where and how contact occurs because this significantly influences computational time.

As reported in [20] contact is a boundary nonlinearity, wherein one body cannot penetrate another. The objectives of this analysis are summarized as follows:

- Define if two bodies are in contact
- Define where the region of contact is
- Compute the contact forces or pressure at the interface
- Define if there is relative motion between the parts after contact

After having decided which bodies will potentially come into contact, the algorithm detects the penetration and, to correct this irregularity, applies forces at the violated nodes. The main features of glued and touching contact are showed in the next figure.

Glued Contact	Touching Contact
• Allows two bodies to be fixed at the contact surface. • Don't need to have the same mesh on both sides of the bodies. • Good solution for joining two bodies having completely different mesh sizes. • If the stress in the contact exceeds a given stress, the contact is released (simulating bonding separation). • The elements involved in the contact region remain welded, regardless of what occurs in the surrounding structure. • Should not be used where the joint forces and stresses are of interest. • Good option when attaching a local model to a global one, for quick assembly modeling. • Possible to define glued contact after two parts come together.	• The bodies can move relative to one another, with the additional condition that one body is not allowed to penetrate the other. • Requires that the analyst manages several numerical parameters, to ensure that the solver computes the problem successfully. • Comes at a cost of a much longer analysis time.

We assumed deformable-deformable contact between our bodies: it means the they all have a similar stiffness and they all can deform.

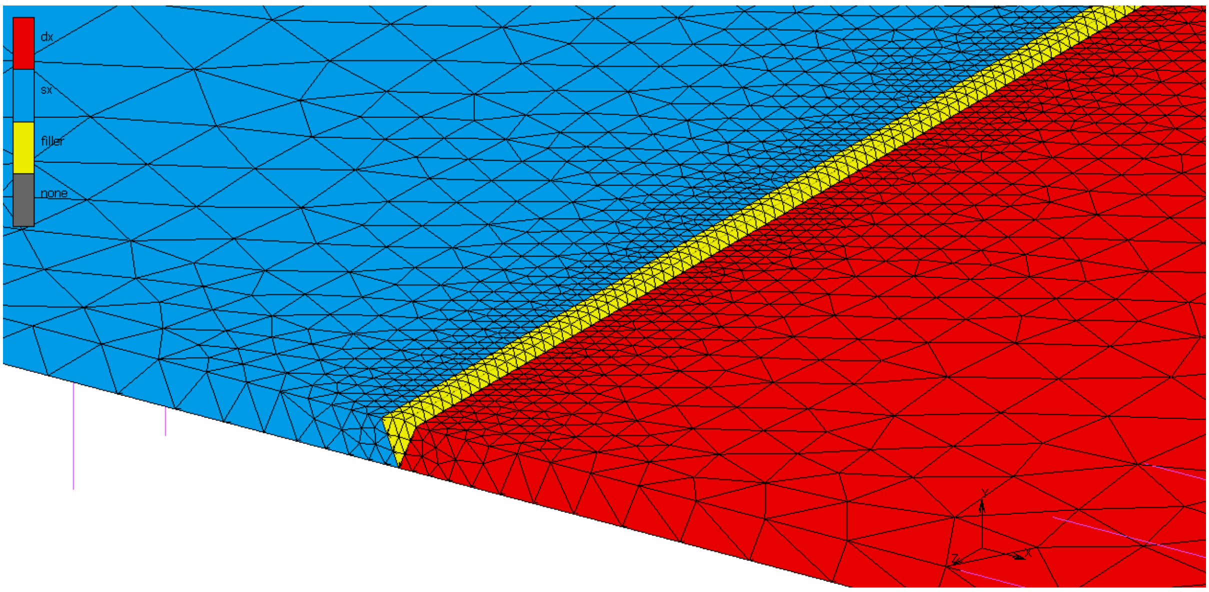

Figure 4.16 : Contact body definition

In the contact table it is possible to observe that there is a touching contact between the two plates (particularly important in the case of Y shape filler) and a glued contact for the interactions with the weld filler.

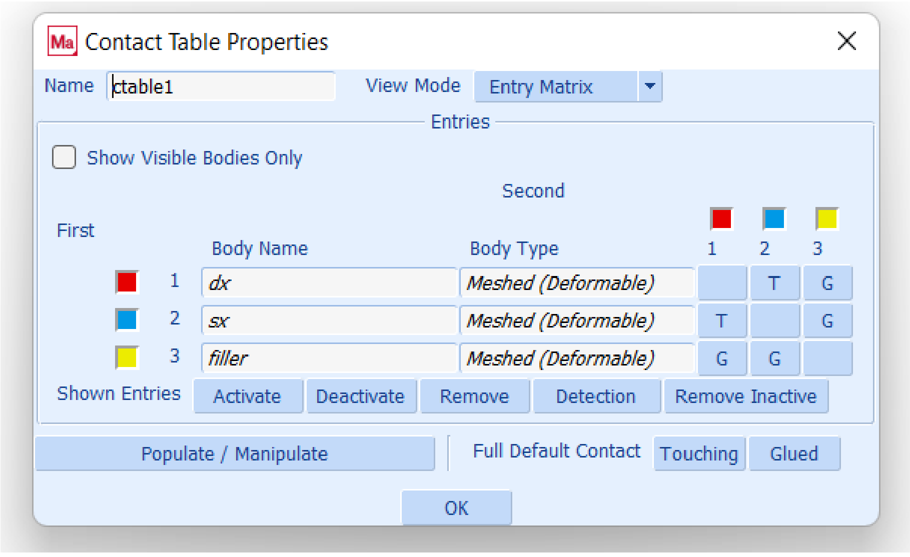

Figure 4.17 : Contact table properties

4.2.5 Weld path an weld filler

At his point it is necessary to define welding characteristics: weld path and weld filler. The first one is easily defined thanks to a Cartesian coordinate system centered on the middle of the weld beam.

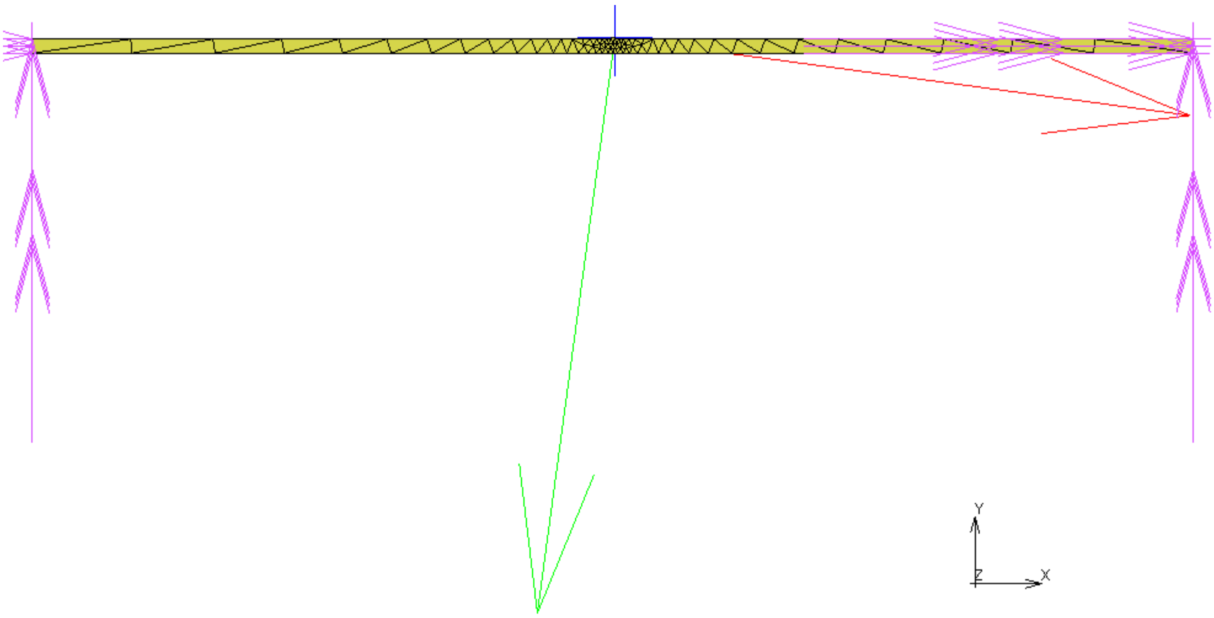

Figure 4.18 : Weld path definition

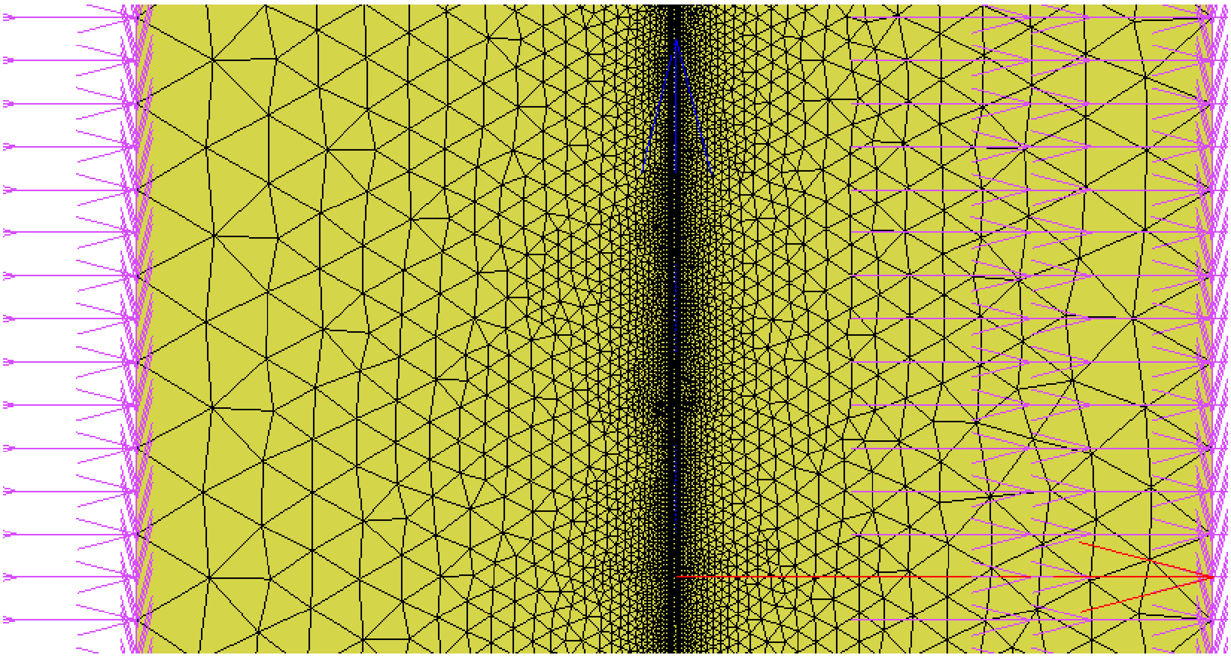

Figure 4.19 : Weld path orientation definition

To define the weld filler we only need to select the elements previously chosen in the geometry section as filler. In addition, for a simplified simulation of the heat source, a melting point temperature can be selected. In this way the simulation acts as if the filler material is inserted directly at the chosen temperature.

However, this choice would not allow us to manage the various welding parameters in the best possible way, which is why we chose to continue using volume weld flux as a boundary condition.

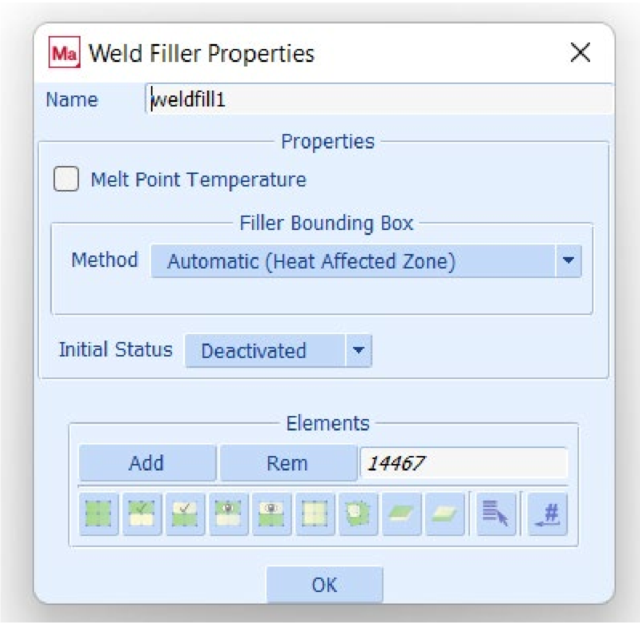

Figure 4.20 : Weld filler properties

4.2.6 Boundary conditions

In Volume Weld Flux boundary condition we need to specify the weld pool shape (Goldak model) and dimensions, velocity, power and efficiency. In this case, since the power was around 1700 W, we distributed 700 W (40%) on the filler side and the remaining 1000 W (60%) on the base material.

The other boundary conditions used are Structural Fixed Displacement and Thermal Face Film. The first one, which is visible from the previous images, simulates workpiece clamping during the welding process, whereas the second takes into account the convective and radiative heat exchange properties of surfaces with the external environment.

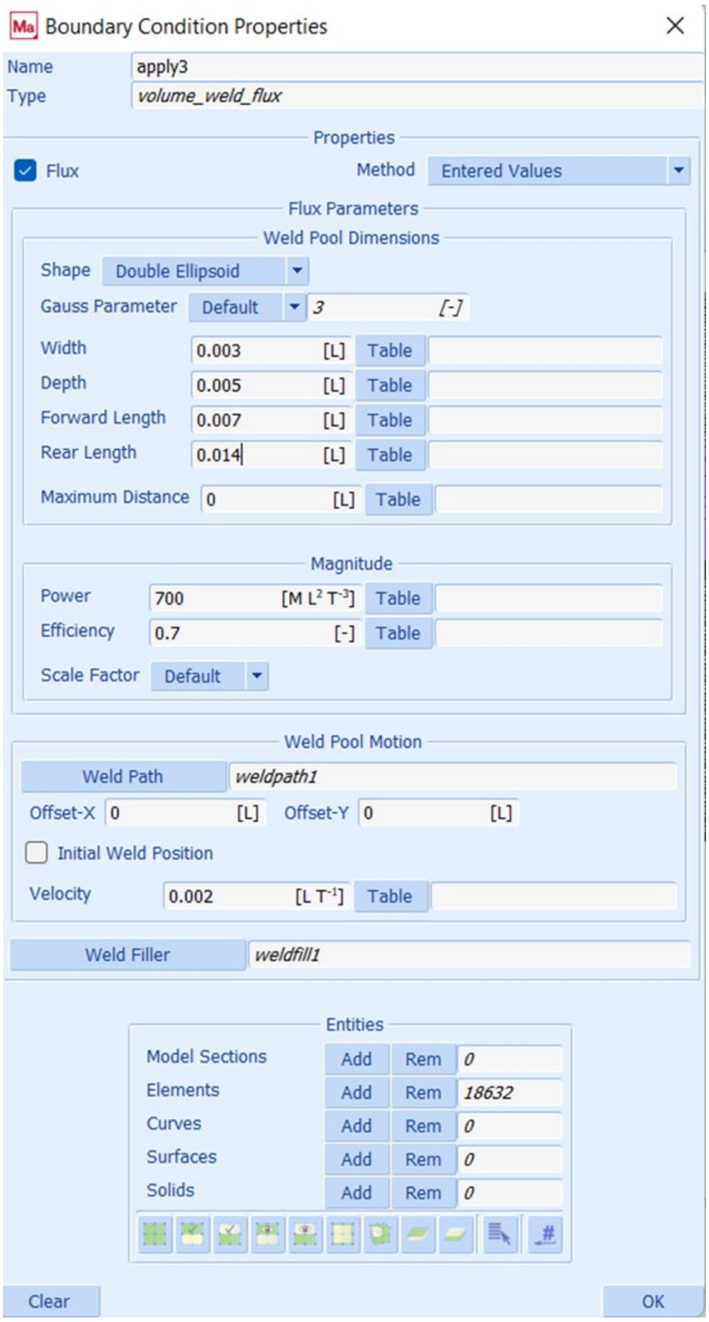

Figure 4.21 : Boundary condition properties – Volume weld flux

Figure 4.22 : Boundary condition properties – Face film

As reported by the ISO/TR 17671 regulation [21] the heat input value Q can be calculated as follows:

$$Q = k \frac{U \times I}{v} \times 10^{-3} \text{ in kJ/mm}$$

Where v is the welding speed [mm/s], I is the arc welding current, U is the arc voltage and k is the thermal efficiency factor, chosen according to the type of process (Figure 4.23).

In our experiment we used:

- U = 18 V
- I = 95 A
- v = 2 mm/s

With these values the heat input Q = 0.684 kJ/mm.

Process No.	Process	Factor k
121	Submerged arc welding with wire electrode	1,0
111	Metal-arc welding with covered electrode	0,8
131	MIG welding	0,8
135	MAG welding	0,8
114	Flux-cored wire metal-arc welding without gas shield	0,8
136	Flux-cored wire metal-arc welding with active gas shield	0,8
137	Flux-cored wire metal-arc welding with inert gas shield	0,8
138	Metal-cored wire metal-arc welding with active gas shield	0,8
139	Metal-cored wire metal-arc welding with inert gas shield	0,8
141	TIG welding	0,6
15	Plasma arc welding	0,6

Figure 4.23 : Efficiency of welding processes according to ISO regulation

Once the model is totally defined, we can proceed with choosing the total load case time and the stepping procedure. Since the welding speed is 2 mm/s and the workpiece is 500 mm long, we used a total time of 300s, to observe both the heating and the cooling transition. Then we decided to use a constant time stepping of 0.1s (3000 steps).

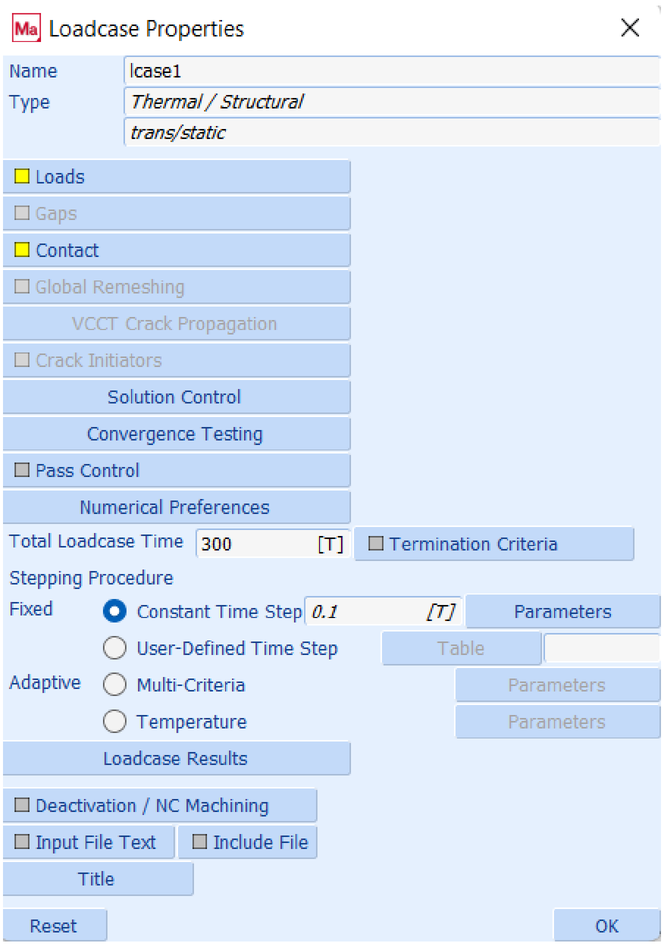

Figure 4.24 : Loadcase definition

Finally on the job results panel, we can select the outputs for the current job. In particular we are interested in temperature distribution, equivalent Von Mises stress and phase volume fractions.

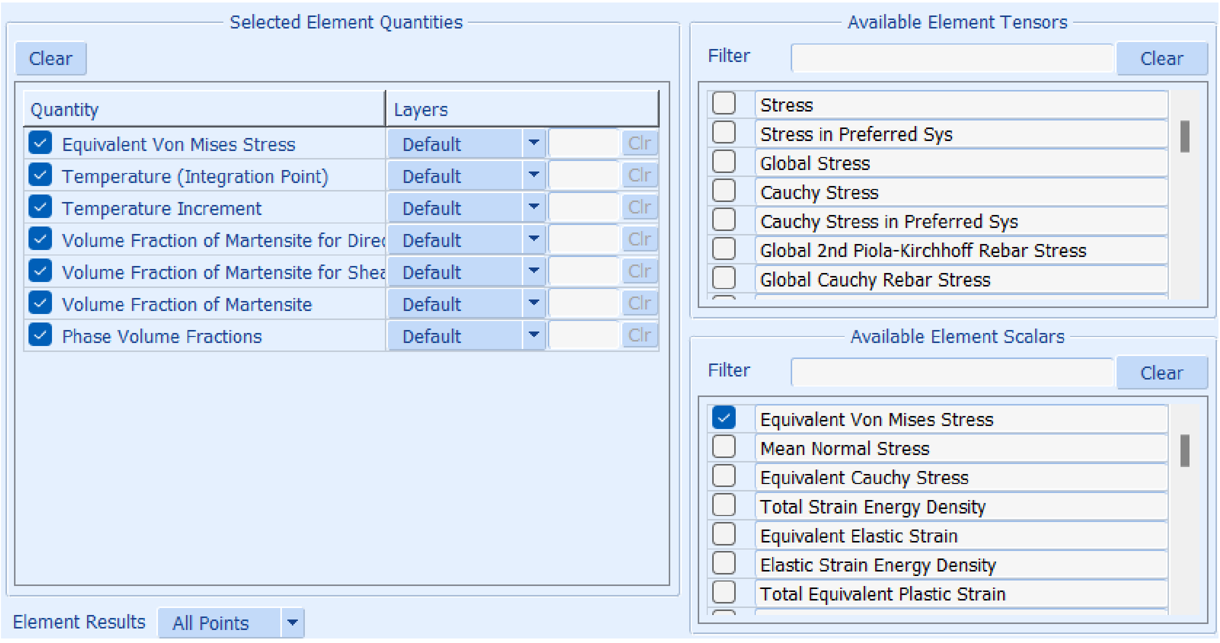

Figure 4.25 : Selecting requested outputs

4.2.7 Results

After running the simulation, we can now display the results.

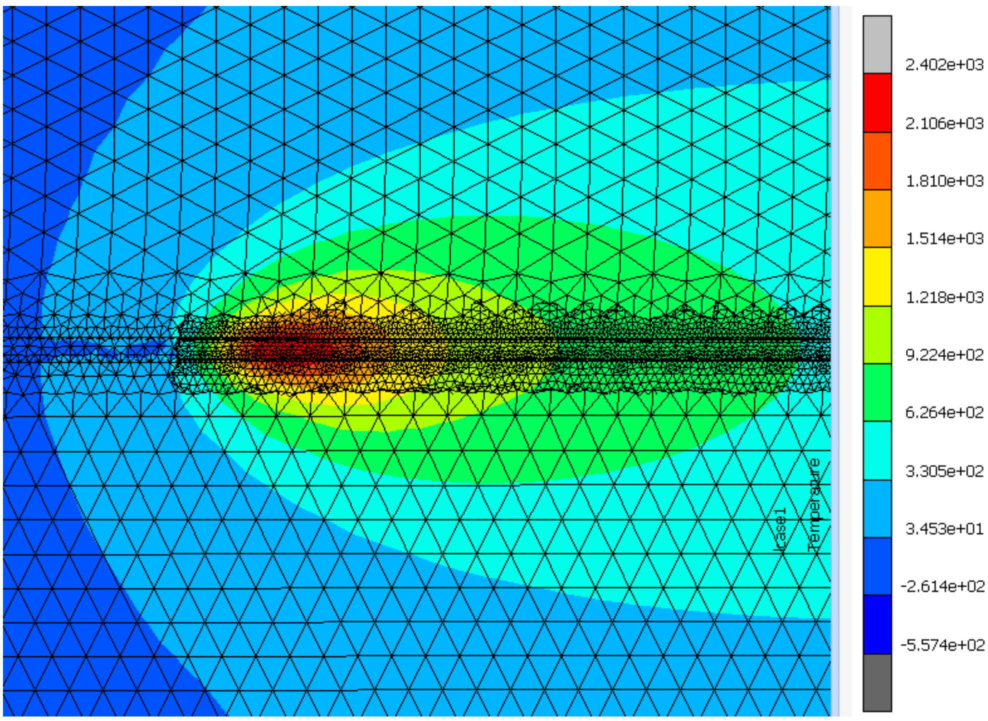

Figure 4.26 : Temperature distribution

As we can see from this figure, we also chose to use a local adaptivity criteria, which refines the mesh around the weld bead when the heat source moves.

The dimensions of the thermal imprint left on the workpieces give us an idea whether the parameters chosen for the Goldak model are correct, comparing them with the experimental ones. Considering the diameter of 2.5 mm of the electrodes and reconstructing the shape and dimensions of the thermal footprint from this unit of reference, we obtained that the measure of the section of the weld bead with temperatures above 300 degrees was around 33 mm, which is very close to the measurement of 35 obtained with the simulation. This means, in conclusion, that the Goldak model parametrization was quite accurate. To have another reference value, we considered a proportion of the dimensions on the total length of the 500 mm weld bead.

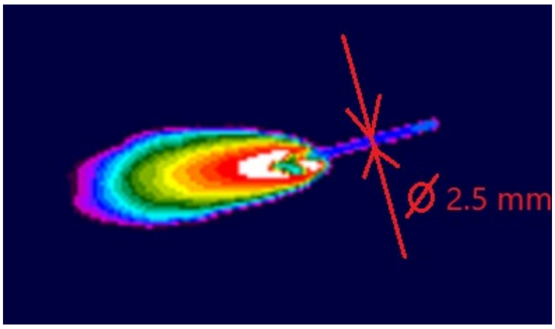

Figure 4.27 : Electrode measurements to convert pixels into length

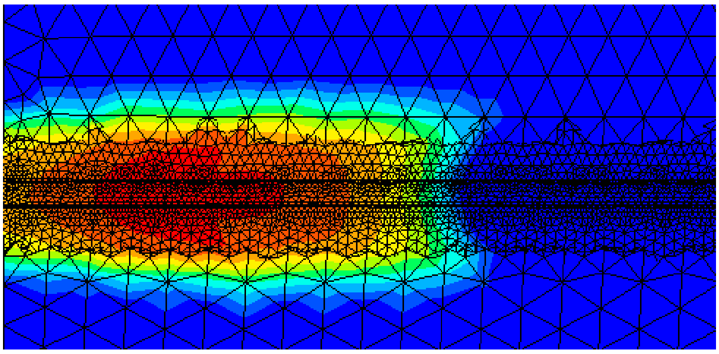

Figure 4.28 : Fraction of martensite

In the next figures we will show the main results from the simulation. Both the Equivalent Von Mises stress and displacement were evaluated at three different sections, with gradually increasing distance from the initial point (50 mm, 200 mm and 330 mm). They show how the maximum values of residual stress decrease along the length of the weld bead whereas the maximum values of displacement increase, narrowing the width of the section.

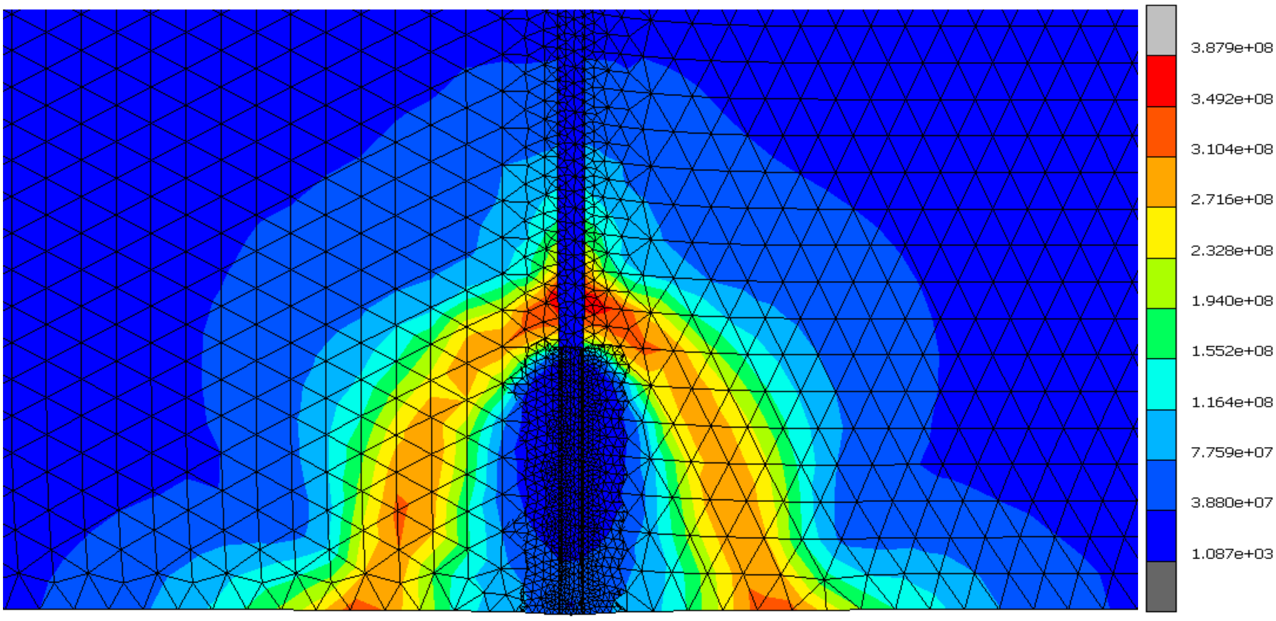

Figure 4.29 : Equivalent Von Mises Stress

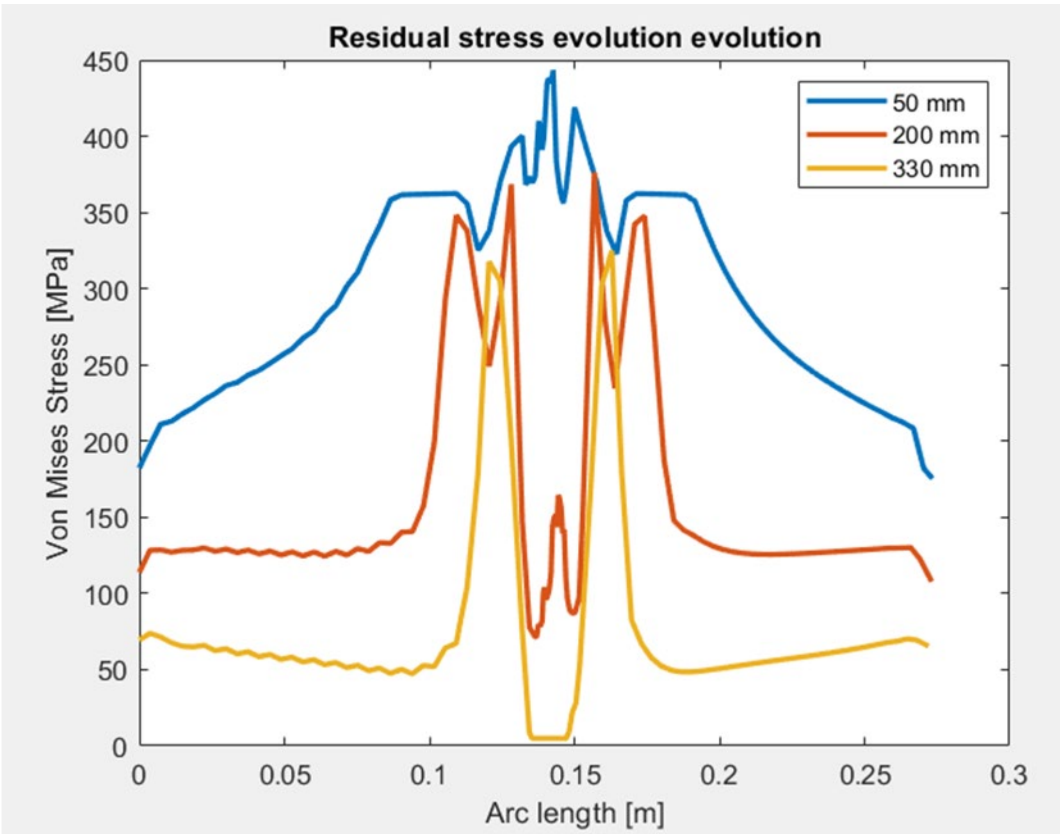

Figure 4.30 : Equivalent Von Mises Stress graph on maximum temperature section

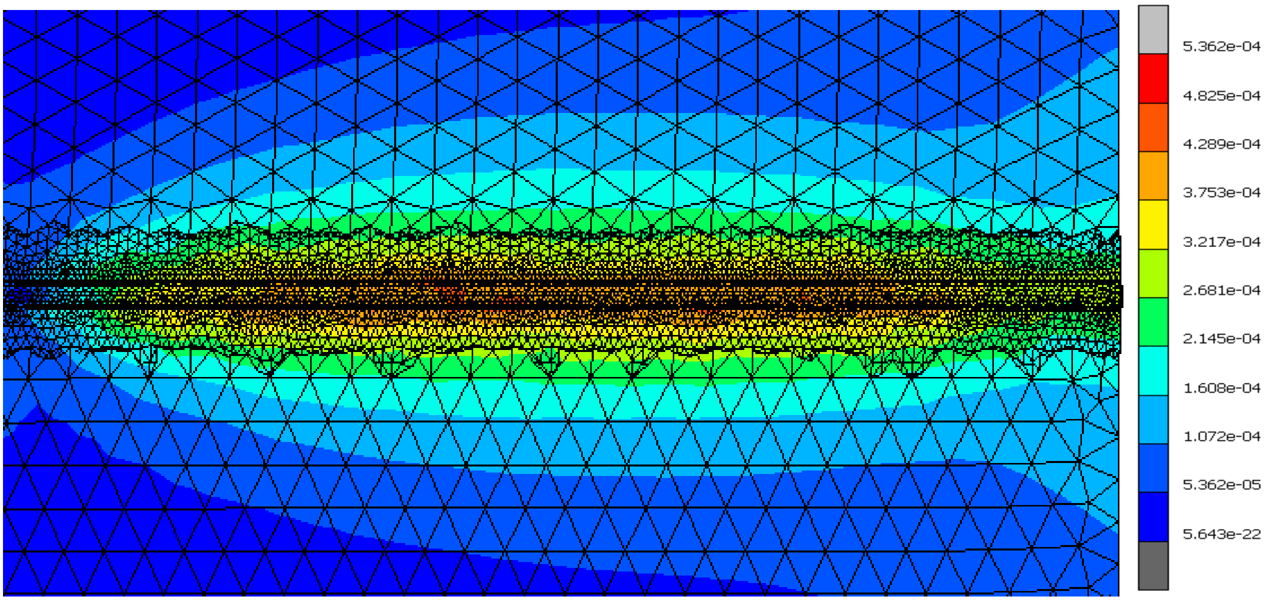

Figure 4.31 : Displacement

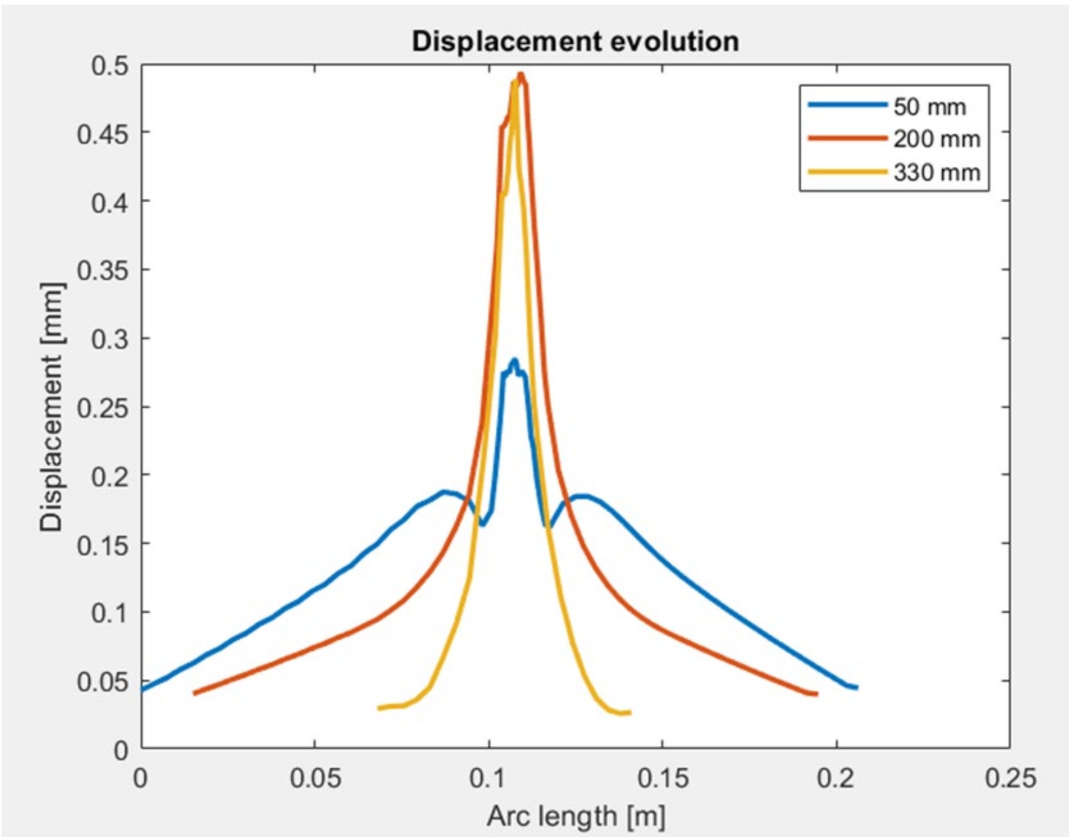

Figure 4.32 : Displacement on a weld filler section

4.2.8 Model validation

At this point, to assess whether the simulation is accurate in every aspect, we can compare the graphs of temperature evolution in time and space (along the profile or at sections) with the experimental results. Our simulation, in particular, showed a more accurate reproduction of the GMAW process.

First of all we have to say that there is a great difference between the maximum temperature reached in the simulation and in the experiment. This is due to the limits of the thermal camera, which is able to operate in a range of temperatures between 300 and 1500 degrees. Even if it shows temperatures up to 1700 degrees, this section can't be taken into consideration because the accuracy in this region may not be reliable. In conclusion we will mainly focus our attention on the cooling transient rather than the heating transient.

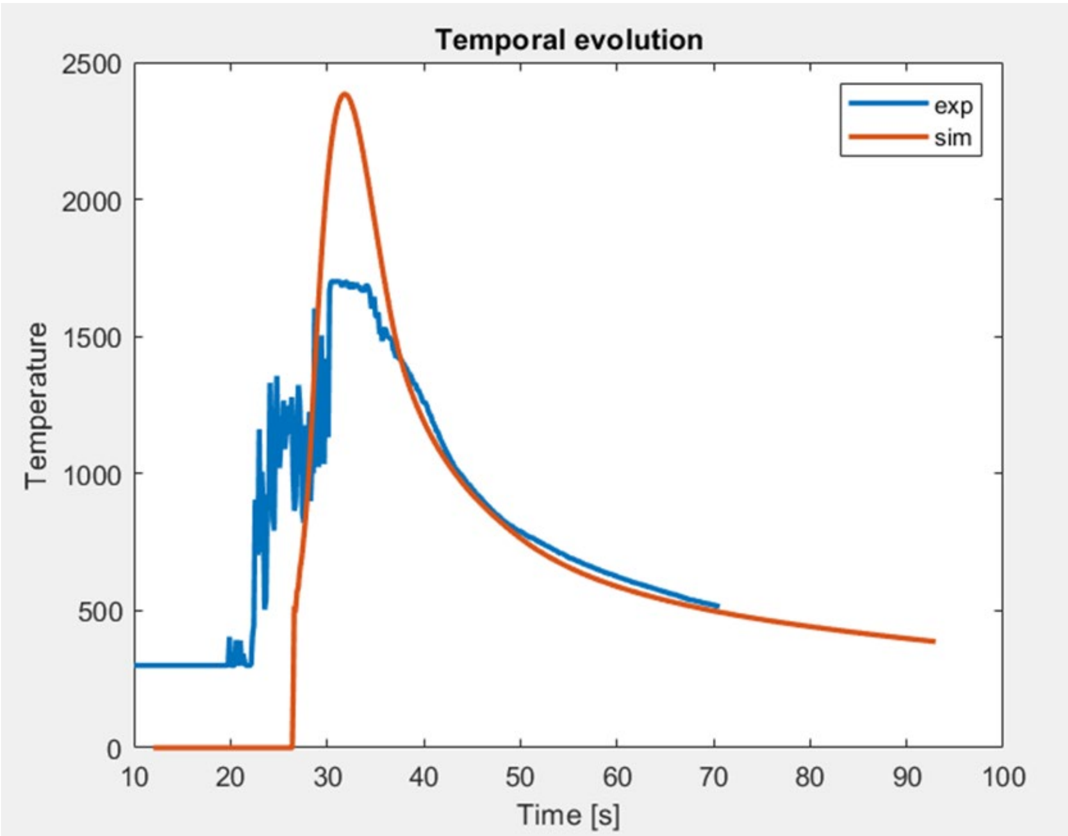

Figure 4.33 : Temporal evolution comparison between numerical and experimental results for 5 mm SMAW Butt welding

In this first figure, after the fast heating transients which share more or less the same gradient, we can see how the experimental saturation correctly covers the gap of the simulation. This means that that the simulation adequately reproduces the thermal phenomenon of the welding process. The slight separation between the two curves could also be due to the saturation of the experimental values at 1700 degrees.

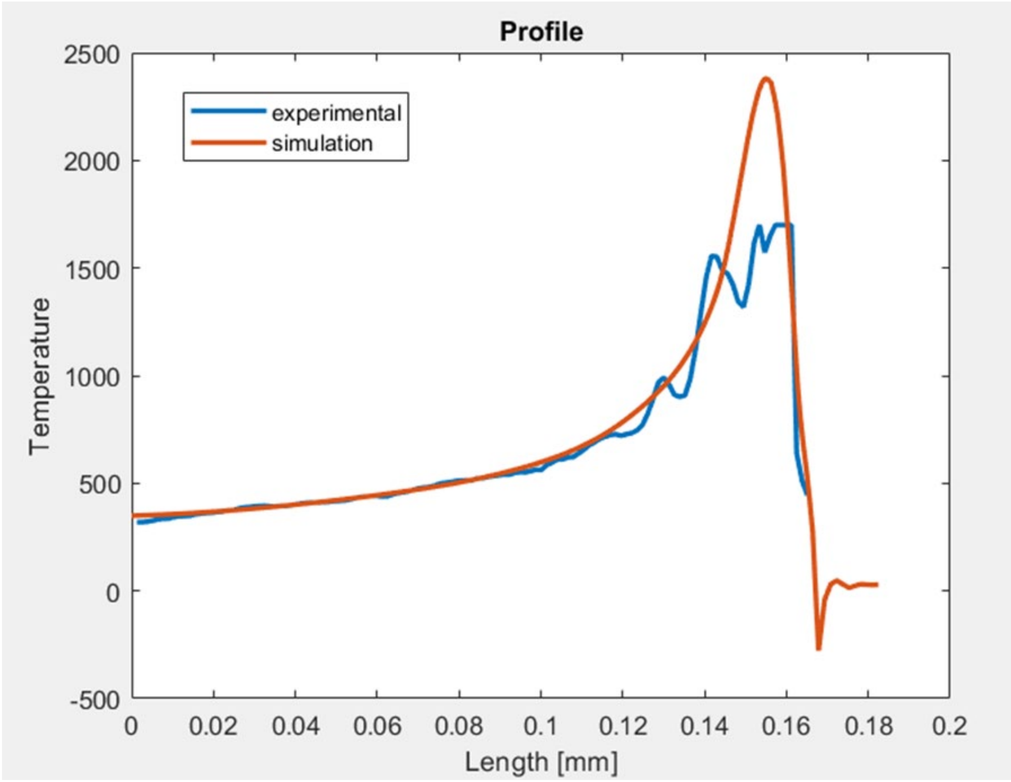

Figure 4.34 : Profile temperature distribution comparison for 5 mm GMAW welding

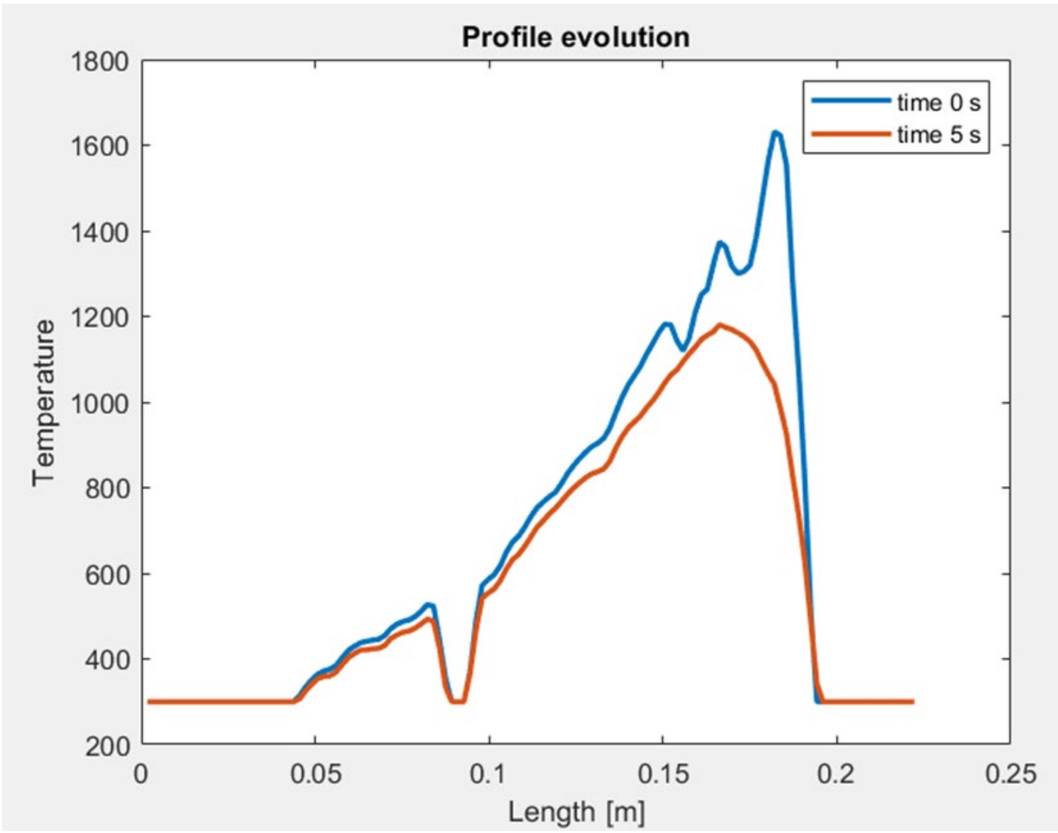

Figure 4.35 : Defect detection over time for 3 mm GMAW welding

Moving to the temperature distribution along the profile, we can observe a saturation at 1700 degrees which covers the gap of the simulation that reaches 2350 degrees. Then the temperature slowly decreases following perfectly the path of the simulation even though the experimental curve is a bit less regular. This kind of behavior could be related to the welder which moves the torch by swinging it in a direction perpendicular to that of the weld bead, unlike the simulation which moves in a straight line. If we wait a few seconds this irregularities disappear (Figure 4.35), whereas the presence of defects remains and they don't change their position in time.

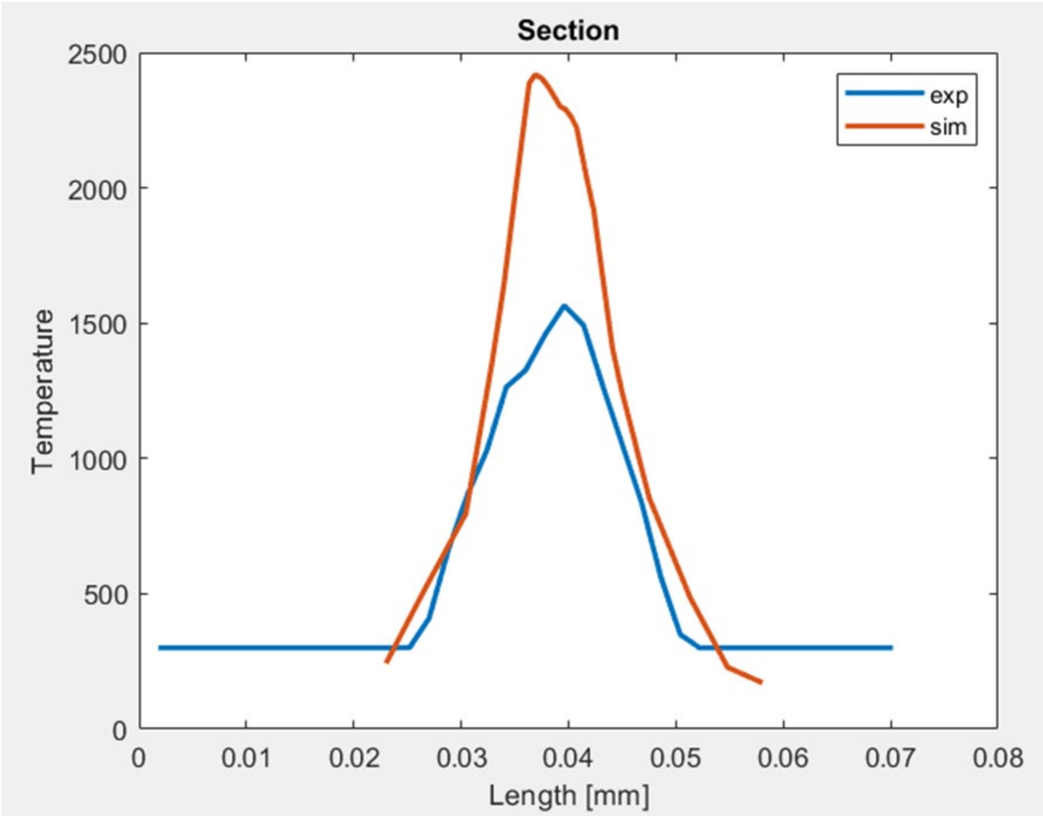

Figure 4.36 : Section temperature distribution comparison for 5 mm GMAW welding

The temperature distribution along the section instead, shows an experimental curve slightly tighter than the simulation one. However this phenomenon can be related to the minimum temperature of 300 degrees detected by the thermal camera, which abruptly lowers the gradient around those temperatures.

5 METALLOGRAPHY

5.1 Experimental procedure

In order to metallographically characterize the specimens used, we decided to select two welds for microscopic analysis :

- 5 mm SMAW butt joint
- 5 mm GMAW butt joint

First of all we need to cut the plates with a liquid cooled metallographic miter saw.

Figure 5.1 : Liquid cooled metallographic miter saw

The next steps are grinding and polishing: this process is carried out by gradually replacing finer abrasive papers.

Figure 5.2 : Metallographic grinder/polisher

Once the piece is perfectly polished we need to proceed with the etching process: in both cases we used NITAL, which is a solution of nitric acid and alcohol (usually methanol or ethanol).

Now the pieces are ready to be observed under the microscope. We used two different microscopes, one more suitable for macrographs, the other for micrographs.

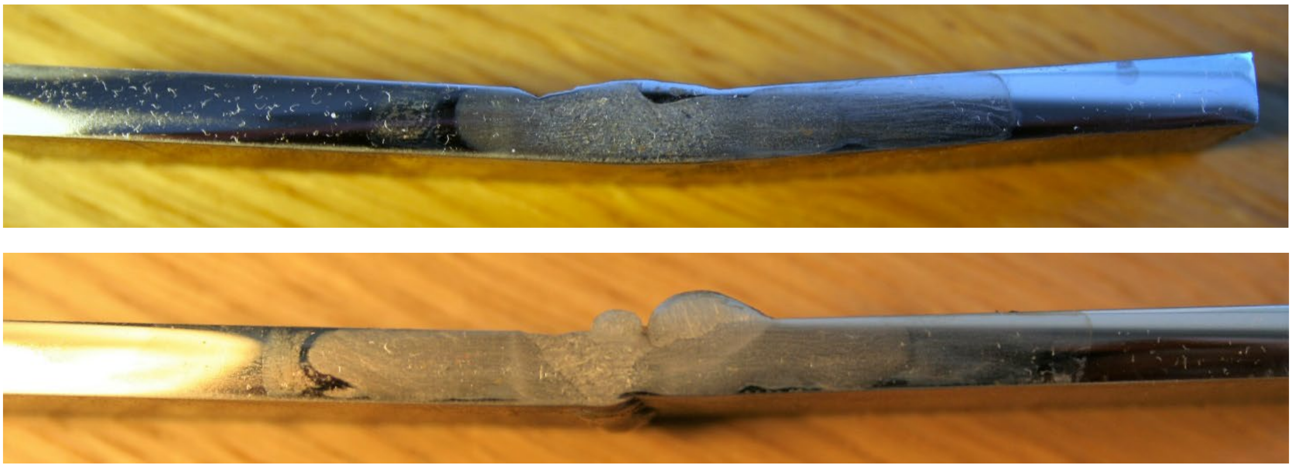

Figure 5.3 : Cut plates of SMAW and GMAW welding

In general the formation of martensite is unwanted, due to its hardness value which could bring to cold cracking. Whereas the formation of bainite is acceptable as it is less hard than martensite and delivers strength to the weld. [19]

At this point we can compare the experimental macrographs with the distribution of different phases in the simulation. In particular we will focus on the heat affected zone (HAZ), represented by the area between the weld and the unaffected base material. The size of the HAZ is mainly influenced by the level of thermal conductivity, density and specific heat. The next figure shows us what we expect from a metallographic analysis. In particular we distinguish four main different zones: weld metal zone (WM), coarse grain heat affected zone (CGHAZ), fine grain heat affected zone (FGHAZ) and base metal (BM). [22]

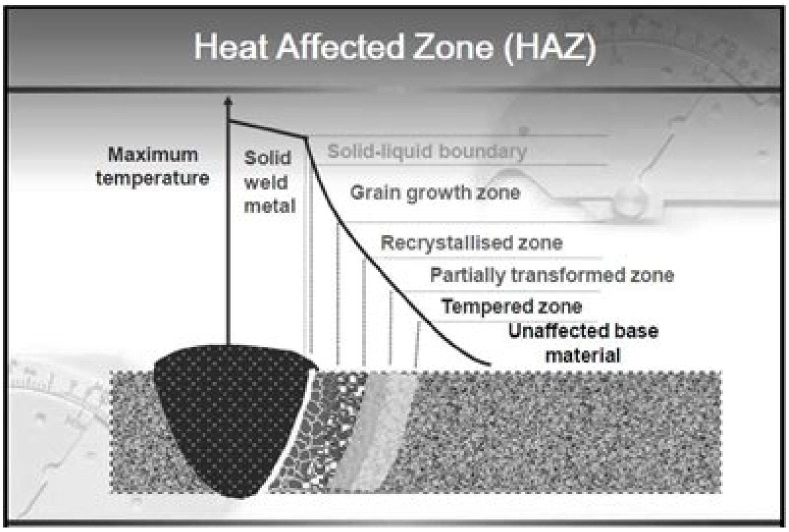

Figure 5.4 : Distribution of microstructures on the HAZ

5.2 Macrographic analysis

As shown in Figure 5.4, in this metallographic analysis we were able to distinguish between fused zone of the weld bead, HAZ and base material, thanks to the different colors, shapes and shading of the cut section.

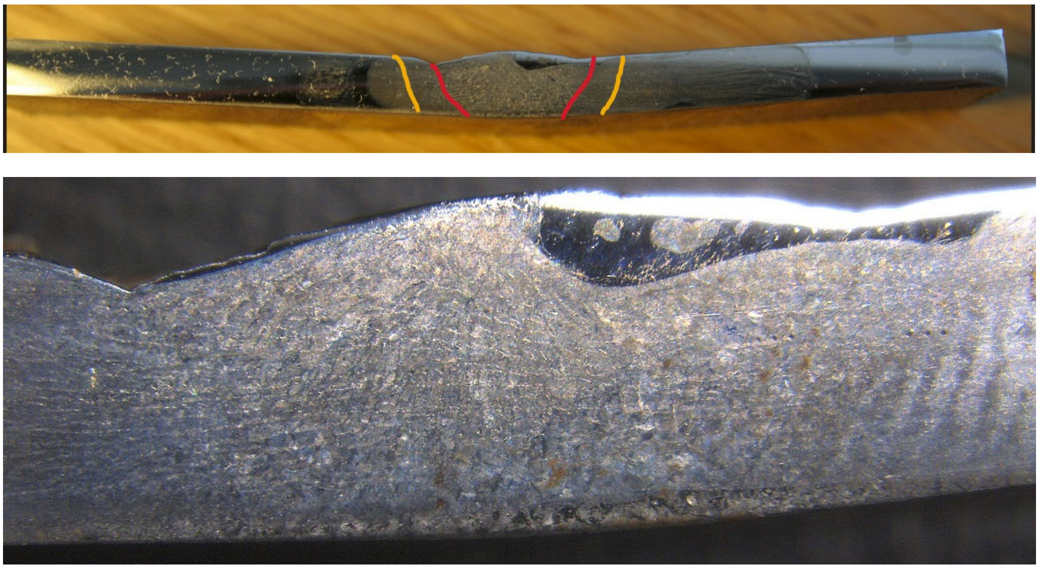

Figure 5.5 : Experimental SMAW weld profile and zoom on the weld bead: red line for the fused zone, yellow line for the HAZ

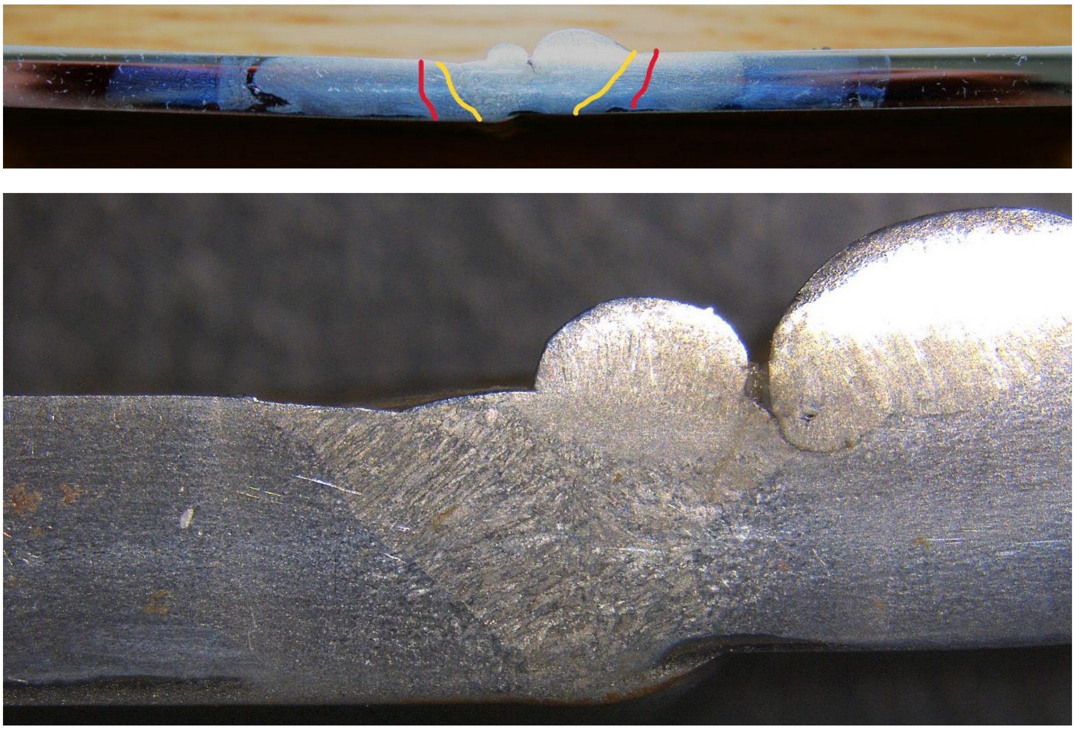

Figure 5.6 : Experimental GMAW weld profile and zoom on the weld bead: yellow line for the fused zone, red line for the HAZ

As already mentioned in chapter 3, the execution of a second welding pass resulted in the formation of a large crack, observable even by a simple visual inspection on the workpiece.

We can now proceed with the measurements of the dimensions of the various zones to compare them with the simulation results and to further validate the effectiveness of the numerical model.

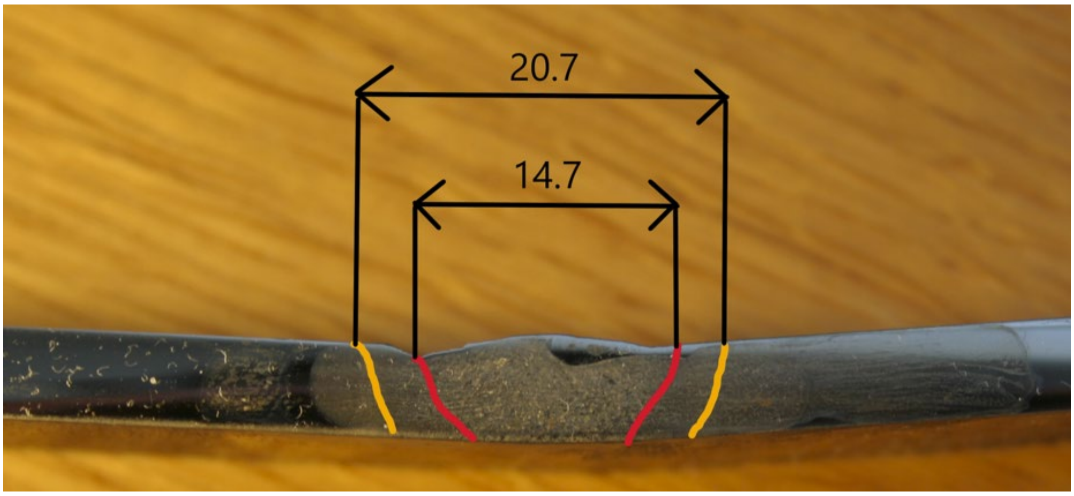

Figure 5.7 : Measurement of the fused zone and HAZ of SMAW section of the workpiece

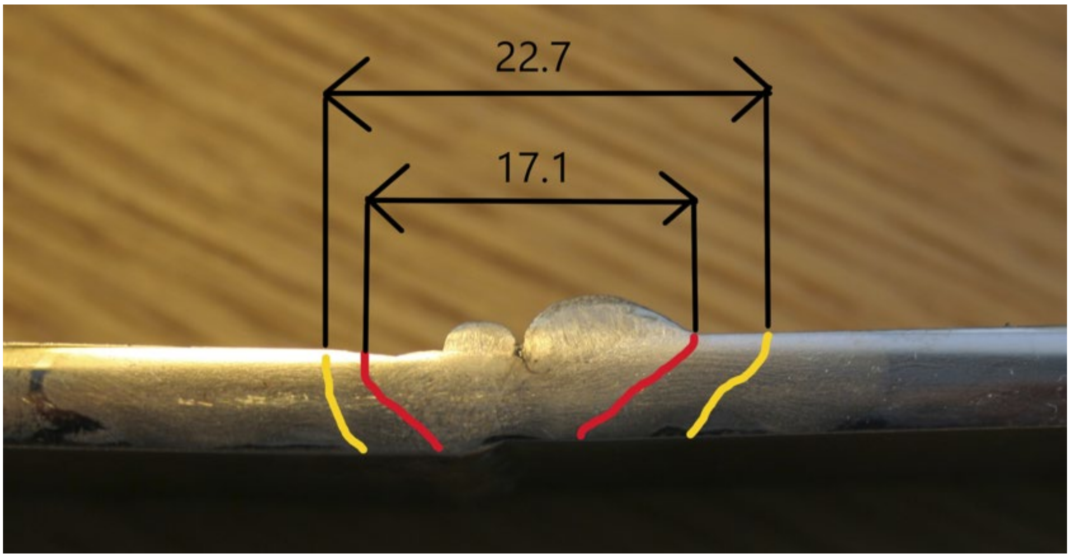

Figure 5.8 : Measurement of the fused zone and HAZ of GMAW section of the workpiece

From the simulation analysis we detected the presence of microstructures assessed as a percentage along a section of the workpieces. All the data were picked up on the same section, except for the austenite data, which were taken at the end of the weld, an area that still has high temperature values due to the short time elapsed from the electrode detachment.

In order to verify the effect of the heat source along the depth, we checked the presence of ferrite both along the upper and lower surface. The results showed a remarkable regularity of the microstructures along the depth, probably due to the thin thickness of the plates (3 mm).

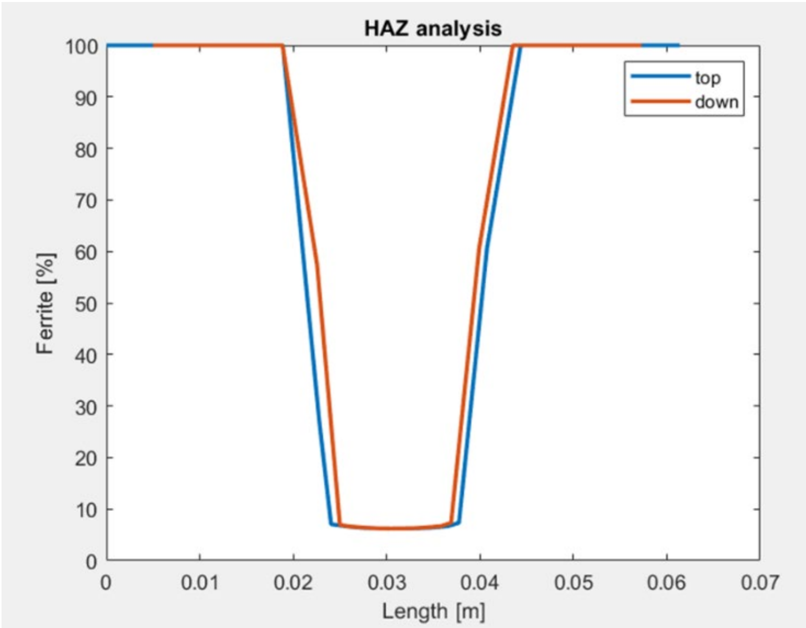

Figure 5.9 : Distribution of ferrite on the upper and lower surface sections

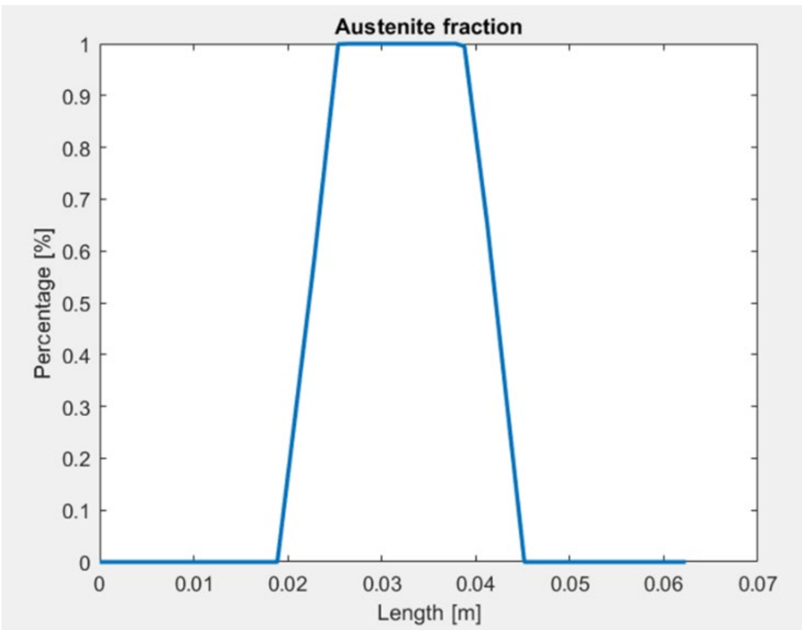

Figure 5.10 : Distribution of austenite on the highest temperature section

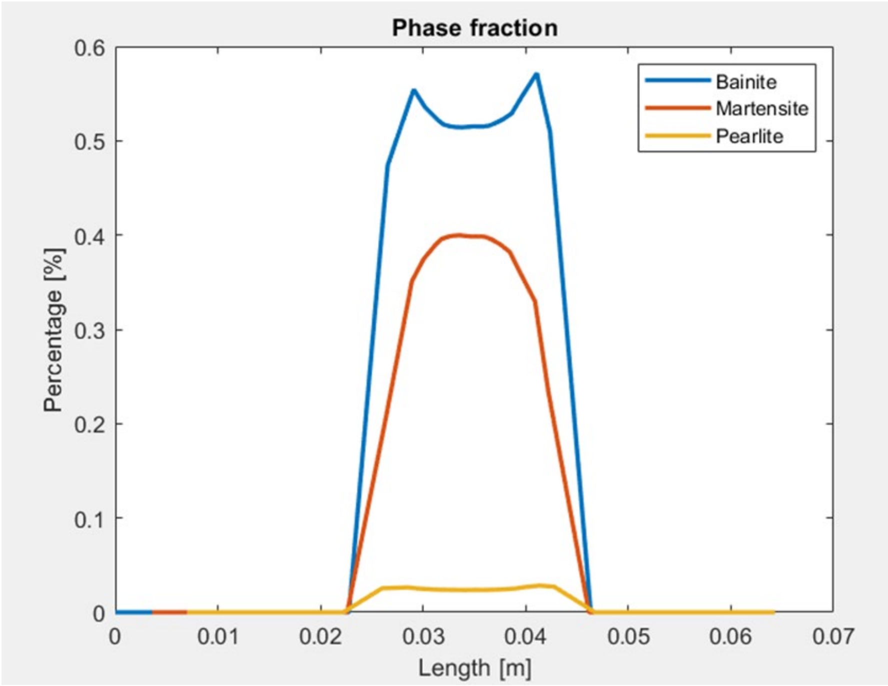

Figure 5.11 : Distribution of bainite, martensite and pearlite along a section of the weld bead

Following the passage of the heat source and the subsequent cooling transient, the distribution of microstructures on the weld bead is roughly as follows : 56% bainite, 41% martensite and 3% pearlite.

Considering the beginning of the HAZ as the zone where the percentage of ferrite starts to decrease, the previous graphs show values around 24 mm, which is quite consistent with the experimental value of 22.7 mm found in the case of GMAW welding.

5.3 Micrographic analysis

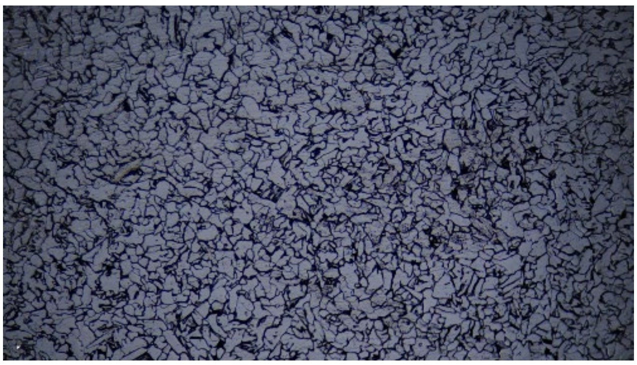

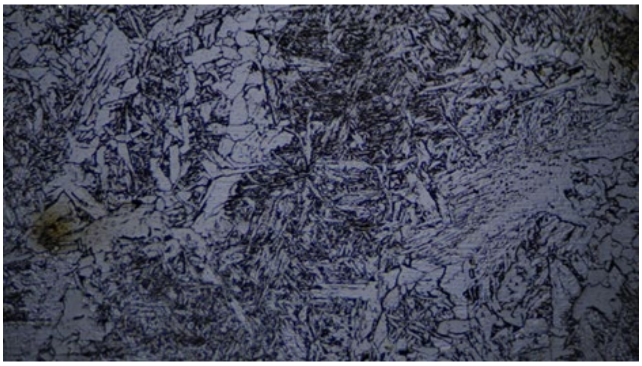

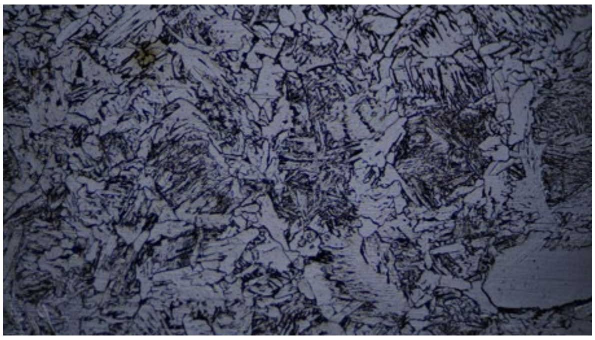

Figure 5.12 : Base material, HAZ and weld bead microstructures on SMAW workpiece

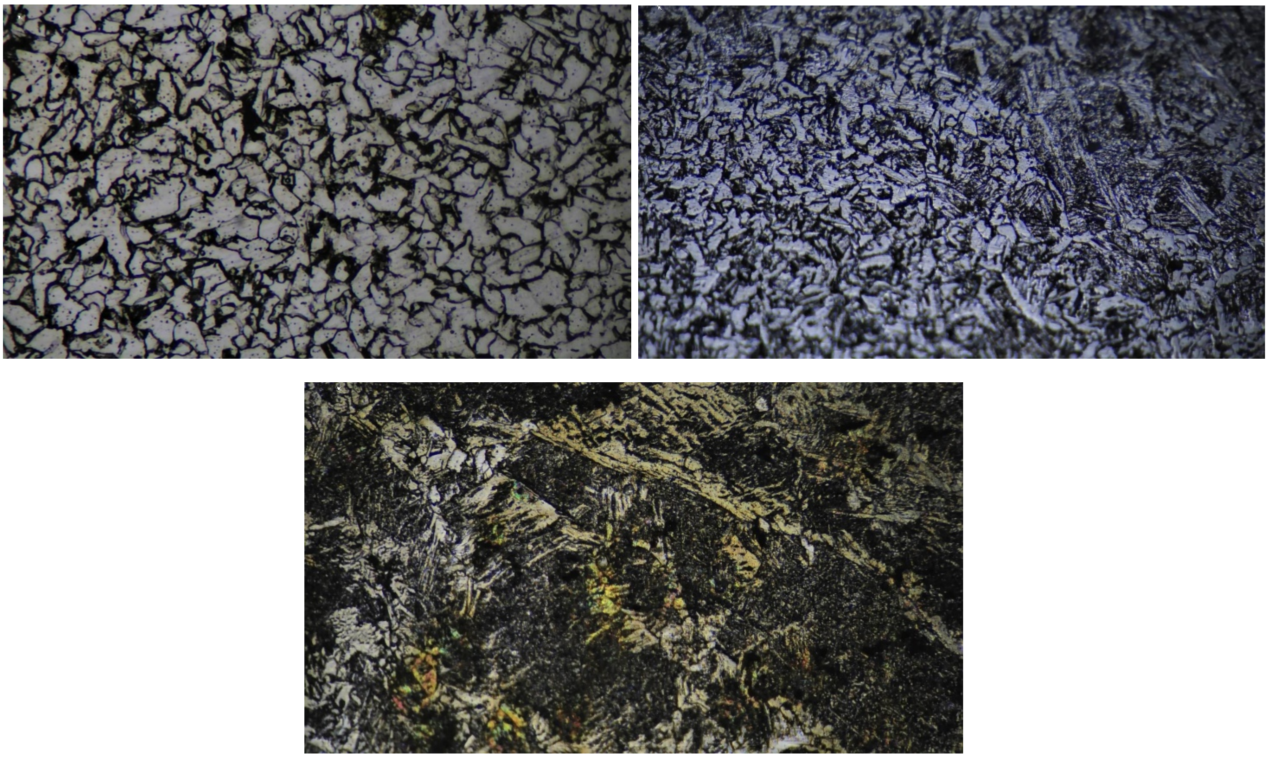

Figure 5.13 : Base material, HAZ and weld bead microstructures on GMAW workpiece

The structure of the base material is predominantly ferritic for both specimens. Moving towards the heat affected zone, it is observable a more abrupt transition towards lamellar structures such as bainite or martensite in the case of the SMAW weld. This phenomenon agrees with J. Hu, L. X. Du, J. J. Wang research [13], as the power supplied to the SMAW specimen is slightly higher than that supplied to the GMAW specimen.

5.4 Microstructure analysis from simulation

Since we have considered a multi-phase material in the simulation, the output allows us to observe the state of the microstructures after cooling. In particular we analyzed percentage quantities and dimensions of austenite, pearlite, ferrite, bainite and martensite. The simulation here analyzed was stopped at ¾ of the total length (500 mm).

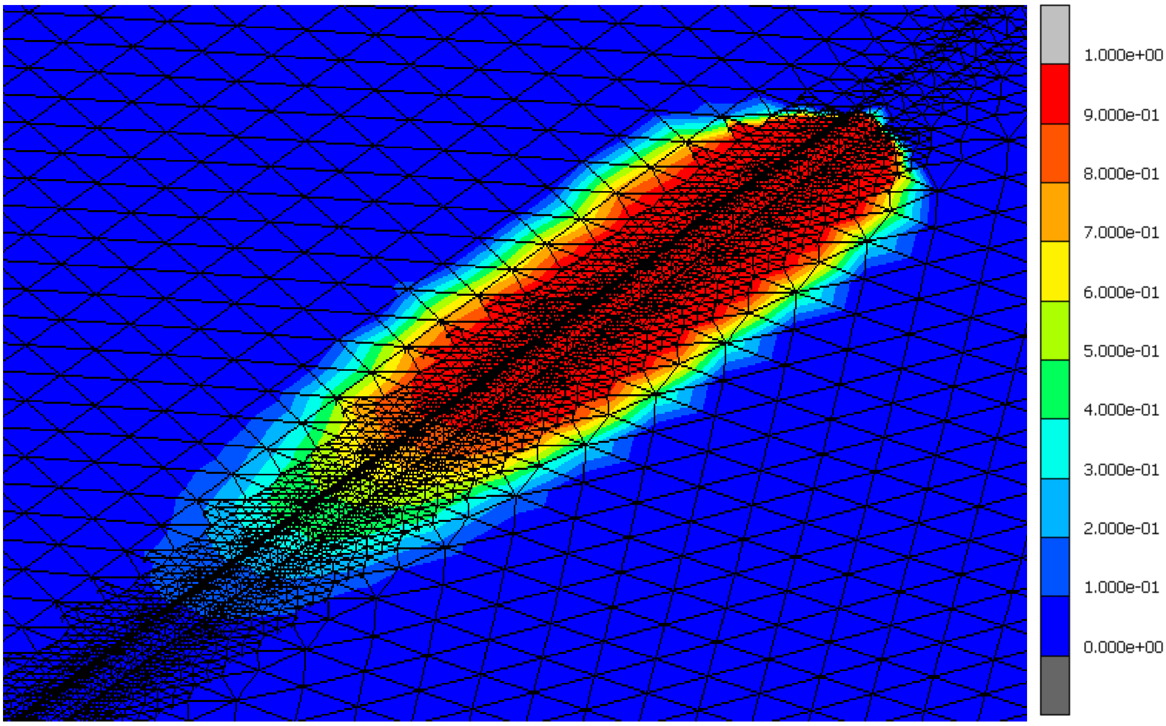

Figure 5.14 : Austenite distribution

As it is easily predictable the area where the electrode is currently melting, it is almost entirely composed of austenite due to the high temperatures. The austenite covers an area approximately 51 mm long and 16 mm wide (we considered the areas where the microstructure is present with more than 50 per cent).

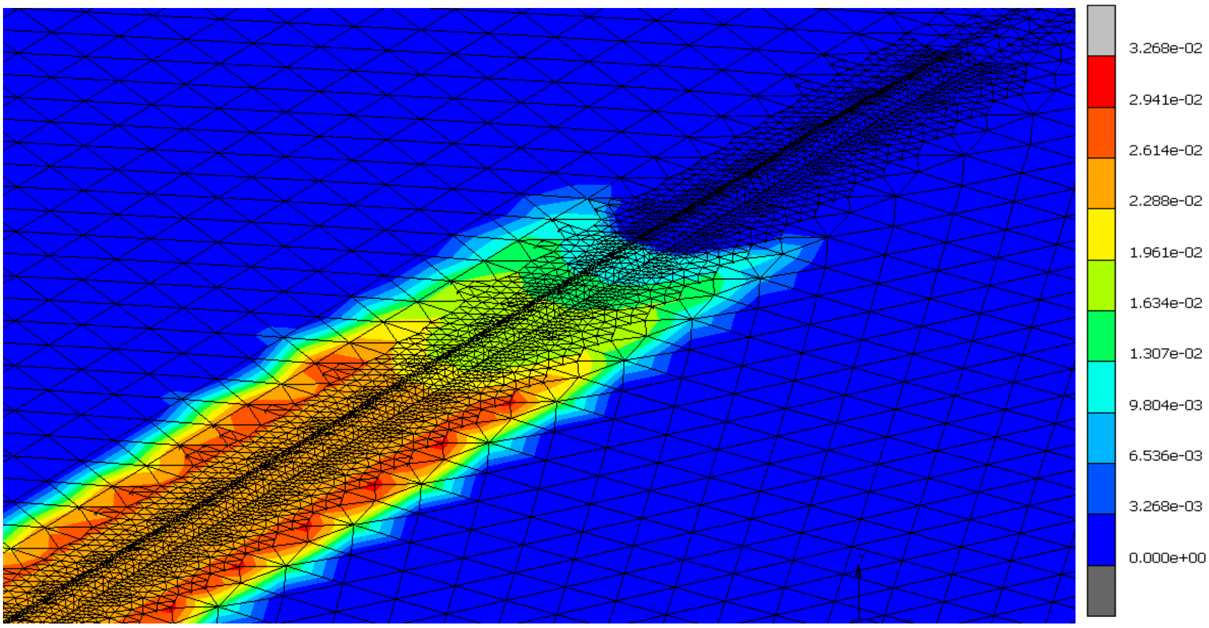

Figure 5.15 : Pearlite distribution

As we can observe from the last figure, the pearlite is present in relatively small percentages (between 2% and 3%) around the weld bead. This fact is probably due to the chemical composition of the base material with low carbon and to the uncontrolled cooling, which promotes the formation of bainite or martensite rather than perlite. While the width of the pearlite footprint is 15 mm wide, the length develops evenly along the entire weld bead, except for the initial part, because it has more exposed surfaces and for this reason it cools down faster, promoting the formation of other microstructures.

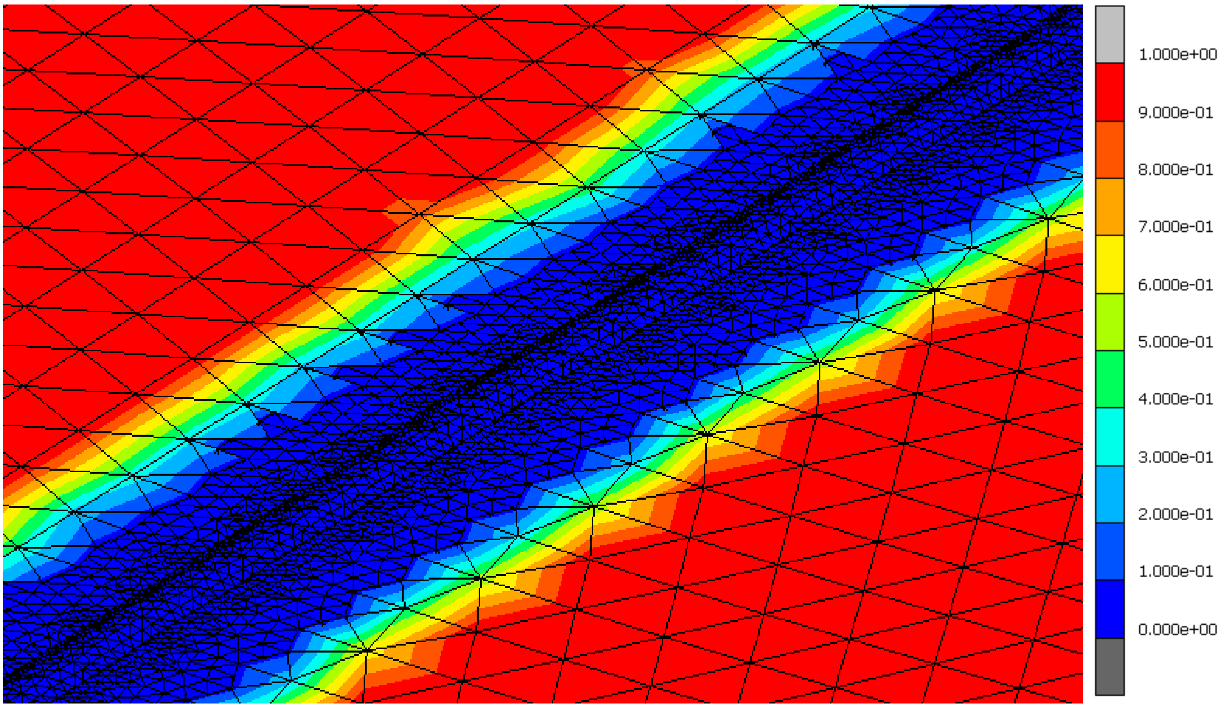

Figure 5.16 : Ferrite distribution

Being the base material, ferrite constitutes almost the entirety of the workpieces except for the weld bead and adjacent areas.

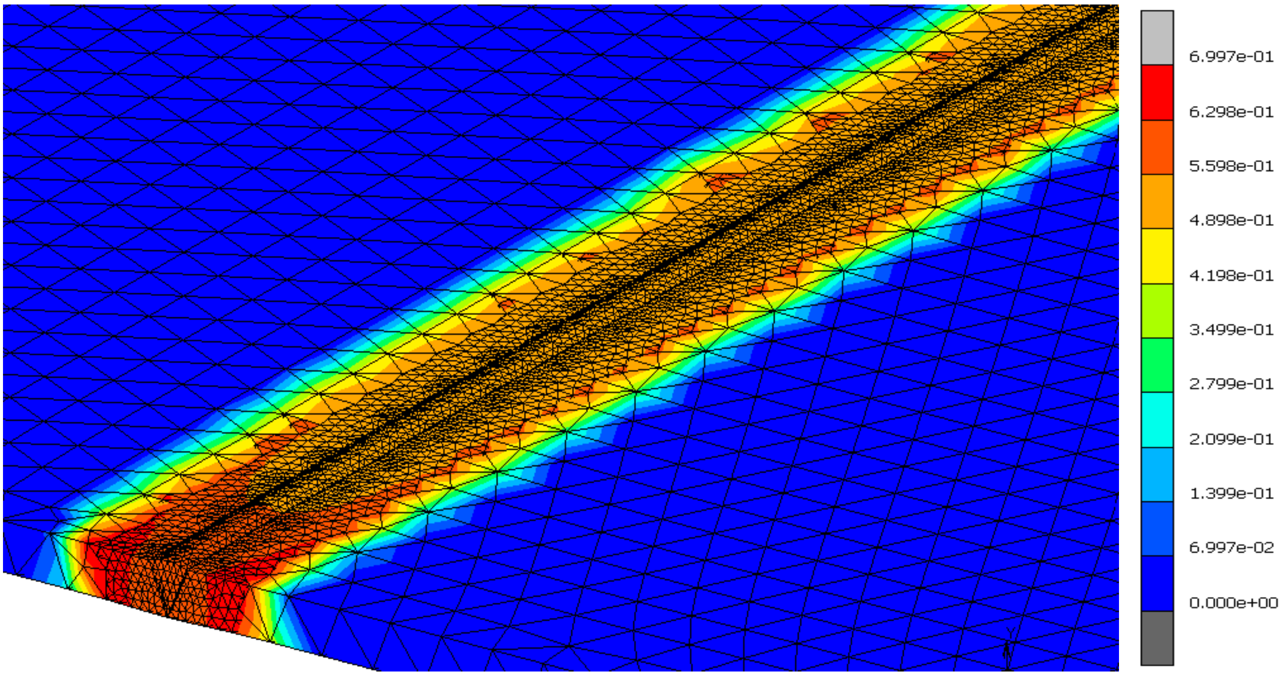

Figure 5.17 : Bainite distribution

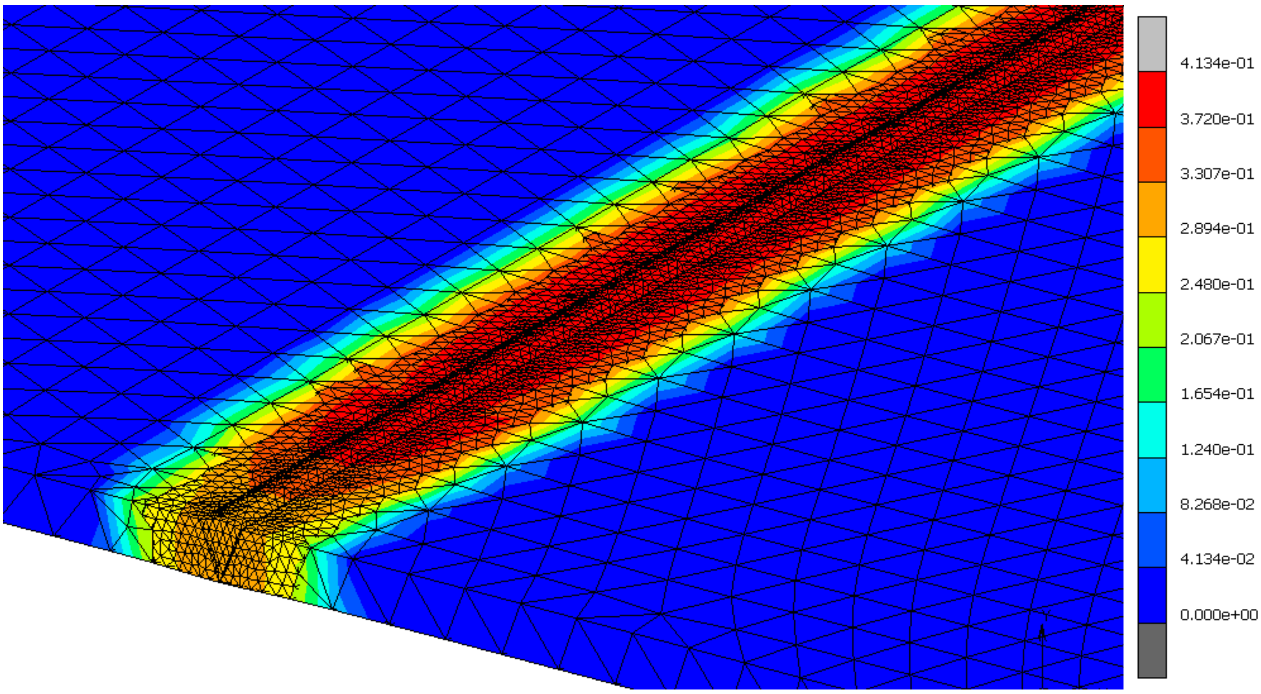

Figure 5.18 : Martensite distribution

The last two remaining microstructures, bainite and martensite, are complementary. The weld bead in particular is mainly composed of bainite (around 60%) which makes the joint more resistant and martensite (around 35%). The maximum concentration of bainite is the initial part, where the cooling process is faster.

As mentioned before, we used two different methods to choose the most appropriate Goldak parameters. In particular we carried out a few tests until the HAZ width of the simulation matched with the experimental results and, in addition, until the profile and section temperature distribution started overlapping. In these simulations GMAW required a narrower and longer shape whereas SMAW required a slightly wider and shorter shape.

To define the HAZ + fused zone dimension from the simulation we measured the width of a section where the original ferrite of the base material starts changing its microstructure. In this case the simulation shows a HAZ width of 23 mm.

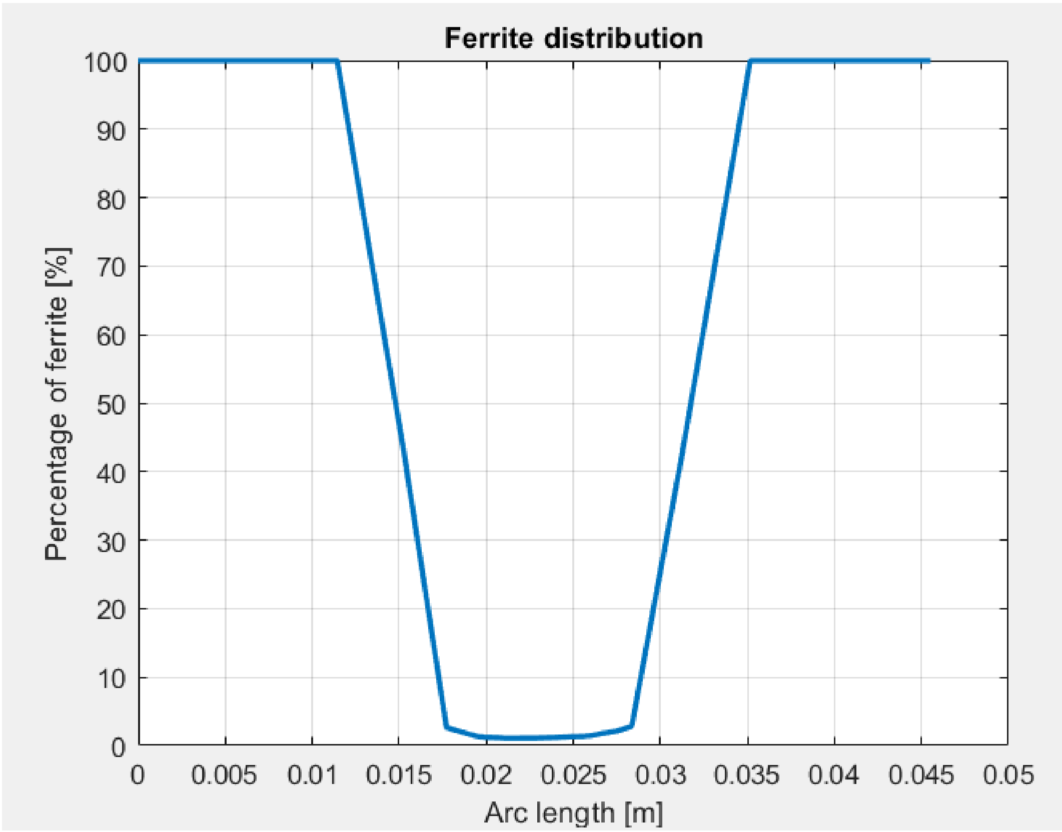

Figure 5.19 : Percentage of ferrite on a section

5.5 Vickers Hardness test

To detect the hardness of the material after the welding process, we decided to use the Vickers test procedure, which is an optical method based on size of indentation left by the indenter. The smaller the indent left by the indenter at a specific test force (15 seconds at 1 kgf in our experiment) in the surface, the harder the tested material.

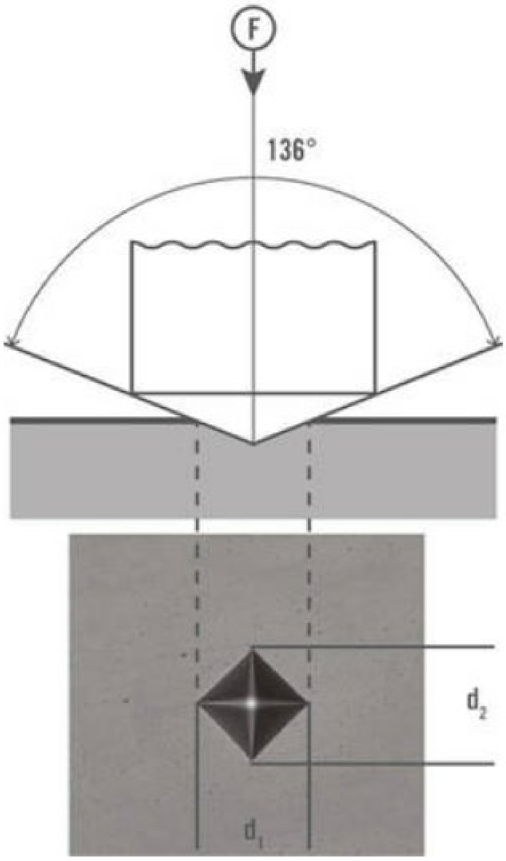

Figure 5.20 : Vickers hardness testing procedure

$$\mathrm{HV} = \mathrm{constant\ x}\,\frac{\text{test force F}}{\text{surface of the indentation}} = 0{,}102\ \mathrm{x}\,\frac{2\mathrm{F}\sin\frac{136°}{2}}{\mathrm{d}^2} = 0{,}1891\ \mathrm{x}\,\frac{\mathrm{F}}{\mathrm{d}^2}$$

$$\mathrm{d} = \frac{d_1+d_2}{2}\ \text{(average diagonal length)}$$

After taking several measurements, we can finally report the results of the Vickers hardness test on a graph both for the 5 mm SMAW and 5 mm GMAW workpieces.

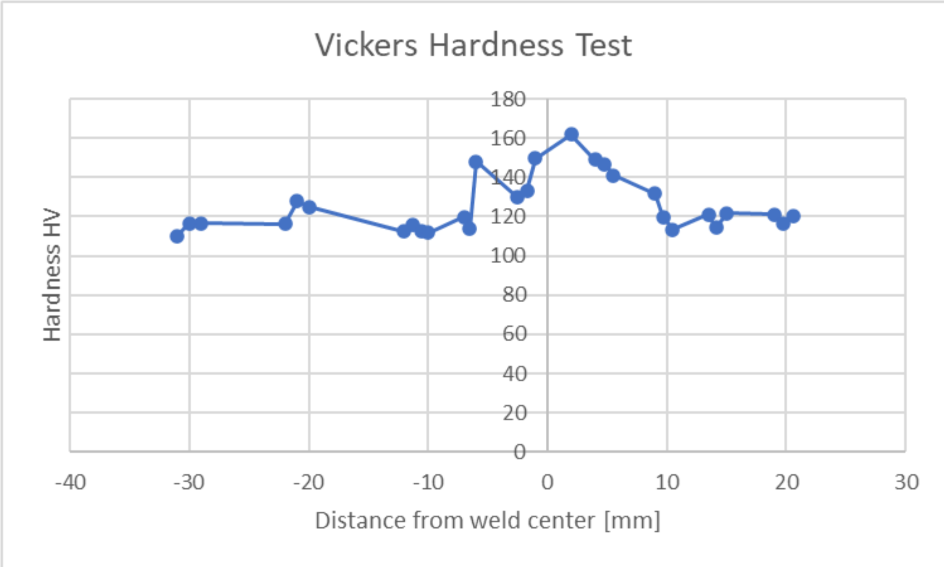

Figure 5.21 : Vickers hardness test on SMAW workpiece

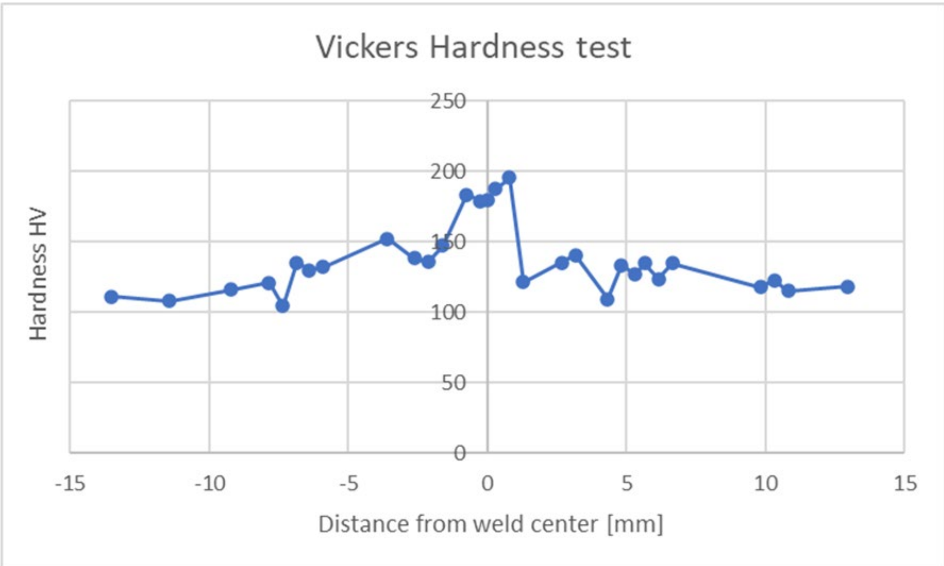

Figure 5.22 : Vickers hardness test on GMAW workpiece

This analysis could give us further information to identify the size of the HAZ, considering the values which deviate from the approximately constant hardness of the base material.

The analysis carried out on the GMAW test specimen in particular shows a section between 20 and 25 mm where the hardness data deviates from the plateau of the base material (around 120 HV for both specimens), in accordance with numerical simulation results.

6 FUTURE DEVELOPMENTS

Until now, the case we discussed about referred to the welding of relatively thin plates which required a single pass. However when the pieces to be welded are quite thick, it becomes necessary to weld in several passes. In the following example we tried to simulate the welding of two plates (39 mm thickness) with 38 passes. As usual the 3D model is first created on SolidWorks, then meshed and finally imported on Marc Mentat.

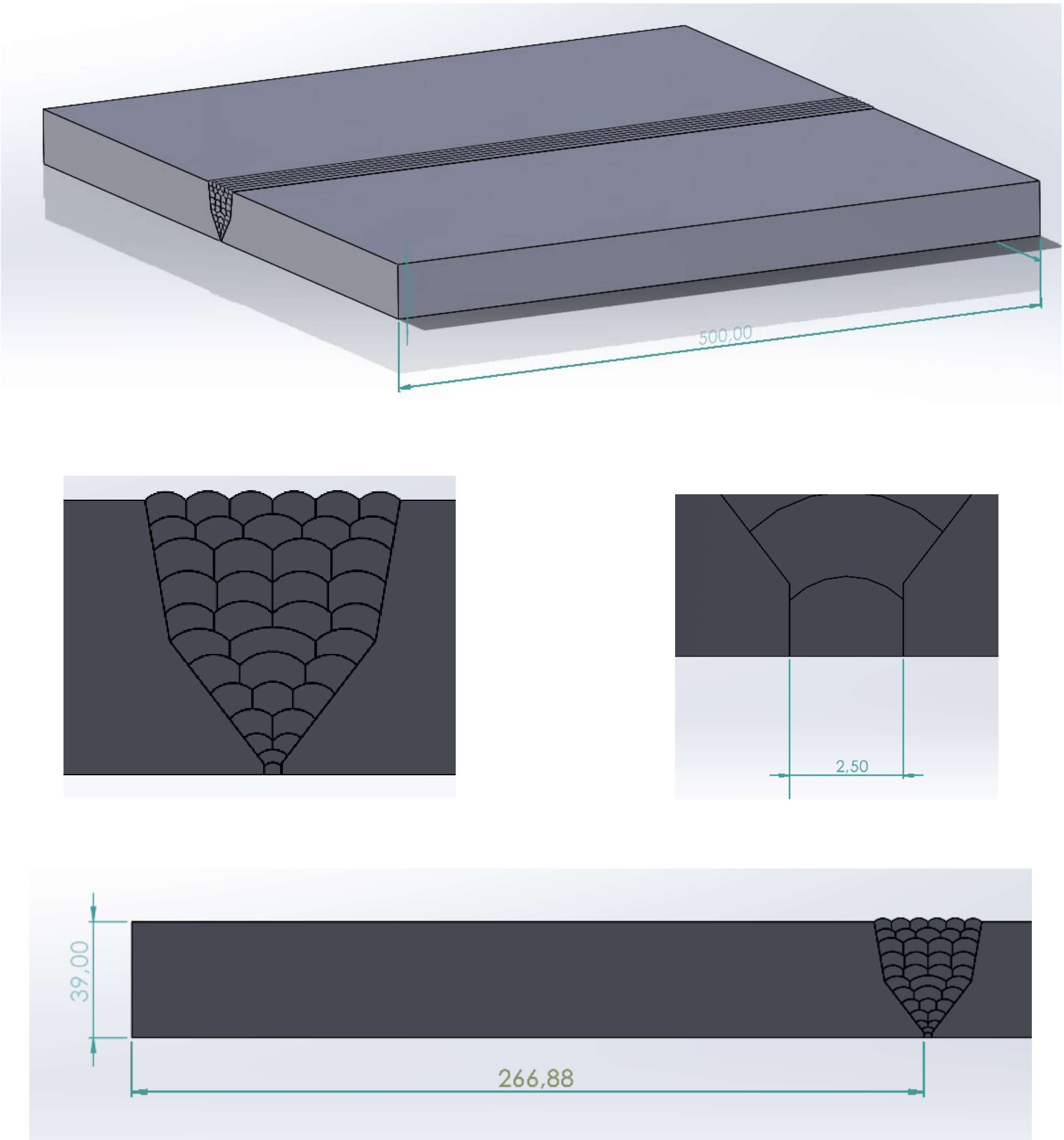

Figure 6.1 : 38-passes 3D model building on Solidworks

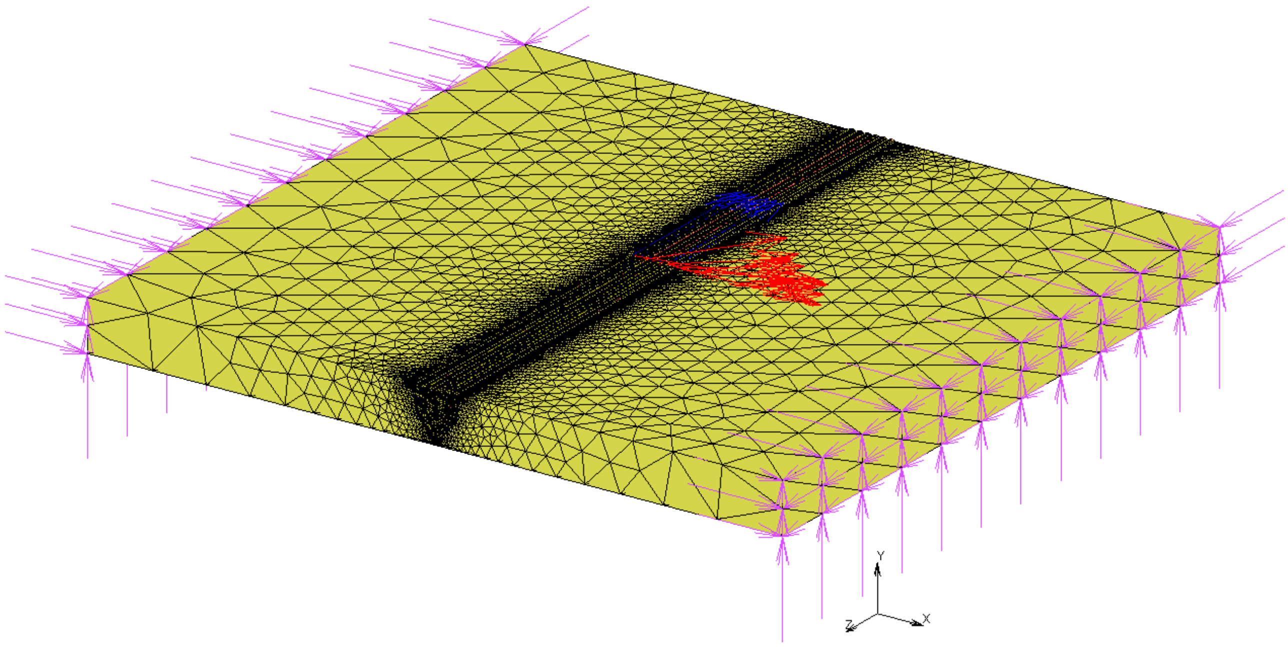

Figure 6.2 : Mesh definition

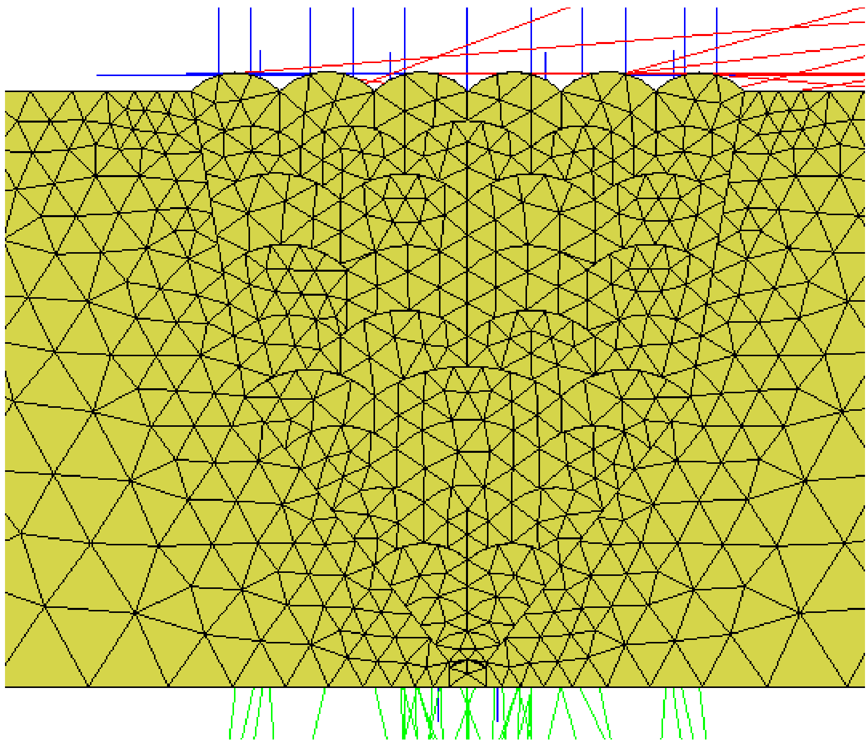

Figure 6.3 : Mesh detail of the weld fillers

This time the mesh is composed of 572830 elements and 1018058 nodes for a total of 1590888. Such a high number of elements makes it almost impossible to process the data on a normal PC and for this reason the use of high performance computing (HPC) is indispensable.

The main difference with the single pass model is in the loadcases and jobs: this time it was necessary to define two loadcases for each pass, the first for heating and the second for cooling.

For the heating loadcase a constant time stepping procedure has been used. In particular the total loadcase time was calculated dividing the total length of the weld by the welding speed while the value of the constant time step was decided choosing a sufficient number of steps to perform calculations twice within the same element along the weld.

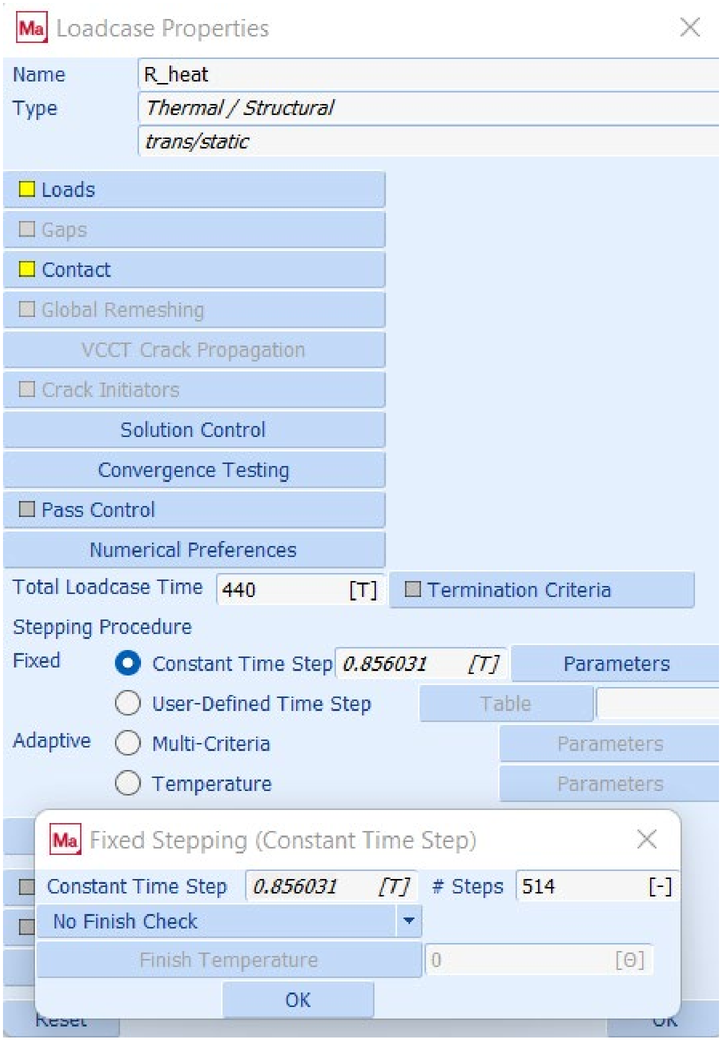

Figure 6.4 : Stepping procedure definition

Whereas for the cooling loadcase an adaptive multi-criteria stepping procedure has been used. In this case a very long cooling time has been set with a termination criteria that activates when the maximum percentage of contact body are below a temperature threshold (usually around 130).

7 CONCLUSIONS

The new active thermography technique introduced in this work showed us satisfactory results in detecting the presence of defects. In fact, comparing correctly executed welding sections with sections in which errors were induced deliberately, anomalies in temperature distributions were quite evident both in space and time.

In addition, the possibility of executing the thermal analysis simultaneously with the welding process itself could make it possible to considerably reduce the time and costs spent on the inspection of welded parts. For this reason the construction of an accurate simulation model would further contribute to resource savings, allowing us to know in advance structural and thermal properties and the state of microstructures. For the latter in particular, the experimental metallographic analysis was fundamental to evaluate the size of the weld bead and of the heat affected zone.

MSC Marc Mentat software proved to be very adequate for our purposes, offering us several results in output such as Von Mises Stress, displacement, microstructures, contact status, heat flux, etc. The main problem of this model, however, is related to the computational cost which increases significantly as the mesh refines. In fact to obtain satisfactory results, we had to change Goldak parameters several times and wait a few hours until at least half the length of the parts to be welded had been simulated. For this reason, as we have already said in the previous chapter, using a HPC system could be indispensable, especially for longer or multi-pass welds.

This work is a first approach to the simulation of two arc welding processes and it could be used as a starting point for a more detailed experimental analysis, including tensile and fatigue testing or deformation evaluation. In particular while evaluating the thermal transient, it would have been useful to measure the temperature evolution for a longer period in order to analyze the cooling process up to room temperature. Furthermore, to reduce the number of simulations performed, a statistical campaign on several experimental trials could be carried out on the basis of methods introduced in the state of the art chapter. Another aspect that could be further investigated is the emissivity: in our experiments we referred to standard values taken from the literature, as these materials are widely used in industry. However, as described on chapter 2.2.3, a poor emissivity calibration could lead to incorrect temperature results.

In conclusion, after comparing the experimental results with the simulated ones, we can say that the numerical model, with the right combination of Goldak parameters adopted, is able to accurately simulate the two arc welding processes analyzed in this work; in addition, from a purely experimental point of view, this new online thermography technique showed considerable potential in defect detection without using additional heat sources as in the traditional active thermography process.

RINGRAZIAMENTI

Ringrazio la Prof.ssa Sesana, per avermi guidato e supportato nella fase più importante del mio percorso accademico.

Un sentito grazie all’Ing. Luca Santoro, per il supporto costante, le dritte indispensabili e la sua complicità nella realizzazione di ogni capitolo della tesi.

Ringrazio Ades Group, in particolare l’Ing. Rini e l’Ing. Molica Nardo, per avermi dato la possibilità di svolgere parte del mio lavoro di tesi presso uno dei loro stabilimenti, seguendomi puntualmente nel corso dell’attività sperimentale.

Al leggendario gruppo “Cinesi 3.0”, in memoria dei serrati ritmi ”asiatici” dei vecchi tempi (tenuti forse per non più di due settimane), compagni di viaggio sin dai primissimi giorni e grandi osservatori ed estimatori della surreale “fauna” Politecnica (menzione d’onore per l’Uomo Ambiguo e per Sciarpaman).

Agli amici di sempre della “Cavarretto Band”, per essere stati sempre presenti e per portare un po' di spensieratezza nelle calde estati siciliane.

Alla mia famiglia, per avermi sempre sostenuto e per avermi permesso di portare a termine questo percorso.

BIBLIOGRAPHY

[1] S. Doshvarpassand, C. Wu, and X. Wang, "An overview of corrosion defect characterization using active infrared thermography," *Infrared Phys. Technol.*, vol. 96, no. September 2018, pp. 366–389, 2019, doi: 10.1016/j.infrared.2018.12.006.

[2] R. M. Farias, P. R. F. Teixeira, and L. O. Vilarinho, "Variable profile heat source models for numerical simulations of arc welding processes," *Int. J. Therm. Sci.*, vol. 179, Sep. 2022, doi: 10.1016/j.ijthermalsci.2022.107593.

[3] H. Arora, K. Mahaboob Basha, D. Naga Abhishek, and B. Devesh, "Welding simulation of circumferential weld joint using TIG welding process," *Mater. Today Proc.*, vol. 50, pp. 923–929, 2022, doi: 10.1016/j.matpr.2021.06.315.

[4] T. Kik, "Computational techniques in numerical simulations of arc and laser welding processes," *Materials (Basel).*, vol. 13, no. 3, Feb. 2020, doi: 10.3390/ma13030608.

[5] X. Jia, J. Xu, Z. Liu, S. Huang, Y. Fan, and Z. Sun, "A new method to estimate heat source parameters in gas metal arc welding simulation process," *Fusion Eng. Des.*, vol. 89, no. 1, pp. 40–48, 2014, doi: 10.1016/j.fusengdes.2013.11.006.

[6] R. Koňár and M. Patek, "Numerička simulacija zavarenog spoja od različitih materijala u simulacijskom programu SYSWELD," *Teh. Vjesn.*, vol. 24, pp. 137–142, 2017, doi: 10.17559/TV-20150513074103.

[7] O. Asserin, A. Loredo, M. Petelet, and B. Iooss, "Global sensitivity analysis in welding simulations - What are the material data you really need?," *Finite Elem. Anal. Des.*, vol. 47, no. 9, pp. 1004–1016, Sep. 2011, doi: 10.1016/j.finel.2011.03.016.

[8] R. Gadallah, N. Osawa, S. Tanaka, and S. Tsutsumi, "Critical investigation on the influence of welding heat input and welding residual stress on stress intensity factor and fatigue crack propagation," *Eng. Fail. Anal.*, vol. 89, pp. 200–221, Jul. 2018, doi: 10.1016/j.engfailanal.2018.02.028.

[9] R. Pamnani, M. Vasudevan, T. Jayakumar, P. Vasantharaja, and K. C. Ganesh, "Numerical simulation and experimental validation of arc welding of DMR-249A steel," *Def. Technol.*, vol. 12, no. 4, pp. 305–315, Aug. 2016, doi: 10.1016/j.dt.2016.01.012.

[10] S. Joshi, J. Hildebrand, A. S. Aloraier, and T. Rabczuk, "Characterization of material properties and heat source parameters in welding simulation of two overlapping beads on a substrate plate," *Comput. Mater. Sci.*, vol. 69, pp. 559–565, Jan. 2013, doi: 10.1016/j.commatsci.2012.11.029.

[11] A. Khudyakov, Y. Korobov, P. Danilkin, and V. Kvashnin, "Finite element modeling of multiple electrode submerged arc welding of large diameter pipes," in *IOP Conference Series: Materials Science and Engineering*, Nov. 2019, vol. 681, no. 1. doi: 10.1088/1757-899X/681/1/012025.

[12] F. F. Chen, J. Xiang, D. G. Thomas, and A. B. Murphy, "Model-based parameter optimization for arc welding process simulation," *Appl. Math. Model.*, vol. 81, pp. 386–400, May 2020, doi: 10.1016/j.apm.2019.12.014.

[13] J. Hu, L. X. Du, J. J. Wang, and C. R. Gao, “Effect of welding heat input on microstructures and toughness in simulated CGHAZ of V-N high strength steel,” *Mater. Sci. Eng. A*, vol. 577, pp. 161–168, Aug. 2013, doi: 10.1016/j.msea.2013.04.044.

[14] G. Mi, X. Zhan, Y. Wei, W. Ou, C. Gu, and F. Yu, “A thermal-metallurgical model of laser beam welding simulation for carbon steels,” *Model. Simul. Mater. Sci. Eng.*, vol. 23, no. 3, Feb. 2015, doi: 10.1088/0965-0393/23/3/035010.

[15] A. Salazar, A. Mendioroz, and A. Oleaga, “Flying spot thermography: Quantitative assessment of thermal diffusivity and crack width,” *J. Appl. Phys.*, vol. 127, no. 13, Apr. 2020, doi: 10.1063/1.5144972.

[16] N. P. Avdelidis and A. Moropoulou, “Emissivity considerations in building thermography.”

[17] E. D’Accardi, A. Ulbricht, R. Krankenhagen, D. Palumbo, and U. Galietti, “Capability of active thermography to detect and localize pores in Metal Additive Manufacturing materials,” *IOP Conf. Ser. Mater. Sci. Eng.*, vol. 1038, no. 1, p. 012018, Feb. 2021, doi: 10.1088/1757-899x/1038/1/012018.

[18] P. N. Narasimhan, S. Mehrotra, A. R. Raja, M. Vashista, M. Zaheer, and K. Yusufzai, “ScienceDirect Development of hybrid welding processes incorporating GMAW and SMAW,” 2019. [Online]. Available: www.sciencedirect.com

[19] A. R. Sayed *et al.*, “Mechanical and microstructural testing of C-45 material welded by using SMAW and GMAW process,” in *Materials Today: Proceedings*, 2020, vol. 38, pp. 223–228. doi: 10.1016/j.matpr.2020.07.036.

[20] D. Madier, “Practical Finite Element Analysis for Mechanical Engineers.”

[21] “Welding-Recommendations for welding of metallic materials-Part 1: General guidance for arc welding from IHS,” 2002.

[22] P. Hariprasath, P. Sivaraj, V. Balasubramanian, S. Pilli, and K. Sridhar, “Effect of the welding technique on mechanical properties and metallurgical characteristics of the naval grade high strength low alloy steel joints produced by SMAW and GMAW,” *CIRP J. Manuf. Sci. Technol.*, vol. 37, pp. 584–595, May 2022, doi: 10.1016/j.cirpj.2022.03.007.

[23] Storia della termografia, https://heatvision.it/storia/

[24] Thermal Imaging from the Beginning of the Thermographer’s Camera to the Present, by Ed Kochanek, Director of Sales Eastern Region, FLIR Systems, Inc., https://irinfo.org/12-1-2013-kochanek/

[25] Shielding gases for welding and their effects on stainless steel properties, assda.asn.au